MCRJ Volume 40 | No.2 | 2023

ISSN No. : 1985 – 3807
eISSN No. : 2590 – 4140

Malaysian Construction Research Journal

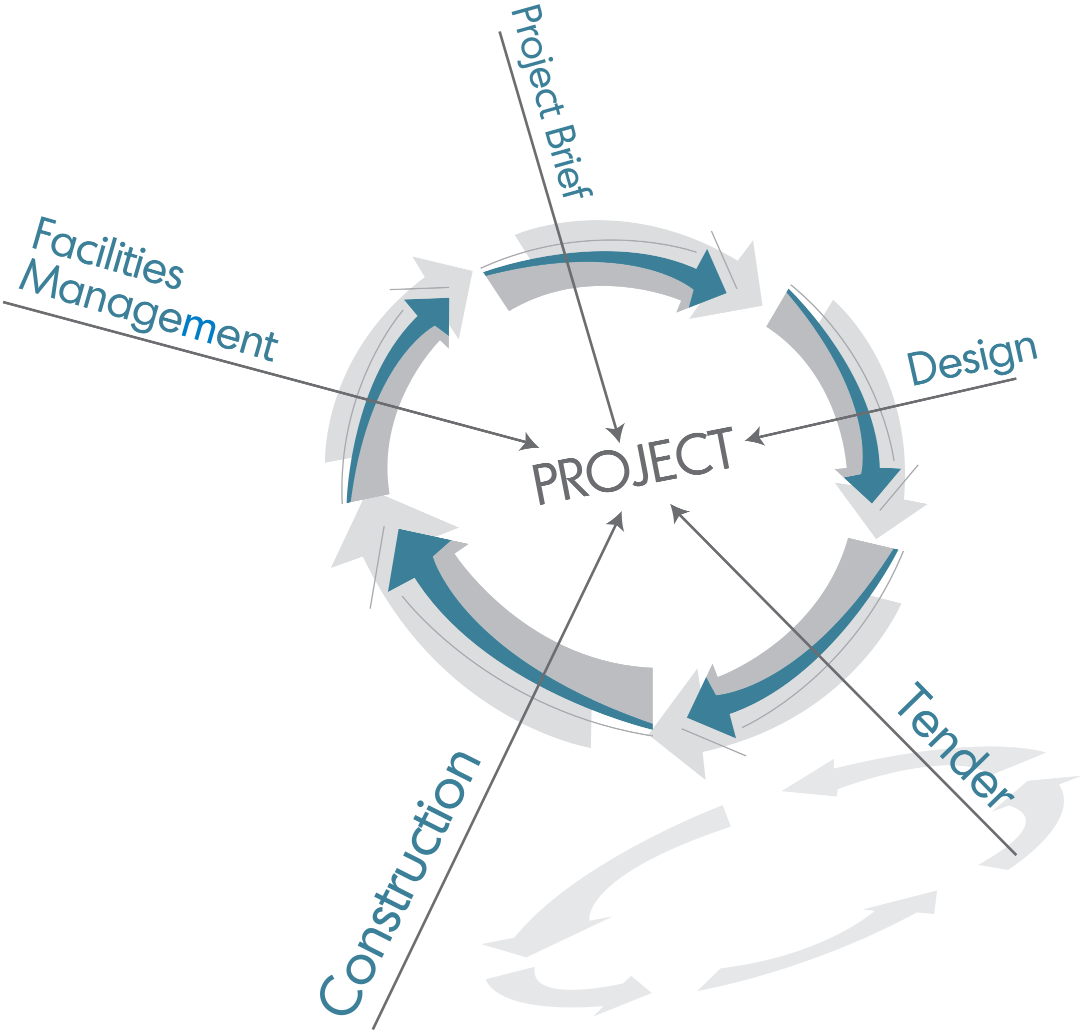

CREAM CONSTRUCTION RESEARCH INSTITUTE OF MALAYSIA

CIDB MALAYSIA

MALAYSIAN CONSTRUCTION RESEARCH JOURNAL (MCRJ)

Volume 40 | No. 2 | 2023

The Malaysian Construction Research Journal is indexed in

Scopus Elsevier and
ASEAN Citation Index

ISSN No. : 1985 – 3807
eISSN No. : 2590 – 4140

Construction Research Institute of Malaysia (CREAM)
Level 29, Sunway Putra Tower,
No. 100, Jalan Putra,
50350 Kuala Lumpur
MALAYSIA

This page intentionally left blank

Contents

Editorial Advisory Board

Abdelatif Hasinni, Dr.
University of Oran 2 Mohamed Ben Ahmed, Algeria

Abdul Halim Abdul Ghani, Assoc., Prof., Ir, Dr.
Universiti Tun Hussien Onn Malaysia (UTHM)

Zainorizuan Mohd Jaini, Ir, Dr.
Universiti Tun Hussein Onn Malaysia (UTHM)

Norliyati Mohd Amin, Dr.
Universiti Teknologi MARA (UiTM)

Siti Akhtar Mahayuddin, Dr.
Universiti Teknologi MARA (UiTM)

Ali M. Alashwal, Dr.
Western Sydney University

Ahmad Ruslan Mohd Ridzuan, Assoc., Prof., Dr.
Universiti Teknologi MARA (UiTM)

Mohd Azizul Ladin, Dr.
Universiti Malaysia Sabah (UMS)

Nadia Kamaruddin, Dr.
Universiti Teknologi MARA (UiTM)

P.Suresh Kumar, Dr.
University College of Engineering Ariyalur, India

Sibilike K. Makhanu, Eng., Prof., Dr.
Oshwal College, Kenya

Maisarah Ali, Prof., Ir, Dr.
International Islamic University Malaysia (IIUM)

Siti Nurbaya Ab. Karim, Ir, Dr.
Universiti Teknologi MARA (UiTM)

Sheila Belayutham, Assoc., Prof., Dr.
Universiti Teknologi MARA (UiTM)

Kartika Negara, Dr.
Queensland University of Technology, Australia

Che Khairil Izam Che Ibrahim, Assoc., Prof., Dr.
Universiti Teknologi MARA (UiTM)

Mahmud Kori Effendi, Dr.
Universitas Negeri Semarang, Indonesia

Lilawati Ab Wahab, Dr.
Universiti Teknologi MARA (UiTM)

Mohd Ezree Abdullah, Assoc., Prof., Dr.
Universiti Tun Hussein Onn Malaysia (UTHM)

Kamarudin Ambak, Dr.
Universiti Tun Hussein Onn Malaysia (UTHM)

Ahmad Kamil Arshad, Prof., Ir, Dr.
Universiti Teknologi MARA (UiTM)

Ng Chee Khoon, Prof., Dr.
Universiti Malaysia Sarawak (UNIMAS)

Afzan Ahmad Zaini, Assoc., Prof., Dr.
Universiti Malaysia Sarawak (UNIMAS)

Nur Akmal Abdullah Goh, Prof., Ar.
Universiti Malaysia Sarawak (UNIMAS)

Sulaiman Abdul Malik, Dr.
Universiti Teknologi MARA (UiTM)

Mohd. Khairolden Ghani, Ts, Dr.
Construction Research Institute of Malaysia (CREAM)

Juang Akbardin, Dr.
Universitas Pendidikan Indonesia

Hafizah Latif, Dr.
Universiti Teknologi MARA (UiTM)

Wendi Boy Rasyid, Dr.
Diponegoro University, Indonesia

Abu Saleh Ahmed, Assoc., Prof., Dr.
Universiti Malaysia Sarawak (UNIMAS)

Khariuddin Sanaullah, Assoc. Prof., Dr.
Universiti Malaysia Sarawak (UNIMAS)

Raudhah Ahmadi, Dr.
Universiti Malaysia Sarawak (UNIMAS)

Shazwan Mohamed Shaari, Dr.
Universiti Malaysia Sarawak (UNIMAS)

Bambang Karsono, Dr.
Universiti Malaysia Sarawak (UNIMAS)

Julaihi Wahid, Prof., Ar., Dr.
Universiti Malaysia Sarawak (UNIMAS)

Zayn Al-Abideen Gregory, Dr.
Universiti Malaysia Sarawak (UNIMAS)

Idawati Ismail, Dr.
Universiti Malaysia Sarawak (UNIMAS)

May Raksmey, Dr.
Universiti Malaysia Sarawak (UNIMAS)

Darrien Mah Yau Seng, Ir, Dr.
Universiti Malaysia Sarawak (UNIMAS)

Azida Hj Rashidi, Dr.
Universiti Malaysia Sarawak (UNIMAS)

Natasha Dzulkalnine, Dr.
Universiti Teknologi MARA (UiTM)

Raja Rafidah Raja Muhammad Rooshdi, Dr.
Universiti Teknologi MARA (UiTM)

Suliahti Hashim, Dr.
Universiti Teknologi MARA (UiTM)

Mysarah Maisham, Mrs.
Universiti Teknologi MARA (UiTM)

Alamah Misni, Ts, Dr.
Universiti Teknologi MARA (UiTM)

Norfashiha Hashim, Ts, Dr.
Universiti Teknologi MARA (UiTM)

Anis Rosniza Nizam Akbar, Dr.
Universiti Teknologi MARA (UiTM)

Abdul Hadi Nawawi, Ts, Sr, Dr., Prof.
Universiti Teknologi MARA (UiTM)

Zarita Ahmad @ Baharum, Dr.
Universiti Teknologi MARA (UiTM)

Yuhainis Abdul Talib, Assoc., Prof., Sr, Dr.
Universiti Teknologi MARA (UiTM)

Nor Suzila Lop, Sr, Dr.
Universiti Teknologi MARA (UiTM)

Siti Hasniza Rosman, Sr, Dr.
Universiti Teknologi MARA (UiTM)

Ahmad Shazrin Mohamed Azmi, Sr, Dr.
Universiti Teknologi MARA (UiTM)

Nurul Afiqah Azmi, Dr.
Universiti Teknologi MARA (UiTM)

Nurul Nadiah Zainol, Dr.
Universiti Teknologi MARA (UiTM)

Don Samarasinghe, Dr.
Massey University, Auckland, New Zealand

Saipol Bari Abd Karim, Assoc., Prof., Sr, Dr.
Universiti Malaya (UM)

Nurul Sakina Mokhtar Azizi, Dr.
Universiti Sains Malaysia (USM)

Shamsulhadi Bandi, Dr.
Universiti Teknologi MARA (UiTM)

Tun Mohd Irfan Mohd Suria Affandi, Dr.
Universiti Teknologi MARA (UiTM)

Nor Hazirah Hasri, Ms.
Universiti Teknologi MARA (UiTM)

Norsalisma Ismail, Dr.
Universiti Teknologi MARA (UiTM)

Fazly Amri Mohd, Dr.
Universiti Teknologi MARA (UiTM)

Aziz Rahman, Dr.
Universiti Teknologi MARA (UiTM)

Mastura Jaafar, Dr., Prof.
Universiti Sains Malaysia (USM)

Zul Zakiyudin Ahmad Rashid, Dr.
Universiti Sains Malaysia (USM)

Nadzirah Zainordin, Ts, Sr, Dr.
UCSI University

Noor Akmal Adillah Ismail, Dr.
Universiti Teknologi MARA (UiTM)

Har Einur Azrin, Assoc., Prof., Dr.
Universiti Teknologi MARA (UiTM)

Zairra Mat Jusoh, Dr.
UCSI University

Marlyana Azyyati Marzukhi, TPr, Dr.
Universiti Teknologi MARA (UiTM)

Anis Rosniza Nizam Akbar, Dr.
Universiti Teknologi MARA (UiTM)

Mohd Azwarie Mat Dzahir, Dr.
Universiti Teknologi Malaysia (UTM)

Mustaqqim Abdul Rahim, Ir, Dr.
Universiti Malaysia Perlis (UNIMAP)

Secretariat

This page intentionally left blank

Editorial

Welcome from the Editors

Welcome to the forty (40^{th}) issue of Malaysian Construction Research Journal (MCRJ). In this issue, we are pleased to include nine papers that cover a wide range of research areas in the construction industry. The editorial team would like to express our sincere gratitude to all contributing authors and reviewers for their contributions, continuous support and comments.

In this issue:

Mohd Arif Rosli et al., identified a macrocomposite as an adsorbent to treat kitchen wastewater from the UTHM Pagoh cafe. The characteristics of kitchen wastewater were determined by measuring two parameters: suspended solid (SS) and chemical oxygen demand (COD). Because the macrocomposite was composed of zeolite, activated carbon, aggregate, and cement, it had a porous structure and a large surface area for adsorption. The flow rate of kitchen wastewater through the column was variable. At regular intervals, an effluent sample was collected. The flow to the column was maintained until the interval of 120 minutes had passed. The performance of the column was evaluated with flow rates of 50mL/min, 60mL/min, and 70mL/min. Using the Yoon-Nelson and Thomas models, experiment data were analysed. The collected and analysed data for both models indicate that a flowrate of 50 mL/min is optimal for wastewater treatment, with the highest R2 and adsorption capacity values.

Noor Ain Najihah Che Rosely et al., evaluated the influence of varied water-cement ratios on the density, ultrasonic pulse velocity and compressive strength of cement mortars. Through Abrams' generalisation law, it is known that the compressive strength of concrete varies inversely with the water-cement ratio in workability and properties of mortars. Specimens are analysed through density, compressive strength tests and ultrasonic pulse velocity. Results indicate that the increase of the water-cement ratio reduces the values of properties and increases the workability. In this experiment, honeycomb appeared due to the improper workability of mortar because of low water content and did not use any superplasticizers, where the mortar was too stiff which made it tough to pour into the cube silicone moulds. Hence, it is suggested to add superplasticizers in the mortar mix with a low water-cement ratio.

Mohamad Hairi Osman et al., developed reinforcing concrete (RC) beam technology using Expanded Polystyrene (EPS) and Palm Oil Fuel Ash (POFA) as replacement materials for sand and cement. The heavy of existing concrete and the use of high cement are the main factors for this study to be carried out. POFA can be used as constituents in concrete due to the pozzolanic properties and EPS has the potential to be used in concrete as structural elements to reduce the density of concrete. The RC beams containing EPS and POFA as replacement materials with a percentage between 10% and 30% were studied in terms of crack. In this model, concrete's tensile cracking and compression crushing for every percentage of EPS and POFA were considered as data input in ABAQUS software.

Darrien Yau Seng Mah et al., analysed on a specifically designed stormwater detention structures that fit in a commercial centre, namely modular-based water micro tanks in the veranda and the parking lot in front of shop buildings. The two designs were simulated using Storm Water Management Model and subjected to historical rainfall data, in which the selected storms were found to span more than 10 hours and with maximum hourly rainfall depths between 40 - 70 mm. Results from the modelling efforts were stormwater characteristics of the particular type of detention system in times of extreme rainfall events. The identified stormwater characteristics provide a guide to urban planners to mitigate urban flooding. It was found that accumulated rainfall of a particular storm was a better indicator than the maximum rainfall depth of the storm to indicate the water storing capacity of detention structures.

Reventheran Ganansan et al., assessed current ANNs models to predict reasonable accuracy of crack width; however, not many studies have been found when it comes to the jointed part of the RC element subjected to lateral cyclic loadings. The ANN crack width prediction model based on Neural Net and Decision Tree was developed in this paper with a focus on the RC beam-column joint (BCJ) area, taking drift ratio, shear links, and length of the anchorage within the joint region into account. Based on the lowest errors, the best crack width model is chosen and further optimised using data splitting ratios.

Nik Elisa Lidya Nik Badrul et al., identified the numerical application of the shape change strategy on a six-strut model. The shape change method solves the optimisation problem for forced elongation in cables and minimises distance between the targeted coordinates and monitored nodes. A total of four numerical cases for a six-strut tensegrity model were studied, with one or two nodes monitored to approach the targeted coordinates prescribed in either x-, y- or z- directions. It is found that the six-strut model in all cases has successfully displaced and advanced to the prescribed targets via the shape change method. The numerical analysis results also show that the six-strut model performed axial and twisting deformations with the axial forces maintained within the elastic limit.

Sam Tan Chek Siong et al., suggested a new passive cooling roof concept called the "breathable roof system" to mitigate heat trapping in the attic space of ordinary roof systems. A case study was conducted on residential houses in Shah Alam, Malaysia, using thermocouples to measure temperatures in intermediate double storey terrace houses facing North-South and East-West directions. The aim was to quantify the effectiveness of the breathable roof system compared to conventional roof systems. The study also included comparisons of temperatures between different house orientations and an investigation of heat profiles in the rooms. The results showed that the breathable roof system can reduce heat by 12.3-19.5% compared to the conventional roof system. The use of the breathable roof system could be considered as an alternative solution for conserving energy and achieving sustainable development.

Vidhya Kanakaraj and Clementz Edwardraj Freeda Christy identified that the factors like composition of GPC, alkali activator concentration, recycled aggregate strength, the inter-transition zone, water/binder ratio and the curing temperature influence the strength of the geopolymer concrete with recycled aggregate. The properties of geopolymer concrete with the thermo-mechanically treated recycled aggregate varies with the molar activator concentration and the curing temperature. Slag based geopolymer concrete with recycled aggregate had higher compressive strength under ambient curing whereas flyash based geopolymer concrete had higher compressive strength under steam curing.

Bismiazan Abd. Razak et al., verified IES-VE reading accuracy of naturally ventilated Royal Malaysia Police (RMP) lockup cell thermal comfort performance. The methodology used in this research is empirical comparison analysis by comparing field measurement with IES-VE simulation results. Parameter used are air temperature, mean radiant temperature, and relative humidity as thermal comfort factors, and operative temperature as thermal comfort index which were extracted from three sets of Delta Ohm HD32.3 WBGT-PMV (internal parameters), one set of Seven Elements Integrated Weather Sensor WTS700 (external parameters), and IES-VE simulation. The results showed that the range of percentage differences between field measurement and the IES-VE simulation is within the acceptable range, which support the previous studies.

Editorial Committee

This page intentionally left blank

MACROCOMPOSITE EFFECTIVENESS IN THE TREATMENT OF USED WATER FROM THE UTHM PAGOH CAFÉ

Mohd Arif Rosli[1]*, Nurulaine Abdullah[1], Mariah Awang[1], Mohd Syafiq Syazwan Mustafa[1] and Mohamed Zuhaili Mohamed Najib[2]
[1]*Faculty of Engineering Technology, Universiti Tun Hussein Onn Malaysia, Malaysia.*
[2]*Department of Water and Environmental Engineering, School of Civil Engineering, Faculty of Engineering, Universiti Teknologi Malaysia, Malaysia.*

Abstract
This work aims to utilise a macrocomposite as an adsorbent to treat kitchen wastewater from the UTHM Pagoh café. The characteristics of kitchen wastewater were determined by measuring two parameters: suspended solid (SS) and chemical oxygen demand (COD). Because the macrocomposite was composed of zeolite, activated carbon, aggregate, and cement, it had a porous structure and a large surface area for adsorption. The flow rate of kitchen wastewater through the column was variable. At regular intervals, an effluent sample was collected. The flow to the column was maintained until the interval of 120 minutes had passed. The performance of the column was evaluated with flow rates of 50mL/min, 60mL/min, and 70mL/min. Using the Yoon-Nelson and Thomas models, experiment data was analysed. The collected and analysed data for both models indicate that a flowrate of 50 mL/min is optimal for wastewater treatment, with the highest R^2 and adsorption capacity values.

Keywords: *Zeolite; macrocomposite; COD; suspended solid.*

INTRODUCTION

Water pollution is a major global problem that is getting worse by the year, according to the current study, which is based on Water Resources Management Policies in Malaysia 2014 from the journal of Quality of Water Resources in Malaysia (Yuk et al., 2015). In Malaysia, measurements of the river water quality made at particular monitoring sites are not published with exact values. Instead, the Water Quality Index (WQI) divides water quality into three categories (clean, slightly polluted, and polluted) based on six variables including pH, dissolved oxygen (DO), biochemical oxygen demand (BOD), ammonia nitrogen, and suspended solids (SS). A total of 473 rivers were surveyed for the Rural Development (2014), Environment Quality 2013 report; only 53% were found to be significantly polluted.

More than 200 fast food restaurants and over 9,000 restaurants can be found in Malaysia. Each day, they use more than 500,000 tonnes of water. Regrettably, the load on municipal wastewater collection and treatment facilities was significantly increased as a result of the direct discharge of untreated wastewater from these restaurants into the drain. Due to the development of a fat, oil, and grease (FOG) layer on the water, the presence of FOG makes it challenging for oxygen to dissolve in water. Due to the coagulation of oil and grease on the drain's surface, this will eventually have an impact on the flow of water inside the drain.

The treatment of wastewater with macrocomposite, which is an environmentally with environment friendly green technology that is also natural and friendly to the environment, offers a more cost-effective method. In general, macrocomposite is a porous rock-like mass that can be used for wastewater treatment and is made of natural materials like aggregates, zeolite, activated carbon, cement, and sand (Ventures, 2014). The primary goals of this research is to describe the characteristics of the wastewater emitted from the UTHM Pagoh Cafe and to assess the efficacy of macrocomposites in the treatment of kitchen wastewater.

LITERATURE REVIEW

Kitchen Wastewater

The wastewater from the kitchen contained higher concentrations of oil and grease. This was caused by higher concentrations of foods, grease, and oil, which raise biochemical oxygen demand (BOD) levels. Grease can physically clog soil pores when it enters the soil absorption system, preventing both water infiltration and the oxygen transfer required for waste digestion. Grease with a higher biological oxygen demand (BOD) not only encourages excessive bacterial growth, but it also encourages it, which leads to the formation of thick anaerobic layers, which in turn leads to a worsening capacity to treat waste. This had the effect of already having the soil adsorption system fail (Nieuwenhuis et al., 2018). It is a common misconception that cooking oils that solidify as they are poured down the drain and cool in subsequent sewer lines are what cause the oil and grease deposits in public sewer lines. But it appears that the formation processes are much more complicated (Nieuwenhuis et al., 2018).

Large amounts of oil from food restaurant preparation can overwhelm a septic tank or treatment facility, causing untreated sewage to be discharged into the drain. Lard is one example of a high viscosity fat that solidifies upon cooling and can combine with other solids to clog drainpipes.

Recent Technology for Kitchen Wastewater Treatment

Kitchen wastewater can be treated using a variety of technologies, such as electrochemistry, membrane filtration, and biological processing. The two different electrochemical treatment technologies are multi-electrode electro-Fenton and electrochemical oxidation processes. Iron, aluminium, platinum-iridium, boron-doped diamond, titanium-rhodium, and have all been tested as electrode materials (Yu & Han, 2013).

Membrane filtration is a popular treatment method for oily wastewater. Among the membrane materials tested were polyvinylidene fluoride (PVDF), polysulfone (PS), polyacrylonitrile (PAN), ceramic materials, mullite, mullite-alumina ceramic material, TiO_2/carbon, and ceramic-polymeric composites (Chen et al., 2000).

Bio-Amp was used to treat grease trap wastewater that contained fat, oil, and grease biologically (FOG). Following the addition of the commercial bio-additive, their findings revealed a 40% reduction in FOG. Total nitrogen, total phosphorus, and total fatty acids all decreased by 39%, 33%, 56%, and 59%, respectively (Tang et al., 2012).

Unfortunately, a small-scale alternative with low capital investment but high maintenance requirements due to low holding capacity has been identified. Large-scale alternatives incur greater capital and energy costs but require less frequent personal attention due to their larger FOG storage capacity.

Macrocomposites

Zeolite, activated carbon, aggregate, and cement were the constituents of macrocomposite. Each component has its own function in wastewater treatment. In addition to absorbing organics, natural zeolite can remove ammonia from wastewater. To absorb colour and xenobiotic pollutants, the actual wastewater stream is treated with activated carbon. Granular media are critical for maintaining a high number of active biomass and a diverse range of microbial populations. Typically, it was square in shape with dimensions of 2 cm x 2 cm x 2 cm. Macrocomposites are the most preferred sustainable technology due to their low cost, low maintenance, and environmental friendliness (Rural Development, 2014).

MATERIALS AND METHODS

Collection and Preservation of Samples

The wastewater sample was collected from 11 a.m. to 1 p.m. at the UTHM Pagoh Campus cafeteria, where most students and staff eat lunch in the afternoon. Figure 1 depicts the location of the UTHM Pagoh Café.

Figure 1. Location of Wastewater Sample Collected

Adsorbent Preparation

For zeolite, activated carbon, and cement, the macrocomposite ratios are 20:5:6. To ensure that all the ingredients were properly incorporated, 60mL of water was added. The mixture was then poured into the 2 cm x 2 cm x 2 cm mould and allowed to dry for about two days at room temperature. Then, the macrocomposite underwent a curing procedure to strengthen its structure because of water pressure. After the curing process, macrocomposites were allowed to dry for two days before they were ready for use.

Column Adsorption Experiment

For this study, a gravity-based fixed bed adsorption column was utilised. Initially, a column was designed to determine the detention time and appropriate flowrate for the adsorption process. Figure 2 depicts a diagrammatic representation of the actual column design.

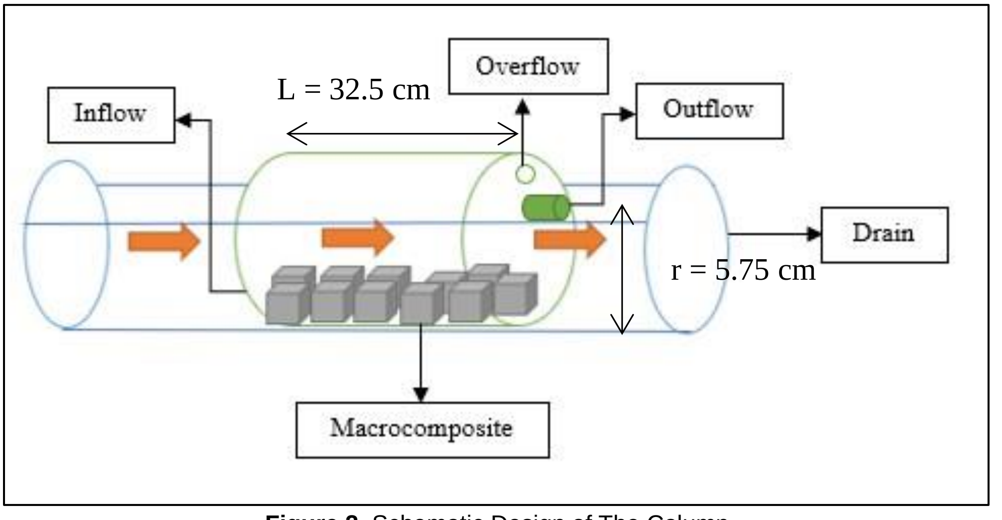

Figure 2. Schematic Design of The Column

Water Sample Collection

In this study, a method known as grab sampling was used to collect water samples over the course of several minutes, including the 2nd, 5th, 10th, 15th, 20th, 25th, 30th, 60th, 75th, 90th, and 2nd hours, for laboratory analysis. COD and SS were the two tested parameters. The purpose is to evaluate the effectiveness of macrocomposites in the treatment of kitchen wastewater.

Parameter Testing

Two tests were conducted in the laboratory, including chemical oxygen demand and suspended solid. Before and after application of the macrocomposite, the efficacy of the material in the treatment of kitchen wastewater was evaluated. The wastewater was diluted 10 times by mixing 1 mL of wastewater with 9 mL of distilled water. This is to ensure that the wastewater concentrations used for testing are lower. The Standard Methods for the Examination of Water and Wastewater APHA (2012) manual served as the basis for all the procedures.

Porosity Test

The porosity test was used to determine the adsorption process rate for the adsorbent. Table 1 shows the data for the adsorption column.

Table 1. The Adsorption Data for Column

Parameter	Unit		Value	
Diameter, D	m		0.115	
Surface Area, A	m^2		0.0104	
Media Height, H	m		0.320	
Volume, V	m^3		0.00033	
Density, ρ	kg/m^3		1458.65	
Porosity, ε	%		61.84	
Porosity Volume, V_ε	m^3		0.000206	
Mass, M = ρV	kg		0.485	
Flow rate, Q	mL/min	50.0	60.0	70.0
Empty Bed Contact Time, EBCT = V_ε /Q	min	4.1	3.4	2.9
Sludge Loading Rate, SLR = Q/A	cm/min	0.48	0.58	0.67

Percentage Removal

The purpose of wastewater treatment is to eliminate contaminants from the influent. Consequently, the percentage of removal efficiency formula is frequently used to calculate the performance of macrocomposites and evaluate the amount of contaminants that were removed. The percentage of removal was represented below:

$$Percentage\ Removal\ (\%) = \frac{C_i - C_f}{C_i} \times 100 \tag{1}$$

Where C_i and C_f represent the initial and equilibrium concentrations of all parameters in kitchen wastewater in mg/L, respectively.

Thomas Model

In the Thomas model, which is based on Langmuir adsorption-desorption kinetics, there is no axial dispersion. Based on continuous mode studies, this model is used to compute the adsorption rate constant and solid phase concentration of the metal ion on the adsorbent. (Vijayalakshmi et al., 2017). The linearized form of the Thomas Model is as follows:

$$\ln\left(\frac{C_o}{C_t} - 1\right) = \frac{k_T q_o m_c}{Q} - k_T C_o t \tag{2}$$

Where C_t and C_o were the effluent and influent metal ion concentration at time t, k_{TH} is the thomas rate constant (mL min^{-1} mg^{-1}), q_o is the maximum adsorption capacity (mg g-1) and Q is the flow rate (mL min^{-1}). The slope and intercept of a plot of ln (C_o/C_t -1) against time can be used to calculate the kinetic coefficient k_{TH} and the equilibrium uptake per gram of the adsorbent q_o (Vijayalakshmi et al., 2017).

Yoon–Nelson Model

The rate of decrease in adsorption probability for each adsorbate molecule in this model is assumed to be proportional to the probability of adsorbate adsorption and adsorbate breakthrough on the adsorbent (Nwabanne & Igbokwe, 2012). The Yoon-Nelson equation for a single component system was written as follows:

$$ln\left(\frac{C}{C_o - C}\right) = k_{YN}t - t_{0.5}k_{YN} \tag{3}$$

Where k_{YN} is the rate velocity constant (L/min), τ is time required for 50% adsorbate breakthrough (min), and *t* is time (min). The values of the rate velocity constant (k_{YN}) and time required for 50% adsorbate breakthrough (τ) can be obtained from the slope and intercept of plot of ln [C_t/(C_o-C_t)] versus t respectively (Nwabanne & Igbokwe, 2012).

RESULTS AND DISCUSSION

Initial Reading of Kitchen Wastewater

Various parameters for the initial wastewater were measured in order to define the characteristics of kitchen wastewater. The initial reading of kitchen wastewater discharged from the UTHM Pagoh Cafe before treatment is displayed in Table 2. Two parameters were measured, namely COD and SS.

Table 2. Initial Result of Kitchen Wastewater

Parameter	Unit	Result
COD	mg/L	1,653
SS	mg/L	377

Final Reading of Kitchen Wastewater

The effluent was subjected to three different flowrates of 50mL/min, 60mL/min, and 70mL/min in order to determine the efficacy of the macrocomposites at varying flowrates. Different flow rates produce various outcomes. The final characteristics of treated kitchen wastewater are displayed in Table 3 through Table 5 for each of the tested parameters.

Table 3. Result of Kitchen Wastewater for COD and SS at 50mL/min

Time (min)	COD (mg/L)	TSS (mg/L)
2	32	7
5	237	42
10	380	65
15	431	82
20	609	98
25	732	113
30	815	140
60	986	178
75	1352	245
90	1540	291
120	1611	360

Table 4. Result of Kitchen Wastewater for COD and SS at 60mL/min

Time (min)	COD (mg/L)	TSS (mg/L)
2	37	12
5	242	47
10	385	70
15	436	87
20	614	103
25	737	118
30	820	145
60	991	183
75	1357	250
90	1545	296
120	1616	365

Table 5. Result of Kitchen Wastewater for COD and SS at 70mL/min

Time (min)	COD (mg/L)	TSS (mg/L)
2	42	17
5	247	52
10	390	75
15	441	92
20	619	108
25	742	123
30	825	150
60	996	188
75	1362	255
90	1550	301
120	1621	370

Removal Efficiency

The regeneration studies will determine the reusability of the adsorbent, which contributes to its efficiency. Prior to beginning the regeneration study, the desorption experiment (Nwabanne & Igbokwe, 2012) was conducted. Based on the graphs of percentage removal for COD and SS shown in Figure 3 and Figure 4, the percentage of removal decreased as the amount of time elapsed. It will decrease until it reaches saturation, at which point macrocomposites will be unable to absorb or remove contaminants. From the beginning of the second minute until the end of the thirty-minute period, the graph showed that contaminants were removed actively. In comparison to 60mL/min and 70mL/min, the flowrate of 50mL/min is the most effective. This is because the percentage of contaminant removal increases as the flowrate and contact time decrease.

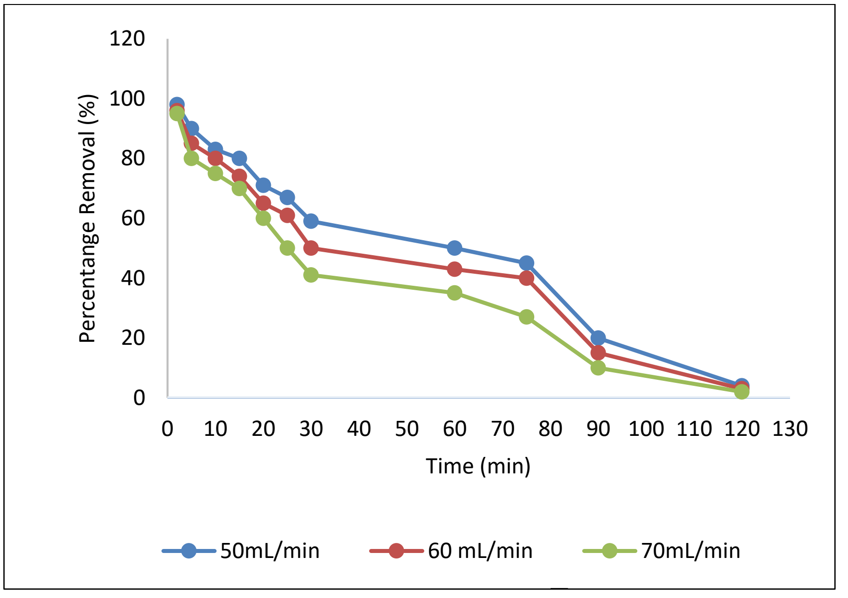

Figure 3. Graph of Percentage Removal for COD

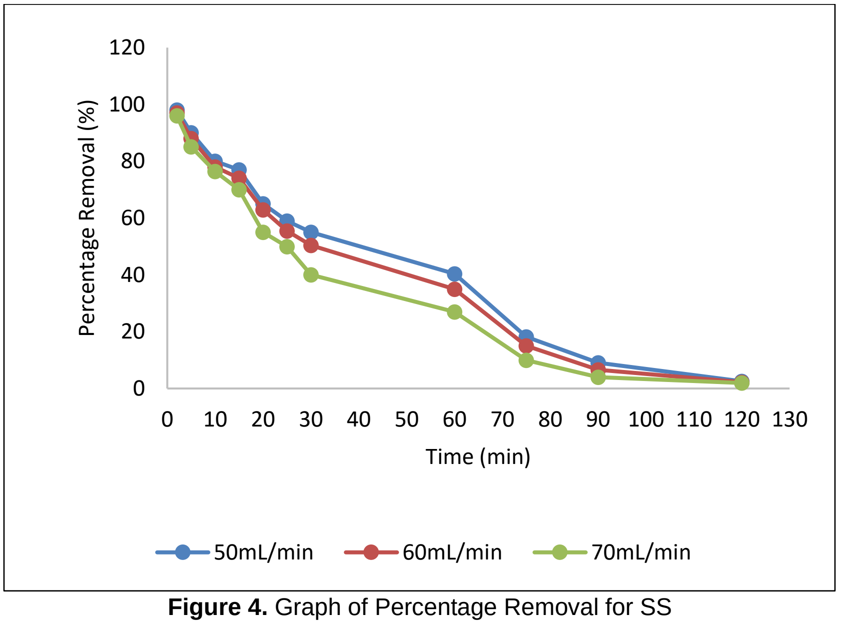

Figure 4. Graph of Percentage Removal for SS

Thomas Model

Many researchers have used the Thomas model to study packed bed adsorption kinetics (Vijayalakshmi et al., 2017, Nwabanne & Igbokwe, 2012). The Thomas model applies to adsorption processes in which neither external nor internal diffusion is limiting. Figures 5 and Figure 6 show the linear plot of the Thomas model for COD and SS using experimental data at flowrates of 50, 60, and 70mL/min, respectively.

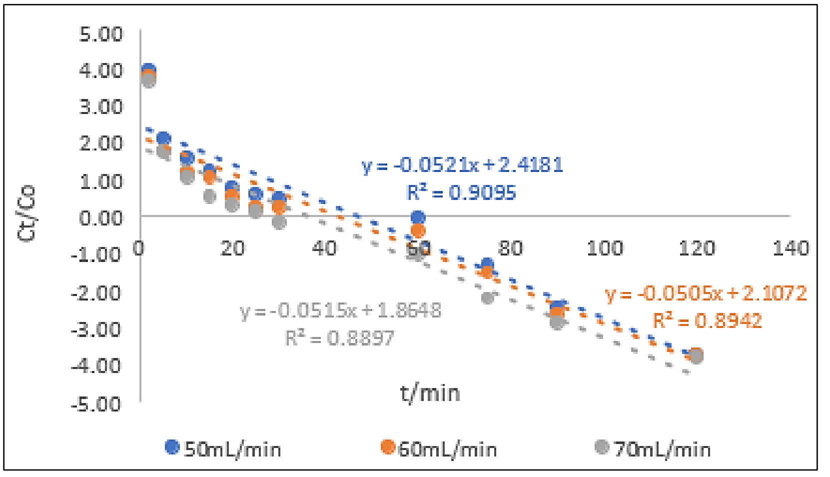

Figure 5. Graph of Thomas Model for COD

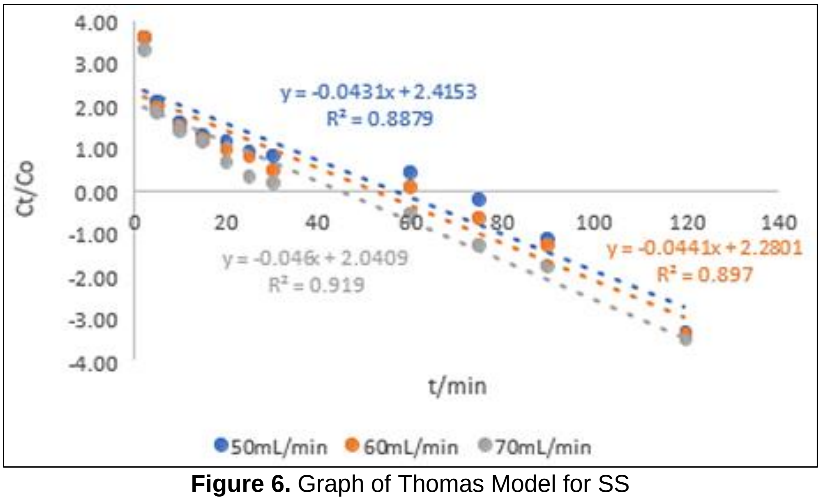

Figure 6. Graph of Thomas Model for SS

According to Table 6, the increase in flowrate led to an increase in the kinetic constant (K_{TH}) and a decrease in the adsorption capacity (q_o,*cal*) and R^2 for both COD and SS. When the flow rate was increased, the K_{TH} increased from 0.0521 to 0.0515 and the q_o,*cal* decreased from a range of 2.4181 to 1.8648. The values of R^2 for both COD and SS also decrease from 0.9095 to 0.8897 and from 0.9190 to 0.8879, respectively. The highest q_o,*cal* value can be attributed to more adsorption sites at slower flow rates. 50mL/min flow rate produced the highest R^2 value, which is closer to 1 than any other flow rate.

Table 6. Linear Plots of The Thomas Model for COD and SS at Different Flow Rates

Parameter	C_o (mg/L)	Q (mL/min)	K_{TH} (mL/min.mg)	q_o,*cal*	R^2
COD	1653	50	0.0521	2.4181	0.9095
	1653	60	0.0505	2.1072	0.8942
	1653	70	0.0515	1.8648	0.8897
SS	377	50	0.0431	2.4153	0.9190
	377	60	0.0441	2.2801	0.8970
	377	70	0.0460	2.0409	0.8879

Yoon-Nelson Model

Several authors (Vijayalakshmi et al., 2017; Nwabanne & Igbokwe, 2012) have used the Yoon and Nelson model to study column adsorption kinetics. The Yoon Nelson rate constant (K_{YN}) and correlation coefficients, $\tau_{0.5}$ are calculated from the slope and intercept of plots of ln (C_t/C_o-C_t) versus time, as shown in Figure 7 and Figure 8. Both graphs for COD and SS show the negative slope. For more than 40 minutes, the concentration of ln (C_t/C_o-C_t) shows positive readings that are in the range of 1.0, 2.0, and 3.0 at 60, 77, and 90 minutes, respectively. Based on the graph, it clearly shows that 50 mL/min > 60 mL/min > 70 mL/min.

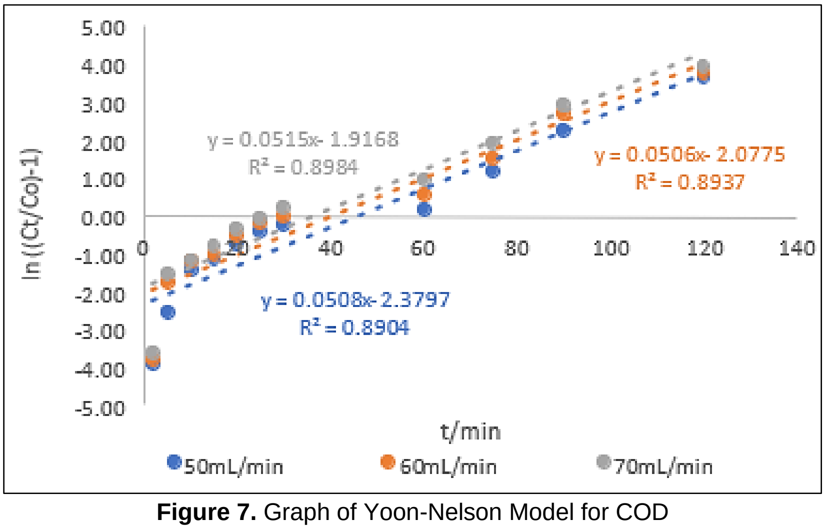

Figure 7. Graph of Yoon-Nelson Model for COD

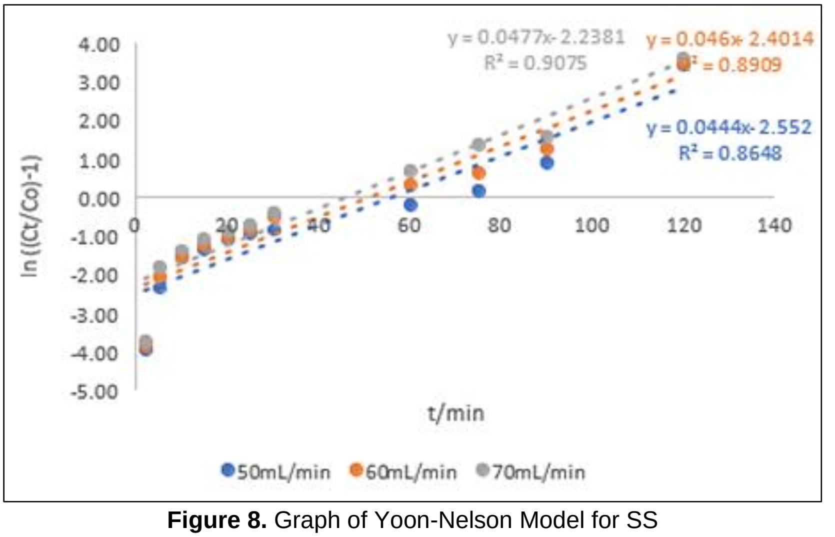

Figure 8. Graph of Yoon-Nelson Model for SS

Table 7 Yoon-Nelson model parameter obtained from linear plots of Yoon-Nelson model for COD and SS at different flow rate. It was discovered that with an increase in flow rate, the k_{YN} increased in the range of 0.8648 to 0.9075, while the time required for 50% breakthrough decreased in the range of 58.532 s to 37.219 min. The value of $T_{0.5}$ decreases with increases in flow rate. The slower the flow rate, the higher the treatment time taken to reach half the initial concentration. The value of R^2 obtained increased due to the increases in the flow rate.

Table 7. Linear Plots of The Yoon-Nelson Model for COD and SS at Different Flow Rates

Parameter	C_o (mg/L)	Q (mL/min)	K_{YN} (mL/min.mg)	$T_{0.5}$ (min)	R^2
COD	1653	50	0.0508	46.844	0.8904
	1653	55	0.0506	41.057	0.8937
	1653	70	0.0515	37.219	0.8984
SS	377	50	0.0444	58.532	0.8648
	377	55	0.0460	55.078	0.8909
	377	70	0.0477	49.406	0.9075

Compliance Standard

Standard A and Standard B from the 2009 Environment Quality Act (sewerage effluent) regulation DOE (2010) were compared to the final readings for treated wastewater with macrocomposite. Table 8 depicts the readings for COD and SS, along with a comparison of their initial and final values.

Table 8. Characteristic of Kitchen Wastewater with Standard A and B

Parameter	Before Treatment	After treatment	EQA, 1974	
			Standard A	Standard B
COD	1,653	32	120	200
SS	377	7	50	100

Standard A for COD and SS in accordance with the Environmental Quality Act for sewage effluent is 120 and 50, represented by the black line, while Standard B for COD and SS is 200 and 100, represented by the red line. According to the graphs in Figure 9 and Figure 10, the range time for standard A is 3 minutes, while for standard B it is 4 minutes. After plotting the SS graph, the range time for standard A is determined to be 7 minutes, while the range time for standard B is calculated to be 20 minutes.

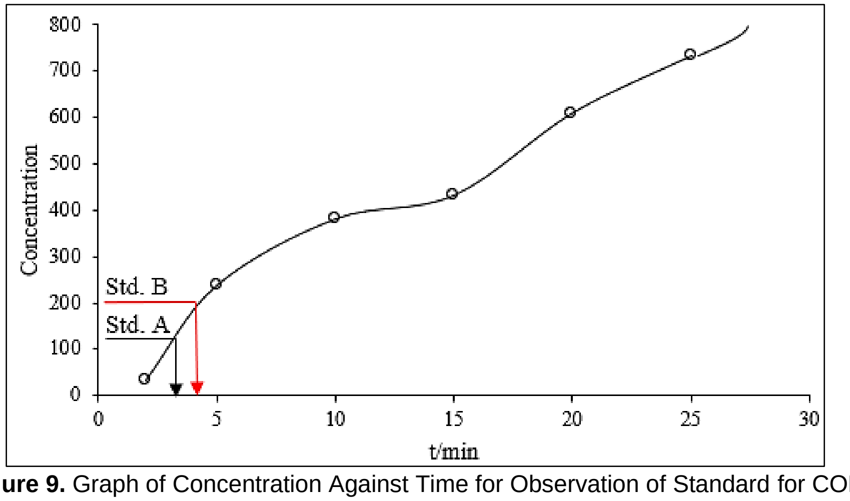

Figure 9. Graph of Concentration Against Time for Observation of Standard for COD

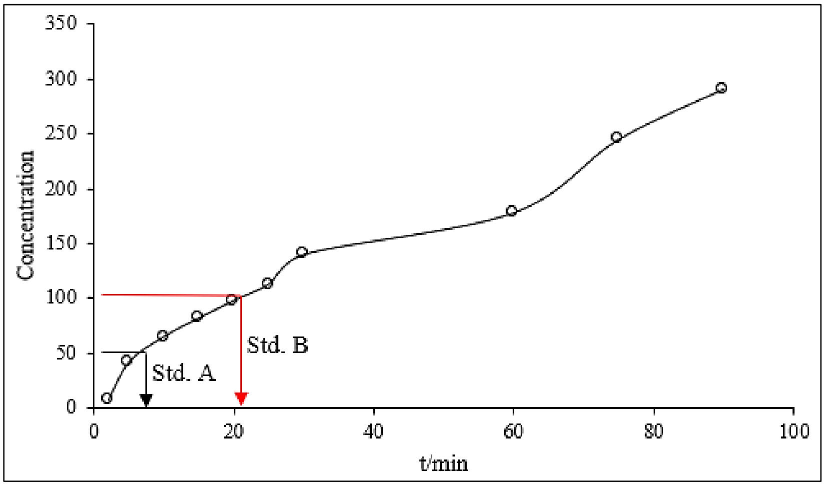

Figure 10. Graph of Concentration Against Time for Observation of Standard for SS

CONCLUSION

Before and after the application of the macrocomposites, the characteristics of the kitchen wastewater were measured in this study. The results for each tested parameter indicate the increase in reading relative to the initial result. It has been demonstrated that macrocomposite is effective for the treatment of kitchen wastewater from the UTHM cafe, allowing the contaminant to be removed. With a fixed bed height, various flow rates, including 50mL/min, 60mL/min, and 70mL/min, have been examined. The results and discussion indicate that, due to the longer contact time, the absorbent is more effective at absorbing and removing the contaminant at a lower flow rate. At lower flow rates, the Thomas and Yoon-Nelson models provide more accurate readings of adsorption capacity than at higher flow rates. The optimal flow rate for the treatment of kitchen wastewater was determined to be 50mL/min based on the preceding results.

ACKNOWLEDGEMENT

The authors acknowledge the Laboratory of Environmental Engineering, School of Civil Engineering, Universiti Teknologi Malaysia (UTM) and the Laboratory of Environmental Engineering Technology, Department of Civil Engineering Technology, Faculty of Engineering Technology, Universiti Tun Hussein Onn Malaysia for providing equipment and technical assistance.

REFERENCES

APHA (2012) Standard Methods for the Examination of Water and Wastewater. American Public Health Association,Washington DC.

Chen, X., Chen, G. and Yue, P. L. (2000) Separation of Pollutants from Restaurant Wastewater by Electrocoagulation, 19: 65–76.

Department of Environment (2010) Environmental Requirements: A Guide for Investors. Ministry of Natural Resource and Environment, (October), 1–14. https://doi.org/10.1016/j.cej.2013.06.055

Nieuwenhuis, E., Post, J., Duinmeijer, A., Langeveld, J., & Clemens, F. (2018) Statistical Modelling of Fat, Oil and Grease (FOG) deposits in wastewater pump sumps. Water Research, 135: 155–167.

Nwabanne, J. T., & Igbokwe, P. K. (2012) Adsorption Performance of Packed Bed Column for the removal of Lead (ii) using oil Palm Fibre. International Journal of Applied Science and Technology, 2(5): 106–115.

Rural Development, Agri. And Env. Stat. Dept. (2014) Environmental Report 2013. Retrieved from: https://www.ksh.hu/docs/eng/xftp/idoszaki/ekornyhelyzetkep13.pdf

Tang, H.L., Xie, Y.F. and Chen, Y.C. (2012) Use of Bio-Amp, A Commercial Bio-Additive for The Treatment of Grease Trap Wastewater Containing Fat, Oil, And Grease. Bioresour. Technol. 124: 52–58.

Ventures (2014) Macrocomposites for Wastewater Treatment, 8319. Retrieved from: http://www.platcomventures.com/upload/projectms/Macrocomposites_for_wastewater_treatment-utm.pdf

Vijayalakshmi, K., Sangeetha, K., and Sudha, P. N. (2017) Analysis of Packed Bed Adsorption Column with Nanochitosan/Sodiumalginate/Microcrystalline Cellulose Bead for Copper (II) Removal from Aqueous Solution, (December).

Yu, L. and Han, M. (2013) A Review of Treating Oily Wastewater. https://doi.org/10.1016/j.arabjc.2013.07.020

Yuk, F. H., Shin, A. Y., K. M. L. and T. S. L. (2015) Quality of Water Resources in Malaysia. Intech Open, 2: 64.

This page intentionally left blank

ROLES OF WATER-CEMENT RATIO IN WORKABILITY AND PROPERTIES OF MORTARS

Noor Ain Najihah Che Rosely[1], Wan Amizah Wan Jusoh[1,2]*, Mohamad Hairi Osman[1], Suraya Hani Adnan[1], Peniel Ang Soon Ern[1], Tuan Noor Hasanah Tuan Ismail[1], Syed Mohd Fareed Syed Zin[3], Mohamad Luthfi Ahmad Jeni[1] and Nur'ain Idris[4]
[1]Department of Civil Engineering Technology, Universiti Tun Hussein Onn Malaysia, Pagoh, Muar, Johor, Malaysia.
[2]Bamboo Research Centre, Universiti Tun Hussein Onn Malaysia, Pagoh, Johor, Malaysia.
[3]Department of Design Management, Lembaga Lebuhraya Malaysia, Kajang, Selangor, Malaysia
[4]Department of Civil Engineering, Centre for Diploma Studies, Universiti Tun Hussein Onn Malaysia Pagoh Higher Education Hub, Pagoh, Muar, Johor, Malaysia.

Abstract
Mortar is the material responsible for the distribution of stresses in masonry structures. Knowledge about the fresh and hardened properties of mortar is fundamental to ensure the good performance of masonry walls. Water-cement ratio is the variable that influences the physical and mechanical behaviour of mortars. The water-cement ratio has been regarded as the most important parameter in cement materials technology, such as concrete and mortar. Through the Abrams' generalisation law, it is known that the compressive strength of concrete varies inversely with the water-cement ratio in workability and properties of mortars. Specimens are analysed through density, compressive strength tests and ultrasonic pulse velocity. Results indicate that the increase of water-cement ratio reduces the values of properties and increases the workability. Besides that, honeycombing in mortar specimens was a rough surface that contained voids in the mortar as a result of incomplete filling. It was also known as hollow cavities found in the mortar mass where the mortar was not reached. In this experiment, honeycomb appeared due to the improper workability of mortar because of low water content and did not use any superplasticizers, where the mortar was too stiff which made it tough to pour into the cube silicone moulds. Hence, it is suggested to add superplasticizers in the mortar mix with a low water-cement ratio.

Keywords: *Mortar; water-cement ratio; workability; compressive strength.*

INTRODUCTION

Mortar is a component of masonry, a composite anisotropic material. Mortar is in charge of ensuring consistent stress distribution, rectifying block imperfections, and adapting thermal expansion and shrinkage deformations. It is well known that mortar has minimal effect on the compressive strength of brickwork (Haach, Vasconcelos, & Lourenco, 2011). In the cement industry, it is a well-known truth that cements mortar strength will be reduced when excessive content of the water is used, whereas mortar mixes might result in a poor workability state if inadequate content of water is applied. As a result, methods in identifying the most appropriate content of water to obtain high strength of cement mortar, as well as the water-cement ratio that plays a significant role in affecting cement mortar properties are clearly desirable. For concrete components, the water-cement ratio is rigorously controlled by the quality control unit. Moreover, the skilled worker believes that the mixture will be in a good workability state when more water is added. Hence, it is necessary enough to have a detailed investigation regarding the water-cement ratio that could affect the strength of mortar (Singh, Munjal, & Thammishetti, 2015).

Aggregate grading and the water-cement ratio serve a vital role in the workability and compressive strength of cement mortar, and these elements were investigated by the authors (Haach et al., 2011). As a result, he discovered that when increasing the value of the water-cement ratio, the mechanical properties of mortars will be degraded while increasing their workability. Another research conducted by the author (Schulze, 1999) emphasised on water-cement ratio effect and the content of cement in polymer-modified mortar properties. Meanwhile, Kim, Lee, Bang, & Kwon (2014) discovered that raising the water-cement ratio from 0.45 to 0.60 boosted the porosity of mortars by up to 150%, compared to the compressive strength, which decreased by up to 75.6%. Next, the authors of (Zhou, Chen, Wu, & Kan, 2011) discovered that when the water content in mortar mixture lowered, then the dynamic compressive strength of mortar improved. In addition, Ji-kai & Li-Mei (2015) discovered that a low water-cement ratio induced higher brittleness in fracture behaviour of mortar when compared to the mortar with a high water-cement ratio. An author investigated how a low water-cement ratio impacts the pore structure along with the strength of cement paste (Zivica, 2009). When employing finer sand grading specimens, a greater water-cement ratio is required to attain an equitable workability, according to (Lim, Tan, Chen, Lee & Lee, 2013). The authors found that mortar comprising coarser sand with low water-cement ratio obtained much higher strengths compared to the mortar with finer sand. The significance of sand grading on the properties of mortar has also been studied (Reddy & Gupta, 2018).

According to Ortiz, Aguado, Agullo, Garcia, & Zermeno (2009), the workability of mortars plays a significant role in constructing the structures of masonry. Workability is a crucial element of mortar since it strongly affects the work of the bricklayer. It is relevant to note that the mechanical properties of masonry can be significantly influenced by the quality of craftsmanship. Consistency, plasticity and cohesion are some of the properties' collections in workability (Haach, Vasconcelos, Lourenco & Mohamad, 2010). Consistency is ordinarily used to evaluate the workability of cement mortar rather than plasticity and cohesion due to difficulty to measure. Prior research indicates that investigating the fresh properties as well as the hardened properties of mortar in order to have a thorough understanding of its impact on the behaviour of masonry structures. Both the water-cement ratio and properties of aggregate are two factors that determine the fresh and hardened behaviour of mortar. The water-cement ratio has traditionally been regarded as the most significant element in the technology of cement materials. The compressive strength of concrete varies inversely with the water-cement ratio, as shown by Abrams' generalisation law, Equation 1 (Seart, Dewst, Kite, Harris & Troy, 1996).

$$Strength = \frac{K_1}{K_2^{w/c}} \tag{1}$$

Where K_1 and K_2 are constants, *w* represents the quantity of water and *c* represents the mass of cement. This formula works with water-cement ratios ranging from 0.3 to 1.20. The correlation between concrete strength and water-cement ratio is well known as Abrams' law. The application of Abrams' law is applicable for any time ranging from 3 to 365 days of concrete age, according to the author (Yeh, 2006). (Rao, 2001) demonstrated that empirical model expressions based on Abrams' law may forecast the compressive strength and split tensile strength of mortar utilising a water-cement ratio larger than 0.40. The water-cement ratio, cement-sand ratio, cementitious material type, and aggregate properties have all been determined to have the largest impact on cement mortar mechanical properties.

It should be emphasized, however, that mortar is way too different material compared to concrete, in terms of distinct structures, compositions, and applications. Few studies have been conducted to determine whether the water-cement ratio influences mortar strength. Traditionally utilisation of fibre also has been used to increase the strength (Ismail et al., 2021). Markeset & Hillerborg (1995) found several correlations between mechanical properties obtained in various mortar mixes, such as compressive strength, flexural strength and elastic modulus. A power function was also established to accurately characterise the compressive strength's dependency on the water-cement ratio. According to Neville (1995), aggregates have a considerable impact on the properties of mortars, which are rheological properties, as well as the mechanical properties. Moreover, the behaviour of mortars in both fresh and hardened state is basically influenced by mineralogical composition, stiffness, particle size distribution, form, and surface roughness of aggregates. Furthermore, the type of sand used has a significant impact on the properties of mortar. Grading curve geometrical factors like fineness modulus, relative specific surface and apparent weight are some of the factors that influence the consumption of water by the sand in the mortar, and these factors also play a role in the dry density of mortars. The objective of this research is to evaluate the influence of varied water-cement ratios on the density, ultrasonic pulse velocity and compressive strength of cement mortars. This study also discusses the applicability of Abram's law to cement mortar.

EXPERIMENTAL DETAILS

Material and Mix Design

All mortar mixes were produced using Ordinary Portland cement, sand, and tap water. The cement used was according to ASTM C 150-07 (2008). A sufficient number of cement mortar specimens with varying water-cement ratios have been created to investigate their influence on mortar strength. The mortar specimens were made up of Ordinary Portland cement (OPC) as a binder and local river sand for the fine aggregate. Table 1 shows the mix proportions of mortar specimens with fixed unit content of fine aggregate. Table 2 and Table 3 show the physical properties and chemical compositions of cement.

Table 1. Mix Proportions

Water-Cement Ratio	Cement (kg/m^3)	Water (kg/m^3)	Sand (kg/m$^{3)}$
0.30	933	280	947
0.40	865	348	947
0.50	808	405	947
0.60	758	455	947
0.70	713	500	947

Table 2. Physical Properties of Cement

Item	Spec. Limit	Test Result
Air content of mortar (volume %)	12 max	8
Blaine fineness (m²/kg)	260 min 430 max	377
Avg Blaine fineness (m²/kg)	280 min 420 max	385
Autoclave expansion (%)	0.80 max	0.04
Compressive strength (Mpa)	min:	

Item	Spec. Limit	Test Result
1 day	*A*	
3 days	7.0	23.4
7 days	12.0	29.8
28 days	*A*	
Time of setting (minutes) (Vicat)		
Initial Not less than	45	124
Initial Not more than	375	

(Source: ASTM C 150-07, 2008)

Table 3. Chemical Compositions of Cement

Item	Spec. Limit	Test Result
SiO_2 (%)	*A*	20.6
Al_2O_3 (%)	6.0 max	4.4
Fe_2O_3 (%)	6.0 max	3.3
CaO (%)	*A*	62.9
MgO (%)	6.0 max	2.2
SO_3 (%)	3.0 max	2.7
Ignition loss (%)	3.0 max	2.7
Na_2O (%)	*A*	0.19
K_2O (%)	*A*	0.50
Insoluble residue (%)	0.75 max	0.27
CO_2 (%)	*A*	1.5
Limestone (%)	*5.0 max*	3.5
$CaCO_3$ in limestone(%)	*70 min*	98
Potential (%)		
C_3S	*A*	50
C_2S	*A*	21
C_3A	*8 max*	6
C_4AF	*A*	10
$C_4AF + 2(C_3A)$	*A*	22
$C_3S + 4.75C_3A$	*100 max*	78.5

(Source: ASTM C 150-07, 2008)

The fine aggregates passing through 4.75 mm sieve have been used and its particle size distribution according to BS 882 (1992), is given in Figure 1. The material properties of fine aggregate are given in Table 4.

Table 4. Mix Proportions

Properties	Values
Fineness Modulus	3.5
Specific Gravity	2.42
Silt Content (%)	2.5
Bulking of Sand (%)	22

(Source: BS 882, 1992)

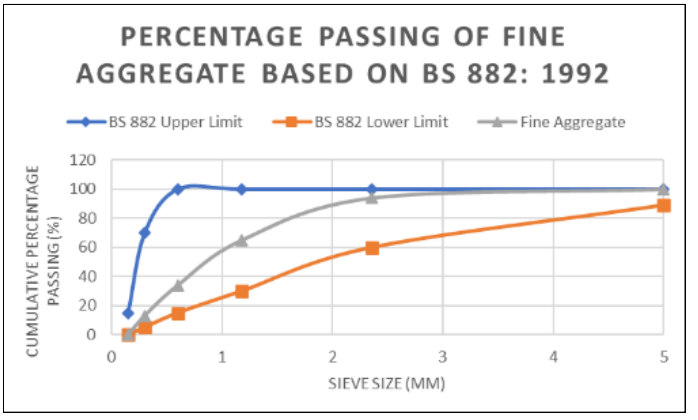

Figure 1. Particle Size Distribution Curve of Fine Aggregate

Methods and Test Procedures

A total of thirty mortars were prepared by weight batching in this experiment, with six mortars for each water-cement ratio ranging from 0.3 to 0.7. For a single water-cement ratio, the cement mortar mix was hand-mixed for 5-7 minutes. After mixing the mortar, six cubes of size (50 mm x 50 mm x 50 mm) were cast in cube silicone moulds with water-cement ratio of 0.3. Then followed by the rest of the mix ratios. Six cubes for each water-cement ratio, meaning that three cubes for 7 days of curing and another three cubes for 28 days of curing. A small coating of release agent was applied to the interiors of the silicone moulds using a clean brush before pouring cement mortar paste into the mould. Excess mortar was removed from the top of the mould using a metallic trowel. To accomplish full compaction, the mould was put on the vibrating table and vibrated for 2 minutes at a speed of 12,000 ± 400 per minute. Specimens were placed in the mould within the laboratory for a period of 24 hours (room temperature 30 ± 2°C and relative humidity 60% ± 5). The specimens were taken from the moulds and placed into the curing tank for 7 and 28 days at a temperature of 27 ± 2°C.

Density

The density of the cement mortars in this laboratory experiment was collected by referring to BS 4551 (1998). A single intact piece of hardened mortar of sufficient size was chosen from the day-7 and day-28 samples for each water-cement ratio and soaked in distilled water for 24 hours. The sample was hung from the balance arm using the wire stirrup and weighed while entirely submerged in water in a beaker, at the temperature of 27 ± 2°C. During the weighing procedure, be sure that neither the specimen nor the stirrup hits the edges of the beaker. Correctly compute the corrected mass in grams of the specimen alone in the water. Finally, take the specimens from the water and quickly dry their surfaces by lightly wiping them with absorbent cloth or paper before weighing them in the air.

Ultrasonic Pulse Velocity (UPV)

An electro-acoustical transducer in contact with one surface of the cement mortar under test produced a pulse of longitudinal vibrations. After travelling a specified route length in the mortar, the vibration pulse was transformed into an electrical signal by a second transducer and the transit duration of the pulse was monitored using electronic timing circuits. The apparatus, shown in Figure 2, included an electrical pulse generator, two transducers, an amplifier and an electronic timing device for measuring the time interval between the commencement of a pulse generated at the transmitting transducer and the onset of its arrival at the receiving transducer. To give a reference for the velocity measurement, a calibration bar was provided. The test for ultrasonic pulse velocity was conducted according to BS EN 12504-4 (2004). The pulse velocity for direct and semi direct transmissions must be calculated using the following formula:

$$V = \frac{L}{T} \tag{2}$$

Where V is the pulse velocity, in km/s, L is the path length, in mm, and T is the time taken by the pulse to transverse the length, in μs.

Figure 2. Set Up for Ultrasonic Pulse Velocity (UPV) Test

Compressive Strength

One of the most essential characteristics of masonry structures is the compressive strength of cement mortar. Three cube specimens were evaluated for 7-day of curing and another three cube specimens for 28-day curing. Six cube specimens were tested for each mix ratios in Universal Testing Machine (UTM) as per ASTM C 109/C 109M-02 (2002). Compressive strength was determined by placing the specimens in contact with the bearing surface of the Universal Testing Machine (UTM), as shown in Figure 3, and applying a load at a rate of 2-5 N/mm2 per minute until failure occurred. By dividing the greatest force applied to the specimen during the test by cross sectional area, the compressive strength was computed.

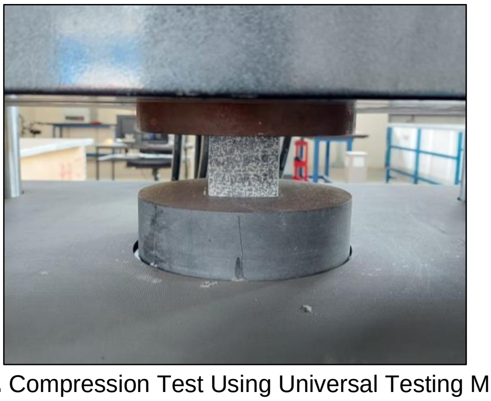

Figure 3. Compression Test Using Universal Testing Machine (UTM)

EXPERIMENTAL RESULTS AND DISCUSSIONS

Density, UPV & Compressive Strength of Cement Mortars at Day 7

Table 5 displays the recorded values of density, compressive strength and UPV test when cement mortar achieved 7-day curing, for all water-cement ratios. The link between density and water-cement ratio variation in mortar mixes at day 7 is depicted in Figure 4. At day 7, Figure 6 depicts the relationship between compressive strength and water-cement ratio in various mortar mixtures. There was a clear pattern of decreasing density and compressive strength as the water-cement ratio raised for all mortar mixtures. This result is compatible with the findings from Mohamad, Neto, Pelisser, Lourenco, & Roman (2009) and Fernandes, Silva, Ferreira, & Labrincha (2005). The increase in the water-cement ratio implies that there is more water between the solid particles, which results in larger voids in the hardened state, increasing porosity and consequently reducing the density and compressive strength of mortar mixtures. Figure 5 shows the relationship between the UPV test and water-cement ratio variation in mortar mixes at day 7. It can be seen that the value recorded for UPV at day 7 was still low.

Table 5. Values of Density, Compressive Strength and UPV Test Recorded on Cement Mortar at Day 7

Water-Cement Ratio	Density at day 7 (kg/m^3)	Compressive Strength at day 7 (kg/m^3)	UPV Test at day 7 (kg/m$^{3)}$
0.30	2173.60	34.19	1.37
0.40	2099.47	28.51	2.11
0.50	2039.47	17.63	0.68
0.60	2028.27	14.97	0.73
0.70	1942.93	9.99	0.78

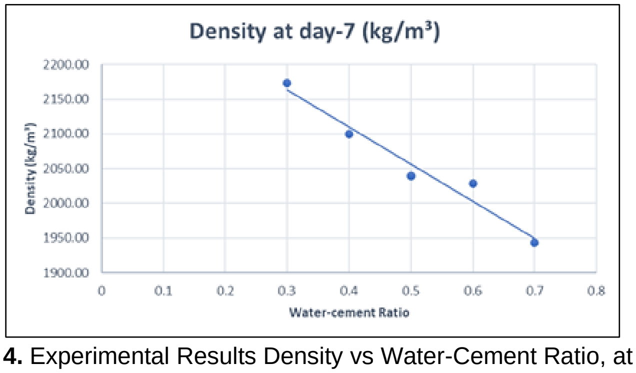

Figure 4. Experimental Results Density vs Water-Cement Ratio, at Day 7

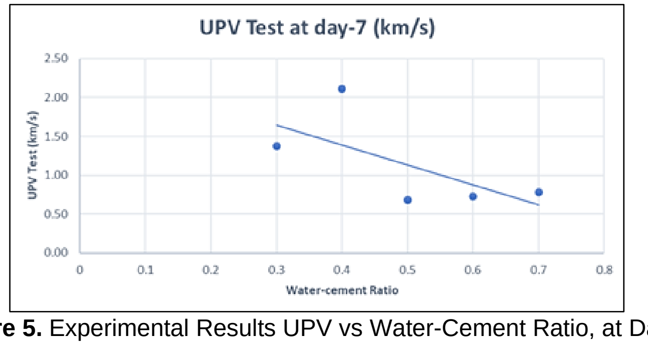

Figure 5. Experimental Results UPV vs Water-Cement Ratio, at Day 7

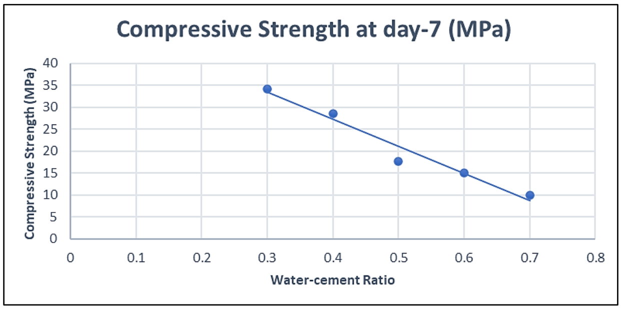

Figure 6. Experimental Results Compressive Strength vs Water-Cement Ratio, at Day 7

Density, UPV & Compressive Strength of Cement Mortars at Day 28

Table 6 illustrates the recorded values of density, compressive strength and UPV test when cement mortar achieved 28-day curing, for all water-cement ratios. The association between density and water-cement ratio variation in mortar mixes at day 28 is depicted in Figure 7. At day 28, Figure 9 depicts the relationship between compressive strength and water-cement ratio in various mortar mixtures. There was a definite pattern of decreasing density along with the compressive strength as the water-cement ratio increased for all mortar mixtures. Figure 8 shows the relationship between UPV test and water-cement ratio variation in mortar mixes at day 28. It can be seen that the value recorded for UPV at day 28 increased when compared to the cement mortar at day 7.

Table 6. Values of Density, Compressive Strength and UPV Test Recorded on Cement Mortar at Day 28

Water-Cement Ratio	Density at Day 28 (kg/m^3)	Compressive Strength at Day 28 (kg/m^3)	UPV Test at Day 28 ($kg/m^{3)}$
0.30	2182.93	35.17	3.02
0.40	2105.87	41.08	3.53
0.50	2069.60	27.47	2.58
0.60	2024.80	24.40	2.76
0.70	1929.33	11.09	2.13

By comparing the density values recorded for all cement mortar mixes on day 7 and day 28, the common approach was that raising the water-cement ratio would lead to a lower density. This occurred since the lower water-cement ratio, which was 0.3, included more cement and less water as compared to the other water-cement ratios, 0.4, 0.5, 0.6 and 0.7, which contained lower cement with higher water, Table 1. Cement hydration is a complicated chemical process that involves the transition from a suspension to a solid state. The ultrasonic velocity is not very sensitive to the formation of structure in the paste throughout the suspension phase. The water/air phase, particularly the air bubbles in the water, is the major component determining the UPV. The joining of smaller particles leads to clusters that create a percolating solid network as cement grains eventually disintegrate and nucleate. The route of ultrasonic pulse propagation changes from liquid to solid (Ye, Lura, Breugel & Fraaij, 2004).

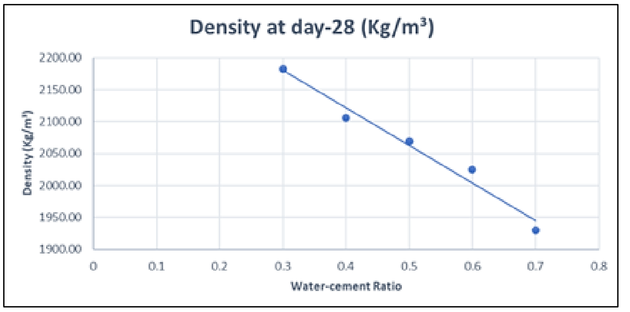

Figure 7. Experimental Results Density vs Water-Cement Ratio, at Day 28

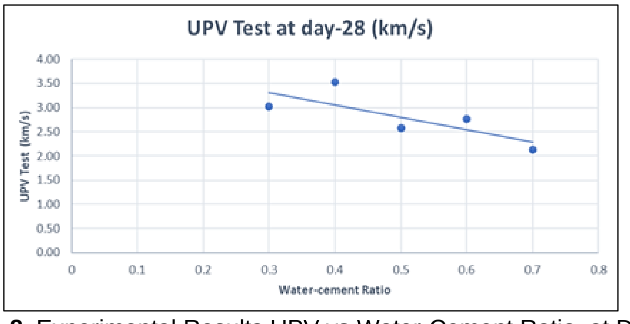

Figure 8. Experimental Results UPV vs Water-Cement Ratio, at Day 28

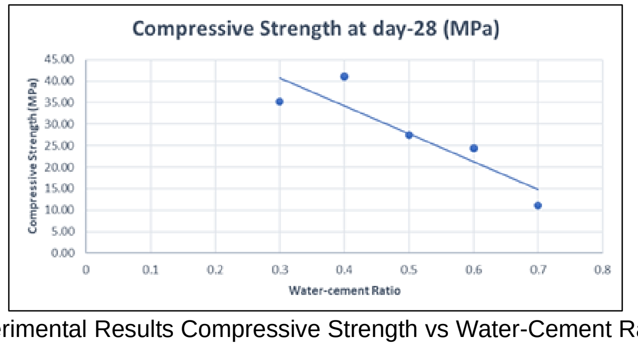

Figure 9. Experimental Results Compressive Strength vs Water-Cement Ratio, at Day 28

The UPV shows a considerable rise following the establishment of this solid percolation threshold, as the stiffness of the cement paste is heavily dependent on the solid phase link. As a result, it was determined why ultrasonic pulse velocity values for all mortar mixes on day 28 were greater than mortar mixes on day 7. Beyond this stage, the impact of the solid phase on the UPV takes precedence over the influence of air bubbles. The stiffness of a material has a significant impact on its UPV. Once the relationship between UPV and solid phase connection is established, further attributes like stiffness and strength may be acquired (Ye et al., 2004).

The compressive strength of water-cement ratio 0.3 recorded the highest value, 34.19 MPa at day 7 while 0.4 recorded 28.51 MPa, lower than the compressive strength of water-cement ratio 0.3. However, as the curing time increased to day 28, the compressive strength of 0.3, 35.17 MPa, recorded a value lower than 0.4. The highest water-cement ratio of 0.4 was recorded at day 28 with 41.08 MPa. This happened due to the presence of honeycomb recorded in the water-cement ratio 0.3 cement mortars, (Figure 10). While the water-cement ratio of 0.4 no honeycomb (Figure 11). Honeycombing in mortar specimens was a rough surface that contained voids in the mortar as a result of incomplete filling. It was also referred to as "hollow cavities" in the mortar mass where mortar could not be reached (Saidani & Roberts, 2007). In this experiment, honeycomb appeared due to the mortars' poor workability due to its low water content and lack of superplasticizers; the mortar was too stiff to pour into the cube silicone moulds.

Figure 10. The Presence of Honeycomb Recorded in Mortar Specimens of Water-Cement Ratio 0.3 After 28-Day of Curing

Figure 11. Mortar Specimens of Water-Cement Ratio 0.4 After 28-Day

CONCLUSION

This study focused on the experimental characterisation of several mortar mixes with varying water-cement ratios. The following primary conclusion may be reached from the evaluation of experimental results:

a) As the water- cement ratio increased, all tested attributes (density, compressive strength, and ultrasonic pulse velocity) decreased.
b) The compressive strength follows Abrams' law and exhibits appropriate power when compared to the water-cement ratio. Following Abram's law, a general variation of compressive strength with water-cement ratio may be provided for the design of mortar mixes ranging from lean to extremely strong as a function of the single biggest element impacting mortar strength, which is the water-cement ratio.

c) Mortars with a low water-cement ratio require the addition of superplasticizers in order to improve the workability of cement mortars, making it easier to pour the mortar paste into the mould.
d) A good mortar mix with good workability will result in a good mortar paste, which will have greater compressive strength.

REFERENCE

ASTM C 150-07. (2008) Standard Specification for Portland Cement, ASTM International.

ASTM C 109/C 109M-02. (2002). Standard Test Method for Compressive Strength of Hydraulic Cement Mortars (Using 2-in. in [50-mm] Cube Specimens). ASTM International.

British Standard. BS 882:1992. Specification for Aggregates from Natural Sources for Concrete.

British Standard BS 4551: Part 1:1998. Methods of Testing Mortars, Screeds and Plasters.

British Standard. BS EN 12504- 4:2004. Testing Concrete – Part 4: Determination of Ultrasonic Pulse Velocity.

Fernandes, V., Silva, L. Ferreira, V.M. & Labrincha, J.A. (2005). “Evaluation of Mixing and Application Process Parameters of Single-Coat Mortars” in Cement and Concrete Research, Vol. 35. pp. 836-841.

Haach, V.G., Vasconcelos, G. & Lourenco, P.B. (2011). “Influence of Aggregates Grading and Water/Cement Ratio in Workability and Hardened Properties of Mortars” in Construction and Building Materials, Vol. 25. pp. 2980-2987.

Haach, V.G., Vasconcelos, G., Lourenco, P.B. & Mohamad, G. (2010). “Influence of the Mortar on the Compressive Behaviour of Concrete Masonry Prisms” in Mecanica Experimental, Vol. 18. pp. 79-84.

Ismail, T. N. H. T., Yuriz, Y., Hassan, Azida, N., Saji, N., Jusoh, W. W., & Rahman, N. K. A. (2021). Experimental Study on Strength Performance of Soil Reinforced with Coconut Fibre for Panchor–Muar Road. Malaysian Construction Research Engineering Technology International Conference 2020, 13(2), 43–52.

Ji-Kai, Z. & Li-Mei, G. (2015). “Effect of Strain Rate and Water-to-Cement Ratio on Compressive Mechanical Behaviour of Cement Mortar” in J. Cent. South. Univ., Vol. 22. pp. 1087-1095.

Kim, Y.Y., Lee, K.M., Bang, J.W., Kwon, S.J. (2014). “Effect of W/C Ratio on Durability and Porosity in Cement Mortar with Constant Cement Amount” in Advances in Materials Science and Engineering, Vol. 2014. Id. 273460.

Lim, S. K., Tan, C.S., Chen, K.P., Lee, M.L. & Lee, W.P. (2013). “Effect of Different Sand Grading on Strength Properties of Cement Grout” in Construction and Building Materials, Vol. 38. pp. 348-355.

Markeset, G. & Hillerborg, A. (1995). “Softening of Concrete in Compression – Localization and Size Effects” in Cement and Concrete Research, Vol. 25. pp. 702- 708.

Mohamad, G., Neto, A.B., Pelisser, F., Lourenco, P.B. & Roman, H.R. (2009). “Mechanical Characterization of Laying Mortars for Structural Masonry – Prediction and Failure Mode” in Revista Materia, Vol. 14. pp. 824-844.

Neville, A.M. (1995). Properties of Concrete: 4th and Final Edition. Longman House, Burnt Mill, England.

Ortiz, J., Aguado, A., Agullo, L., Garcia, T. & Zermeno, M. (2009). "Influence of Environmental Temperature and Moisture Content of Aggregates on the Workability of Cement Mortar" in Construction and Building Materials, Vol. 23. pp. 1808-1814.

Rao, G.A. (2001). "Generalization of Abrams' Law for Cement Mortars" in Cement and Concrete Research, Vol. 31. pp. 495-502.

Reddy, B.V.V. & Gupta, A. (2018). "Influence of Sand Grading on the Characteristics of Mortars and Soil-Cement Block Masonry" in Construction and Building Materials, Vol. 22. pp. 1614- 1623.

Saidani, M. & Roberts, M.W.L. (2007). "Experimental Investigation of Honeycomb Constructional Elements" in Asian Journal of Civil Engineering (Building and Housing), Vol. 8. pp. 125- 132.

Schulze, J. (1999). "Influence of Water- Cement Ratio and Cement Content on The Properties of Polymer-Modified Mortars" in Cement and Concrete Research, Vol. 29. pp. 909-915.

Seart, L.K.A., Dewst, J., Kite, B., Harris, F.C. & Troy, J.F. (1996). "Abrams Law, Air and High Water-to-Cement Ratios" in Construction and Building Materials, Vol. 10. pp. 221-226.

Singh, S.B., Munjal, P. & Thammishetti, N. (2015). "Role of Water/Cement Ratio on Strength Development of Cement Mortar" in Journal of Building Engineering, Vol. 4. pp. 94-100.

Yeh, I. (2006). "Generalization of Strength Versus Water-Cementitious Ratio Relationship to Age" in Cement and Concrete Research, Vol. 36. pp. 1865- 1873.

Ye, G., Lura, P., Breugel, K.V. & Fraaij, A.L.A. (2004). "Study on the Development of the Microstructure in Cement-Based Materials by Means of Numerical Simulation and Ultrasonic Pulse Velocity Measurement" in Cement & Concrete Composites, Vol. 26. pp. 491- 497.

Zhou, J., Chen, X., Wu, L. Kan, X. (2011). "Influence of Free Water Content on the Compressive Mechanical Behaviour of Cement Mortar Under High Strain Rate" in Sadhana – Indian Academy of Sciences, Vol. 36. pp. 357-369.

Zivica, V. (2009). "Effects of the Very Low Water/Cement Ratio" in Construction and Building Materials, Vol. 23. pp. 3579- 3582

BEHAVIOUR OF REINFORCED CONCRETE BEAM CONTAINING EPS AND POFA SUBJECTED TO THREE POINT BENDING USING CONCRETE DAMAGE PLASTICITY (CDP) MODEL

Mohamad Hairi Osman[1], Suraya Hani Adnan[1], Shahrul Niza Mokhatar[2], Mohd Luthfi Mohd Jeni[1], Peniel Ang Soon Ern[1], Wan Amizah Wan Jusoh[1], Nur Faezah Yahya Hannifah Tami[2] and Salman Salim[3]

[1]*Faculty of Engineering Technology, Universiti Tun Hussein Onn Malaysia, Batu Pahat, Johor, Malaysia*
[2]*Faculty of Civil and Environmental Engineering, Universiti Tun Hussein Onn Malaysia, Batu Pahat, Johor, Malaysia.*
[3]*Centre for Diploma Studies, Universiti Tun Hussein Onn Malaysia, Batu Pahat, Johor, Malaysia.*

Abstract

A study is conducted to develop reinforcing concrete (RC) beam technology using Expanded Polystyrene (EPS) and Palm Oil Fuel Ash (POFA) as replacement materials for sand and cement. The heavy of existing concrete and the use of high cement are the main factors for this study to be carried out. POFA can be used as constituents in concrete due to the pozzolanic properties and EPS has the potential to be used in concrete as structural elements to reduce the density of concrete. The RC beams containing EPS and POFA as replacement materials with a percentage between 10% and 30% were studied in terms of crack. RC beam's size was 150mm x 150 mm x 1000mm and simply supported at spaced 750mm apart. In this paper, the simulation of Finite Element Analysis by using ABAQUS was performed to study the non-linear behaviour of concrete containing EPS and POFA by Concrete Damage Plasticity (CDP) model. In this model, concrete's tensile cracking and compression crushing for every percentage of EPS and POFA were considered as a data input in ABAQUS software. For RC beams with percentages of 10% to 30% EPS and POFA that were put through a three-point bending test and load versus displacement curves were produced. The simulation result shows that the cracks of RC beam may be classified as shear cracks based on the crack angle. The first crack at mid span led to the development of larger cracks. Without EPS, RC Beams with 10% POFA have a crack pattern quite similar to the control beam's. The concrete without EPS that contains 10% POFA displays a near ultimate load to normal concrete and demonstrates that concrete containing 10% POFA may withstand the same ultimate load as normal concrete. RC beam containing 10% POFA and 10% EPS also indicating close performance to normal concrete in term of capacity to bear ultimate load.

Keywords: *Palm Oil Fly Ash; expanded polystyrene; concrete damage plasticity; three point bending.*

INTRODUCTION

The Finite Element Method (FEM) is a numerical approach used in the Finite Element Analysis (FEA), which is the modelling of any given physical phenomena. Finite Element Analysis (FEA) has been used widely to analyse structures and material behaviour. FEA is highly efficient analytical tools for studying behaviour of structure, as an alternative to the experiment to reduce the cost and time. The goal of this study was to determine how much EPS and POFA should be utilised as a replacement to sand and cement in order to enhance or maintain the flexural performance of the RC beam base software simulation. In this study, three dimensional- nonlinear RC Beam model was developed. Software called ABAQUS was used because it can simulate reinforced concrete's structural behaviours. Concrete Damage Plasticity Model (CDP) were used in this study. The typical characteristics of concrete containing varying percentages of EPS and POFA, which were discovered from experiment, were utilized to establish FEA's simulation of the structural behaviours of a reinforced concrete beam. To explore the behaviours of reinforced concrete beams containing EPS and POFA under three point loads, a three-dimensional nonlinear finite element model was developed and analysed using static technique, which is accessible in ABAQUS software.

LITURATURE REVIEW

ABAQUS has the capability in problem solutions related to simulation because of a large range of material models, including those for concrete damage and metal plasticity, as well as capabilities for nonlinear implicit and explicit dynamic analysis. Additionally, modal and buckling analysis, response spectrum analysis, and random response analysis are also capabilities of ABAQUS. Finally, for modelling reinforcement, ABAQUS may embed components and rebar with pre-stress.

It provides precise, high-performance solutions for difficult linear dynamics applications, routine design simulations, and complex nonlinear challenges. The automobile, aerospace, and industrial goods sectors also utilize ABAQUS. The product's extensive range of material modelling capabilities and adaptability make it popular among academic and research institutes. ABAQUS is appealing for production-level simulations where various fields must be linked because it offers a good selection of multiphase capabilities, including coupled acoustic-structural, piezoelectric, and structural-pore capabilities. Since ABAQUS was primarily created to address non-linear physical behaviour, it contains a wide variety of material models, including the ability to represent elastomeric (rubber-like) materials.

Rahman et al. (2019) carried out experimental effort to undertake three-dimensional non-linear modelling of reinforced foamed concrete beam integrating 20% Palm Oil Fuel Ash and 5% and 10% Eggshell Powder as partial cement replacement employing concrete damage plasticity failure in ABAQUS/CAE software. The simulated outcomes showed that the suggested finite element modelling was effective in correctly forecasting the damage behaviour of foamed concrete.

According to Earij et al. (2017), who used ABAQUS software to simulate a fiber-reinforced concrete beam owing to the concrete damage plasticity (CDP) model, projected load defection curves closely match the values of the corresponding experimental beams. In spite of the linear law's minor disregard of starting stiffness, the deflection curves demonstrated excellent agreement with the experimental response in the post-yielding phase. Another study by George et al. (2017) examined the behaviour of a plain concrete beam utilizing concrete damage plasticity with various meshes. Despite the fact that the test peak curve for triangular mesh was steeper than that of quadrilateral mesh, the results of the flexural strength were in good accord with those of standard laboratories.

MATERIALS AND METHODS

Modelling of The Reinforced Concrete Beam

The proposed FEA model of Reinforced concrete beam is a three dimensional-nonlinear material model. The model was developed and analysed by quasi static technique using ABAQUS explicit module. Reinforced concrete beam with various of concrete properties containing 10%, 20%, 30% EPS and 10%, 20%, 30%, POFA for replacement level were analysed using the same structural model. Using several element types according to each element's appropriateness, each part of a reinforced concrete beam was independently simulated in the part module of the ABAQUS program. Table 1 lists the elements utilized for each part. Specific geometry, element section properties, material information, load and boundary conditions, analysis types, and output requests were all considered during the modelling process. The reinforced concrete beam was constructed using each component's finite-difference geometry. As shown in Figure 1, the steel reinforcement was modelled with three-dimensional 2 nodes components because to the complicated reinforcement configuration in the beam. The cross section area and material parameters of the reinforcing region were assigned and included in the study. Data from experiment results and previous research were used to give material properties to each component.

Table 1. Element Used for Each Parts of Reinforced Concrete Beam

Part	Element	Definition of Element
Beam	C3D8R	Three-dimensional 8-node linear
Rebar	B31	Node linear beam in space
Reinforcement	T3D2	Three dimensional 2 nodes truss element
Stirrup	B31	Node linear beam in space.

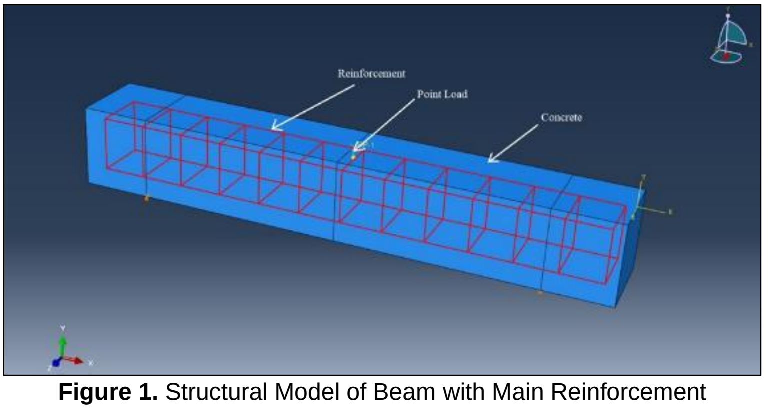

Figure 1. Structural Model of Beam with Main Reinforcement

After all the parts had been assigned with section and material properties, all parts were assembled. After the reinforced concrete beam model was put together, each modelled part was appropriately linked to the other. Tie contact technique was utilized to create proper interaction between reference point (RP) with the concrete as shown in Figure 2. The reference point (RP) and concrete components were joined together using the tie technique. Reference point (RP) was used as medium to transfer point load to beam. Embedded method was used to link the stirrup with a solid element to the main reinforcement. The technique for constraint the main reinforcement to the solid element representing concrete shown in Figure 3.

The boundary condition at Bottom of beam was assigned as pin support and roller support as shown in Figure 4. The distance between supports were 750 mm. Loading was placed at reference point (RP) and transfer to beam. Lastly, the mesh was assigned to the Reinforce Concrete Beam. The appropriate mesh size for model was used. Jobs had been created to do the analysis on beam. The field out parameter was defined such as deflection, and crack pattern.

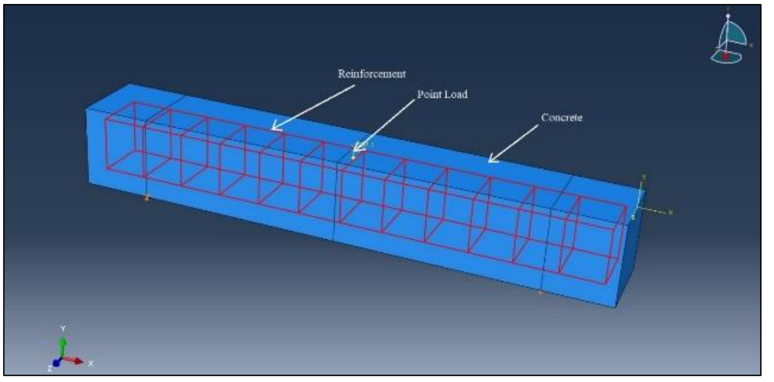

Figure 2. Structure Model with Reference Point (RP) at Point Load

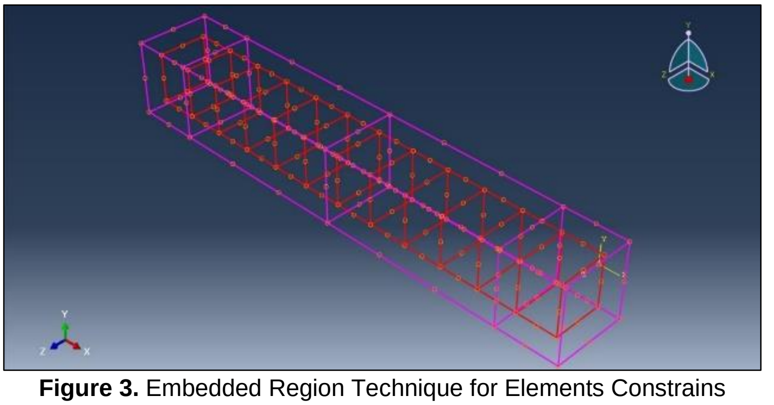

Figure 3. Embedded Region Technique for Elements Constrains

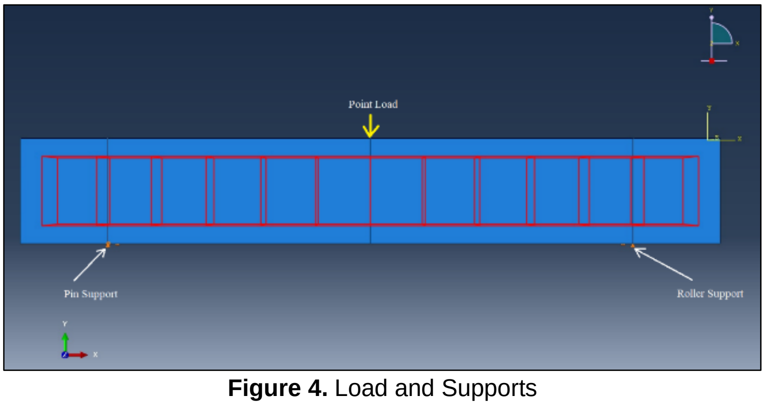

Figure 4. Load and Supports

Parameters of Reinforced Concrete Beam

Reinforced Concrete Beam with Size 150mm x 150mm x 1000mm with support 750mm support to support length were simulated as Figure 5 and Figure 6. All specimens were simulated with different percentage of EPS and POFA in concrete.

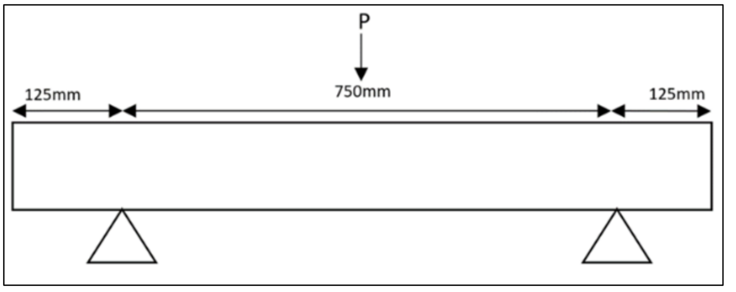

Figure 5. Load and Supports

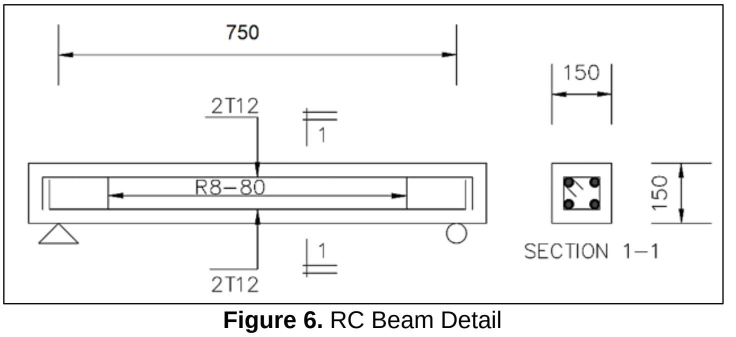

Figure 6. RC Beam Detail

Modelling of Material Properties

Eleven different types of material characteristics were taken into account, including those of normal concrete and EPS-POFA concrete with varying EPS and POFA content. In order to determine the concrete damage plasticity parameters as input to the model, the material characteristics for EPS-POFA concrete and reinforcement were collected by experimentation. From the experiment, the compressive strength, the tensile strength, the Young's modulus, the mass density, and the poisson ratio of EPS-POFA concrete were determined.

The constitutive parameters utilized in the concrete damaged plasticity model for the EPS-POFA concrete material's compressive and tensile behaviours are shown in Table 2. Default values were used to determine parameters that were not measurable in the experiment for normal concrete, as indicated in Abaqus 2016. The data in Table 2 were also based on previous study done by Lee & Fenves (1998) and Lubliner et al. (1989).

The Inelastic Strain is material parameter used in concrete damage parameter for normal concrete in Table 3 and Table 4 were obtained from experimental result and were used in Abaqus software for analysis and verification. The concrete damage parameter data for concrete with different percentage of EPS and POFA are attached in appendix. The damage parameters *dc* were calculated based on Equation 1. Where dc is the damage parameter of EPS-POFA concrete in compression and tension, σi is the initial stress and σcu is the ultimate stress.

$$dc = 1 - \frac{\sigma i}{\sigma cu} \tag{1}$$

Table 2. Concrete Damage Plasticity for Normal Concrete

Dilation Angle	Eccentricity	Initial Biaxial/ Uniaxial Ratio	k	Viscosity Parameter
31°	0.1	1.16	0.667	0.00005

Table 3. Material Parameter Used in Concrete Damage Parameter for Normal Concrete Subjected to Compression

Compressive Behaviour		
Yield Stress (MPa)	**Inelastic Strain**	**Damage Parameter, *dc***
22.066624	0	0
22.632435	0.001000	0
23.198246	0.001043	0
23.764057	0.001087	0
24.329868	0.001130	0
24.895679	0.001174	0
25.210269	0.001217	0
25.179311	0.001240	0.001228
25.031569	0.001270	0.007088
24.854194	0.001290	0.014124
24.446394	0.001320	0.030300
24.266913	0.001330	0.037420

Table 4. Material Parameter Used in Concrete Damage Parameter for Normal Concrete Subjected to Tension

Tensile Behaviour		
Yield Stress (Mpa)	**Cracking Strain**	**Damage Parameter, *dc***
2.34	0	0
2.90	0.000093	0
2.61	0.000111	0.056180
2.34	0.000119	0.101124
2.08	0.000127	0.146067

Stress-Strain Curve

Figure 7 shows the effect of EPS and POFA on the stress-strain behaviour for all twelve concrete samples. This sample is sample 1 from three samples taken and put in the stress-strain graph. The vertical strain gauge's through the displacement were used to measure the axial strain, and axial stress and strain graphs were then plotted against one another. All the diagrams appeared to have the same shape as normal concrete. Beginning with a linear range, it transitioned to a nonlinear response as the stress increased for strain gain until the maximum stress. Afterwards, stress decreased inelastically while strain increased. Figure 7 also shows concrete's stress-strain curves change gradually when the EPS-POFA content increases. The stress-strain of concrete containing 10% POFA without EPS seems almost close to normal concrete at the beginning and the peak stress and strain seem proximity to normal concrete with peak stress and strain values of 25.46 MPa and 0.001211mm/mm compared to normal concrete with peak stress and strain value 25.21MPa and 0.001217 mm/mm. The increase of EPS-POFA caused the lower maximum peak and give a smaller initial slope of curves. According to known theories, a smaller maximum peak may cause a lower compressive strength, while a smaller initial slope may cause a smaller elastic modulus. The slope of the curve, which is lower than that of normal concrete, indicates that EPS-POFA concrete performed more ductility and had a greater capacity for absorbing energy than normal concrete. This trend is consistent with a previous study by Cui et al. (2016) which stated a descending branch of the stress-strain curve showed that EPS concrete's stress decreased slowly as the strain increased. When concrete containing EPS is compressed, the condition of failure is more delayed, and the concrete can continue to support weight after failure without completely collapsing. As a result, EPS-contained concrete might be used to absorb vibrations. The same kind of failure was also noted by Babu, (2003) for EPS concrete.

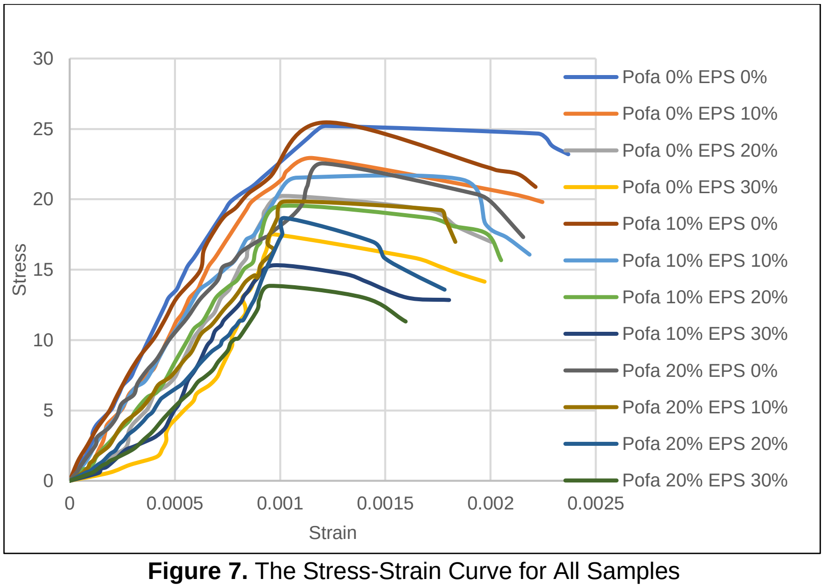

Figure 7. The Stress-Strain Curve for All Samples

Material Properties of Main Reinforcement and Shear Link

Based on laboratory tensile results, the elastic and plastic characteristics of the 6mm and 12mm diameter bars utilized for the shear link and primary reinforcement were determined. Initial yield stress, ultimate stress, strain at failure, Modulus' Young, mass density, and Poisson ratio were among the values utilized in the FEA. Table 5 contains a summary of all the material properties. Failure mode of reinforcement is assumed as plastic deformation with strain hardening after elastic stage.

Table 5. Mechanic Properties of Steel Assigned for Reinforced and Shear Link in RC Beam

Bar Diameter, Ø (mm)	Initial Yield Stress, σy (MPa)	Ultimate Stress, Pt (MPa)	Strain, ε	Modulus' Young, Es (kN/ mm^2)	Mass Density, ρ (kg/ m^3)	Poisson Ratio, v
12	359	600	0.00486	210	7800	0.3
8	343	485	0.0061	210	7700	0.3

FINITE ELEMENT ANALYSIS (FEA) VERTICAL LOAD VS DISPLACEMENT

Displacement of RC beam upon the reaching of ultimate load carrying capacity was recorded from FEA, it is an important parameter to study the behaviour of RC beam. Table 6 lists the ultimate load with maximum displacement of RC Beam recorded for various percentage of EPS and POFA.

Table 6. FEA Displacement of RC Beam with Various Percentage of EPS and POFA

RC Beam Containing EPS and POFA	% of EPS	% of POFA	FEA Ultimate Load, Pu (kN)	Maximum Displacement, mm
Normal Concrete	0%	0%	137.128	6.61
EPS-POFA Concrete 1	10%	0%	116.85	6.60
EPS-POFA Concrete 2	20%	0%	109.42	6.51
EPS-POFA Concrete 3	30%	0%	113.36	7.019
EPS-POFA Concrete 4	0%	10%	134.08	6.80
EPS-POFA Concrete 5	10%	10%	124.50	7.18
EPS-POFA Concrete 6	20%	10%	104.71	7.02
EPS-POFA Concrete 7	30%	10%	85.16	6.94
EPS-POFA Concrete 8	0%	20%	102.67	7.02
EPS-POFA Concrete 9	10%	20%	99.43	7.02
EPS-POFA Concrete 10	20%	20%	70.47	6.12
EPS-POFA Concrete 11	30%	20%	51.72	3.5

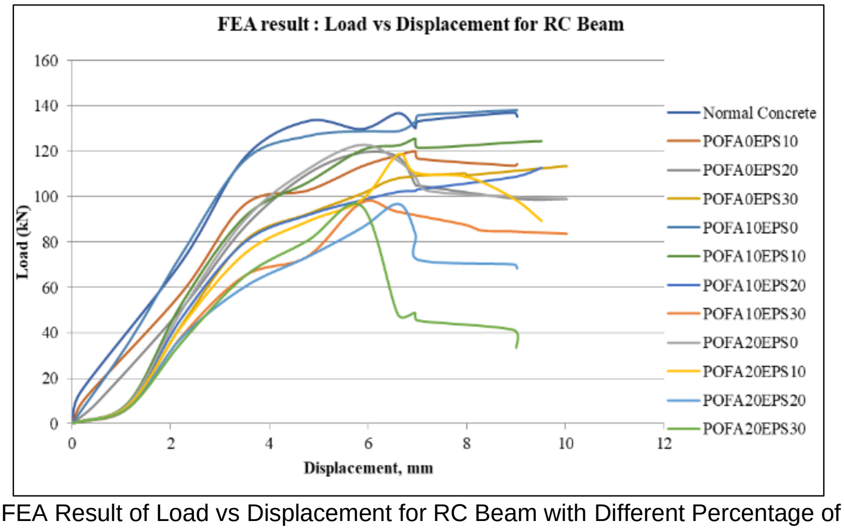

Figure 8. FEA Result of Load vs Displacement for RC Beam with Different Percentage of EPS and POFA

FEA result for load versus displacement of RC beam with various percentage of EPS and POFA were plotted in Figure 8. The trends of displacement were similar for all RC beams. Loading and displacement increased linearly from elastic until the RC beam upon the plastic stage. After that, the trend of curves becomes non-linear from plastic stage until ultimate load carrying capacity achieved upon the damage stage. Figure 8 shows that when the percentage of EPS increase from 10% to 30%, the ultimate load of RC beam had decreased. The ultimate load 0%, 20% and 30% EPS with 0% of POFA shows 137.128 kN, 116.85 kN and 109.42 kN respectively as shown in Table 6. The same decrease trend also occurred for other percentage of POFA with increasing of EPS. The concrete of 10% POFA without EPS shows the close ultimate load with normal concrete with gave 134.8 kN and it shows the 10% POFA in concrete was able to sustain same ultimate load compared to normal concrete. Tay et al. (1990) discovered the same outcome, the ideal POFA replacement level was proposed to be 10% in order to prevent any long-term effects on concrete strength development. In general, the presence of EPS in concrete causes the non-homogeneity of the concrete, which results in a loss in strength. Additionally, it appears that adding POFA to concrete that contains EPS does not assist to boost the strength of RC beams.

Crack Pattern of RC Beam From FEA

Generally, FEA failure mode of Normal RC beam and EPS-POFA RC beam in FEA can be classified flexural and shear crack due to the angle of crack close to 45 degrees. Major cracks were developed from the first crack near mid span. Crack pattern of EPS-POFA RC Beam is tabulated in Table 7. It can be seen that, most of specimen shows shear crack due to the angle of crack close to 45 degrees.

Table 7. Crack Pattern of RC Beam with Various Percentage of EPS and POFA in FEA

RC Beam	POFA (%)	EPS (%)	Crack Pattern
1	0.00	0.00	Flexural cracking
2	0.00	20.00	Shear cracking
3	10.00	0.00	Flexural cracking
4	10.00	20.00	Shear Cracking
5	20.00	0.00	Flexural and Shear cracking
6	20.00	20.00	Shear cracking

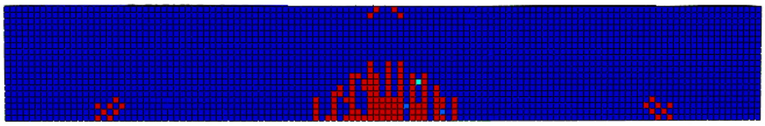

Figure 9. Crack Pattern of Normal Reinforced Concrete Beam

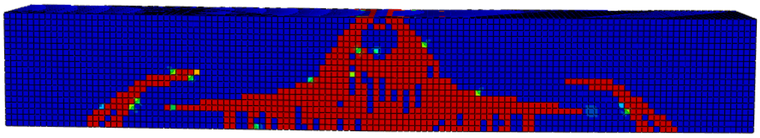

Figure 10. Crack Pattern of Reinforce Concrete Beam Containing 0% POFA and 20% EPS

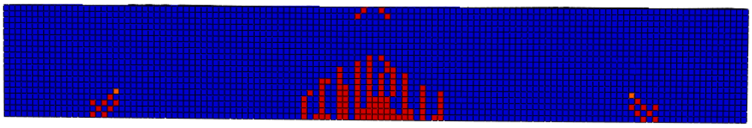

Figure 11. Crack Pattern of Reinforcement Concrete Beam Containing 10% POFA and 0% EPS

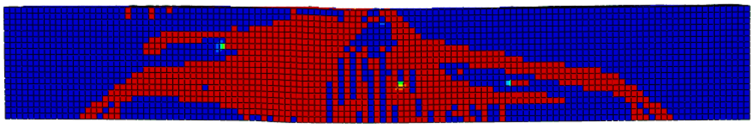

Figure 12. Crack Pattern of Reinforcement Concrete Beam Containing 10% POFA and 20% EPS

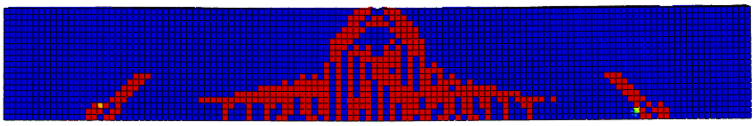

Figure 13. Crack Pattern of Reinforcement Concrete Beam Containing 20% POFA and 0% EPS

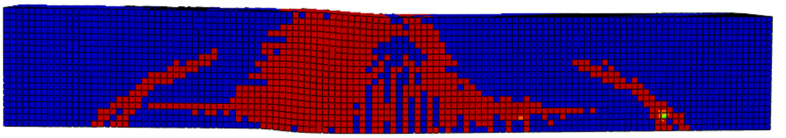

Figure 14. Crack Pattern of Reinforcement Concrete Beam Containing 20% POFA and 20% EPS

For control beam as shown in Figure 9, it is evident that the center portion is where the main cracking occurs. The failure zone showed signs of cracking, and the concentration also occurred in the support and center region, spreading diagonally toward flexural failure. Next, it can be seen that the cracking started in the middle and moved up to the top surface. RC Beams with 10% POFA without EPS as shown in Figure 11 also failed similar to the control beam. Major cracks were developed from the first crack near mid-span. The pattern of cracking begins to change to shear cracking as the percentage of EPS increases up to 20% and above for all specimens as shown in Figure 12. Shear cracks were developed when the acting shear on the section exceeds the resisting shear capacity in certain situations. High EPS content can cause the shear capacity of the concrete to be low. According to Herki & Khatib (2017) the mechanism of failure was mostly a shear failure and the deflection grew as the replacement levels of EPS rose, regardless of the reinforcing arrangement. However, the involvement of POFA in the reinforcement concrete beam with 10% in Figure 11, shows the crack width had been reduced. Based on Altwair et al. (2014), the loss of flexural strength and flexural deflection capacity tends to diminish as POFA rises, which might be explained by a reduction in the crack width. The pattern of cracking seem also begins to bigger shear cracking as the percentage of FOFA increases up to 20% and above for all specimens but the FEA ultimate load for the RC beam containing 10% POFA seem close with control RC beam and this means that RC Beams with 10% POFA may improve flexural strength at the initial stage.

CONCLUSION

RC beam containing 10% POFA without EPS is seen to have almost the same capacity as control RC beam in simulation result. RC Beam containing 10% POFA can be observed has the highest bending resistant at ultimate load compared to other specimens. The ultimate load capacity of the RC beam appears to be reduced when EPS-POFA increases in the RC beam. The high level of porosity in concrete with POFA, which causes stress concentration and weakens cement and aggregate, may be to responsible for the decreased ultimate load. This may be connected to concrete's porous structure with POFA, which caused stress concentration and weakened the link between aggregate and paste. The feature of EPS not assisting the bonding between cement and aggregate has also contributed to the decrease of the ultimate load for EPS-POFA RC beams. Moreover, it was discovered that as the EPS volume % increased, the flexural strength of EPS concrete decreased linearly. Due to the presence of EPS particles, the flexural section height is reduced, which is the main cause of the drop in flexural strength.

ACKNOWLEDGEMENT

The author would like to give truthful recognition to Office for Research Management Centre (RMC), Universiti Tun Hussein Onn Malaysia, for the commitments, especially on giving the budget for a fee through the TIER 1 research grant (Grant Code H932).

REFERENCES

Altwair, N. M., Johari, M. A. M., & Hashim, S. F. S. (2014). Influence of treated palm oil fuel ash on compressive properties and chloride resistance of engineered cementitious composites. Materials and Structures/Materiaux et Constructions, 47(4), 667–682.

Babu, K. G., & Babu, D. S. (2003). Behaviour of lightweight expanded polystyrene concrete containing silica fume. Cement and Concrete Research, 33(5), 755–762.

Cui, C., Huang, Q., Li, D., Quan, C., & Li, H. (2016). Stress-strain relationship in axial compression for EPS concrete. Construction and Building Materials.

Earij, A., Alfano, G., Cashell, K., & Zhou, X. (2017). Nonlinear three–dimensional finite–element modelling of reinforced–concrete beams: Computational challenges and experimental validation. Engineering Failure Analysis, 82(July), 92–115.

George, J., Kalyana Rama, J. S., Siva Kumar, M. V. N., & Vasan, A. (2017). Behavior of Plain Concrete Beam subjected to Three Point Bending using Concrete Damaged Plasticity (CDP) Model. Materials Today: Proceedings, 4(9), 9742–9746.

Hamada, H. M., Jokhio, G. A., Yahaya, F. M., & Humada, A. M. (2018). Properties of fresh and hardened sustainable concrete due to the use of palm oil fuel ash as cement replacement. IOP Conference Series: Materials Science and Engineering, 342(1).

Herki, B. A., & Khatib, J. M. (2017). Valorisation of waste expanded polystyrene in concrete using a novel recycling technique. European Journal of Environmental and Civil Engineering.

Hossain, M. M., Karim, M. R., Hossain, M. K., Islam, M. N., & Zain, M. F. M. (2015). Durability of mortar and concrete containing alkali-activated binder with pozzolans: A review. Construction and Building Materials, 93, 95–109.

Huang, Z., & Liew, J. Y. R. (2015). Nonlinear finite element modelling and parametric study of curved steel-concrete-steel double skin composite panels infilled with ultra-lightweight cement composite. Construction and Building Materials.

Lee, J., & Fenves, G. L. (1998). Plastic-Damage Model for Cyclic Loading of Concrete Structures. Journal of Engineering Mechanics, 124(8), 892–900.

Lubliner, J., Oliver, J., Oller, S., & Onate, E. (1989). A Plastic-Damage Model. International Journal of Solids and Structures, 25(3), 299–326.

Rahman, A. F., Goh, W. I., & Jhatial, A. A. (2019). Flexural study of reinforced foamed concrete beam containing palm oil fuel ash (POFA) and eggshell powder (ESP) as partial cement replacement. International Journal of Sustainable Construction Engineering and Technology, 10(1), 93–100.

Rahman, A. F., Goh, W. I., Mohamad, N., Kamarudin, M. S., & Jhatial, A. A. (2019). Numerical analysis and experimental validation of reinforced foamed concrete beam containing partial cement replacement. Case Studies in Construction Materials, 11.

Sayadi, A. A., Tapia, J. V., Neitzert, T. R., & Clifton, G. C. (2016). Effects of expanded polystyrene (EPS) particles on fire resistance, thermal conductivity and compressive strength of foamed concrete. Construction and Building Materials, 112, 716–724.

Syaizul, E., Abdullah, R., & Mirasa, A. K. (2019). Review on the Effect of Palm Oil Fuel Ash (POFA) on Concrete Review on the Effect of Palm Oil Fuel Ash (POFA) on Concrete. October.

Tangchirapat, W., & Jaturapitakkul, C. (2010). Strength, drying shrinkage, and water permeability of concrete incorporating ground palm oil fuel ash. Cement and Concrete Composites.

Tangchirapat, W., Jaturapitakkul, C., & Chindaprasirt, P. (2009). Use of palm oil fuel ash as a supplementary cementitious material for producing high-strength concrete. Construction and Building Materials.

Tangchirapat, W., Saeting, T., Jaturapitakkul, C., Kiattikomol, K., & Siripanichgorn, A. (2007). Use of waste ash from palm oil industry in concrete. Waste Management.

Tay, J. H. (1990). Ash from oil-palm waste as concrete material. Journal of Materials in Civil Engineering.

Tay, J. H., & Show, K. Y. (1995). Use of ash derived from oil-palm waste incineration as a cement replacement material. Resources, Conservation and Recycling.

Taylor, H. F. W. (1997). Cement chemistry. Cement Chemistry.

Tejaswini, T., & Raju, M. V. R. (2015). Analysis of RCC Beams using ABAQUS. International Journal of Innovations in Engineering and Technology (IJIET) Analysis, 5(3), 248–255.

Thomas, B. S., Kumar, S., & Arel, H. S. (2017). Sustainable concrete containing palm oil fuel ash as a supplementary cementitious material – A review. Renewable and Sustainable Energy Reviews, 80, 550–561.

STORMWATER DETENTION STRUCTURES IN THE VERANDA AND PARKING LOT AT COMMERCIAL CENTRE SUBJECTED TO HISTORICAL EXTREME RAINFALL EVENTS

Darrien Yau Seng Mah[1], Merry Shi Ting Tang[1] and Fang Yenn Teo[2]
[1]UNIMAS Water Centre, Faculty of Engineering, Universiti Malaysia Sarawak, Kota Samarahan, Sarawak, Malaysia.
[2]Faculty of Science and Engineering, University of Nottingham Malaysia, Semenyih, Selangor.

Abstract
This paper reports on a specifically designed stormwater detention structures that fit in a commercial centre, namely modular-based water micro tanks in the veranda and the parking lot in front of shop buildings. This is in line with the concept of integrating detention structures into urban features as small pockets to capture urban runoff along the stormwater flow path so that the amount of stormwater flowing downstream is reduced. The two designs were simulated using Storm Water Management Model and subjected to historical rainfall data, in which the selected storms were found to span more than 10 hours and with maximum hourly rainfall depths between 40 - 70 mm. Results from the modelling efforts were stormwater characteristics of the particular type of detention system in times of extreme rainfall events. The identified stormwater characteristics provide a guide to urban planners to mitigate urban flooding. It was found that the detention structures, although with a limited storage volume, were able to sustain an accumulated rainfall up to 60 mm, a feature 3 times higher than the 23 mm design rainfall. It was found that accumulated rainfall of a particular storm was a better indicator than the maximum rainfall depth of the storm to indicate the water storing capacity of detention structures.

Keywords: *Detention; Drainage; Flood; Sustainable Development; SWMM; Urban Runoff.*

INTRODUCTION

A stormwater detention structure is made to temporarily hold stormwater on the urban land surfaces (Bilodeau, Pelletier & Duchesne, 2018). Having detention structures embedded in the veranda and parking lot in a commercial centre are in line with the trends of integrating urban runoff management with urban features (Hamouz et al., 2020; Pour, Wahab, Shahid, Asaduzzaman & Dewan, 2020). This is due to the fact that congested urban environments had caused difficulty to source empty land spaces for stormwater structures (Shams et al., 2018; Maulana, Samad & Nordin, 2022). Four examples of the integrated structures are presented in the following paragraphs.

The first example showcases a roof detention (Figure 1a). This integration method made use of the building roof surfaces, one of the prominent features of cities, to capture stormwater. Generally, a storage layer was laid on a roof and channels were equipped to deliver overflowing water to the exit points (Campisano, Modica & Gullotta, 2020; Rey-Mahía, Álvarez-Rabanal, Sañudo-Fontaneda, Hidalgo-Tostado & Menéndez Suárez-Inclán, 2022).

The second example showcases high density polyethylene pieces which were embedded within a building floor slab (Figure 1b). This method targeted the buildings covering the urban landscape. The square pieces were hollow and interconnected with pipelines. Once completed, these pieces functioned as ground-level floor and water tanks which received water from the building itself (Rainey, Brody, Galloway & Highfield, 2021).

Retaining wall is an urban feature built as a solid wall to keep the soil behind it from sliding. The third example showcases concrete pieces which were laid as retaining wall (Figure 1c). Referring to the inlet of the figure, one could see that stones filled the gaps in between the concrete pieces instead of soil. The voids in between the stones play a role in holding the stormwater (Ostendorf, Morgan, Celik & Retzlaff, 2021).

The fourth example shows the most common integration to blend stormwater detention into roads and car parking spaces (Maurer et al., 2021; Xu, Liu & Ding, 2021). Hollow concrete pieces were replacing conventional tarred road structure (Figure 2d), in which the surfaces of the pieces supported vehicles and pedestrians alike, with service inlets to direct stormwater to the underground hollow chambers. In short, stormwater structures had been merged successfully into building roof, floor slab, retaining wall and roadway. These endeavours gave confidence to the current study to explore on veranda and parking lot in front of shops to house detention structures.

(Source: https://sustainabletechnologies.ca/) a) Rooftop Detention

(Source: https://www.aquacomb.com.au/) b) Building Floor Slab Detention

(Source: https://magnumstone.com) c) Retaining Wall Detention

(Source: https://oldcastleinfrastructure.com/) d) Road Subsurface Detention

Figure 1. Integrated Stormwater Structures

In the case study of this paper as depicted in Figure 2, manmade structures were designed with water holding capacity to replace the natural process of water infiltration to the soil layer that was depleted due to urbanization (Kaykhosravi, Khan & Jadidi, 2022; Yang, Zhang &

Krebs, 2022). Precast concrete pieces were used to create multiple micro water tanks (Figure 2b). These pieces were non-commercialized R&D product developed by Universiti Malaysia Sarawak and collaborators (Bateni et al., 2020). This paper focuses on commercial centre, in which the modular units were tried for the walkway under the veranda and parking lot (Figure 2c) (Mah, Bateni, Bustami, Adam & Salehe, 2021; Mah, Ayog & Salehe, 2022).) Each of the modular unit consisted of two hexagonal covers, in which nine covers made up of 1m^2 of surface area. A 0.3 m high hollow cylinder was stationed in between the covers, in which each was provided with a side outlet so that water would fill the entire detention system. Its effective water storing capacity was estimated at 0.19 m^3 for 1 m^2 of surface area (Mah et al., 2021). The small and compact size of the modular units allowed them to be installed as walkway under the veranda (3 m wide) and car parking lot (5 m wide) in front of, usually a row of shops.

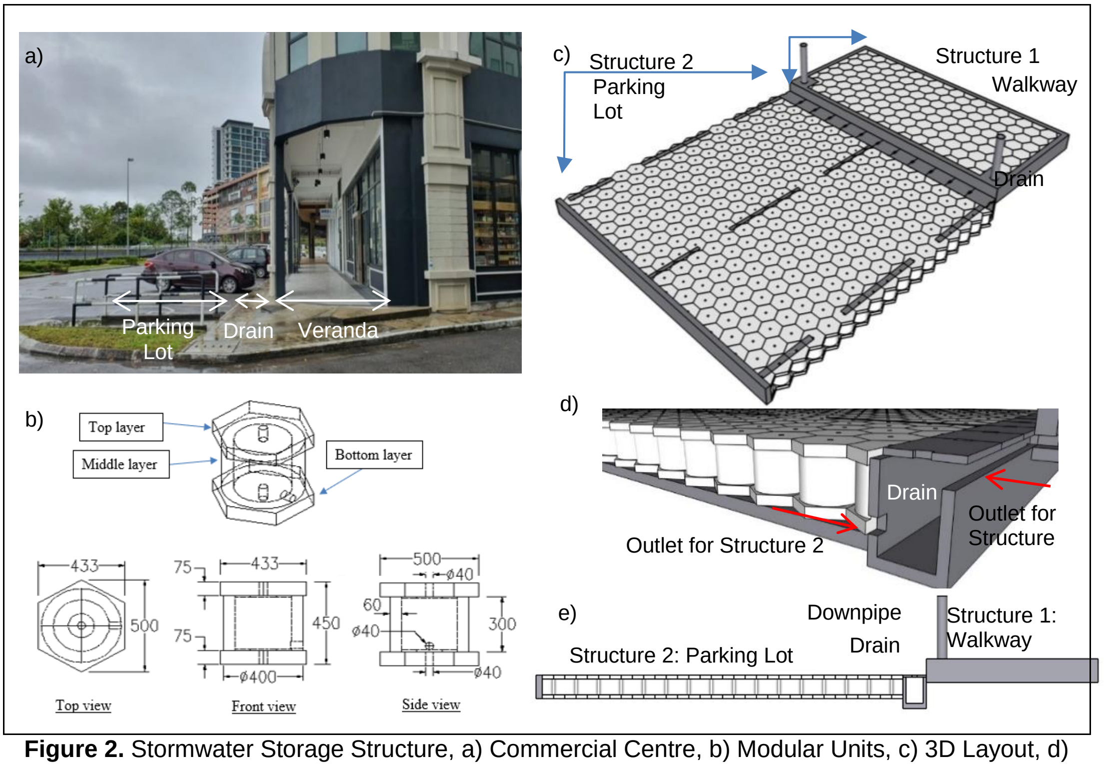

Figure 2. Stormwater Storage Structure, a) Commercial Centre, b) Modular Units, c) 3D Layout, d) Side View, and e) Cross Section View

The veranda detention which is termed as Structure 1 (Figure 2c), received stormwater from the building roof via downpipes. The parking lot detention which is termed Structure 2 (Figure 2c), received stormwater from the road surfaces. Eventually waters from the two were discharged to the perimeter drain that separated the two structures (Figure 2d).

The floor level of the shop was 0.07 m higher than the walkway while the walkway was 0.5 m higher than the car park (Figure 2e). The authors had investigated on veranda in Mah, Ayog and Salehe (2022) by subjecting the said structure to 5-min, 10-year Average Recurrent Interval (ARI) design rainfall (Table 1), following the recommendation of a Singaporean guideline (Singaporean Public Utilities Board [PUB], 2010). This paper is investigating further to use extreme rainfall events to check the combination of veranda and parking lot detention structures for overflowing of floodwaters that could inundate the shops.

Table 1. Studies of Veranda and Parking Lot Detention Structures

Source	Description
Mah et al., 2022	Veranda subjected to 23 mm design rainfall for 5 minutes.
Current study	Veranda and parking lot subjected to 40 – 70 mm historical rainfall, spanned over 10 hours, sourced from the Department of Irrigation and Drainage, Sarawak.

The structures in Mah et al. (2022) were designed as a flow-through system which the flow mechanism had the water flowed in and out at the same time. Such a flow mechanism allowed the small sizes of the structures. The applied design rainfall was intense from the beginning of the event but for short time span. It was found that the structures were able to contain the stormwater without overflowing. The current study applies the same structures but subjected them to historical extreme rainfall. The major difference of the extreme compared to design rainfall was the maximum rainfall and time span were higher and these were a test of time to the responses of the structures.

MATERIALS AND METHODS

Study Area

A commercial centre located in Kota Samarahan, Sarawak was selected as study area (Figure 3). The simple one-row shop building allowed measurement of the site conditions and easier interpretation of the stormwater management measures being explored (Xiong et al., 2019). Three measures were initiated (Figure 4).

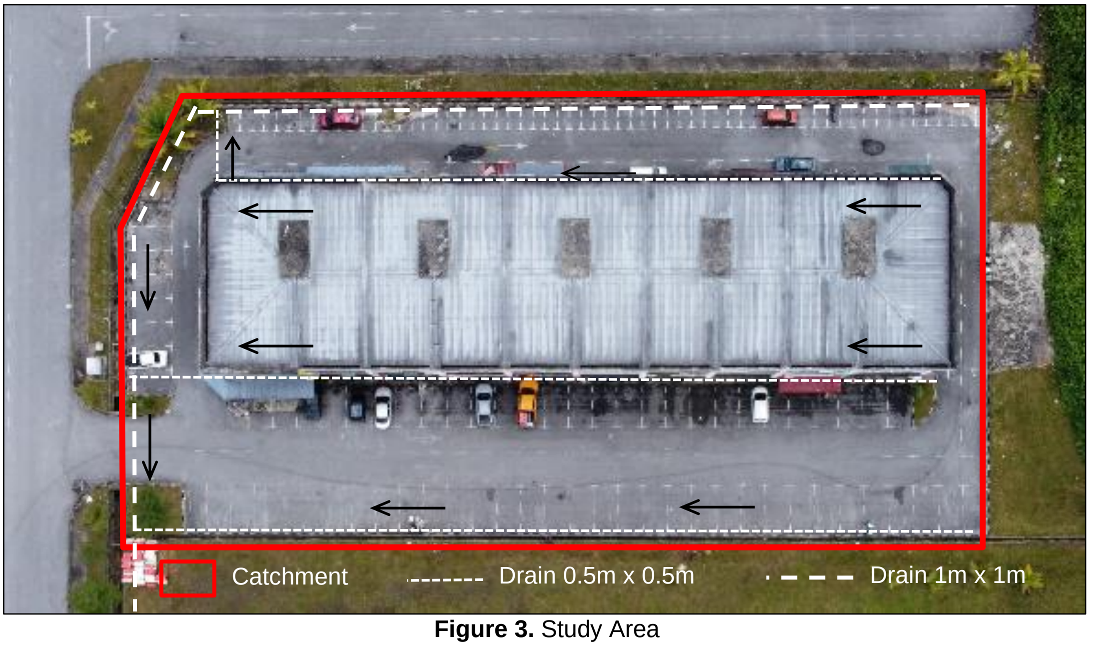

Figure 3. Study Area

Figure 4. Stormwater Detention, a) Measure 1, b) Measure 2, and c) Measure 3

Based on the measurement of land areas in the aerial photo taken by the research team, the commercial centre was found to have a total catchment area of 3,425 m^2. The shop building had 39% of the surface area, while the tarred surfaces surrounding the shop building had 61% of the surface area. There were 10 shop lots, in which the dimension of a corner lot was 9 m x 18 m, and an intermediate lot was 7 m x 18 m. The row was measured at 74 m in length.

Measure 1 was having the veranda detention only that received water from the front roof (9 m x 74 m) (Figure 4a); Measure 2 was having the car park detention only that received water from the parking lot surfaces (5 m x 74 m) (Figure 4b); Measure 3 was a combination of the earlier two measures (14 m x 74 m) (Figure 4c). The veranda detention was designed with a dimension of 3 m x 74 m and water storing capacity of 42 m^3. On the other hand, the parking lot detention was with a dimension of 5 m x 74 m and water storing capacity of 70 m^3.

Selected Historical Rainfall Events

Four historical extreme rainfall events recorded for Samarahan were selected (Table 2). These events happened during the Northeast Monsoon experienced by Sarawak. These events were reported with subsequent flooding at various parts of Samarahan areas.

Table 2. Selected Historical Extreme Rainfall Events Sourced from The Department of Irrigation and Drainage, Sarawak

Rainfall Event	Max Rainfall (mm)	Duration of Storm (hr)
Event 1: 18 Jan 2015	38.5	11
Event 2: 19 Jan 2015	43	14
Event 3: 17&18 Dec 2017	47.5	15
Event 4: 11&12 Dec 2019	70.5	15

Urban Stormwater Drainage Design

Urban stormwater management paid attention to the water flow mechanisms for pre- and post-development conditions. It was taken that the pre-development condition of a catchment was usually forested area (Figure 5a) which most of the runoff was infiltrated to the soil layer. On the other hand, it was taken that post-development condition was problematic due to the high volume of running water generated from the impervious surfaces (Figure 5b).

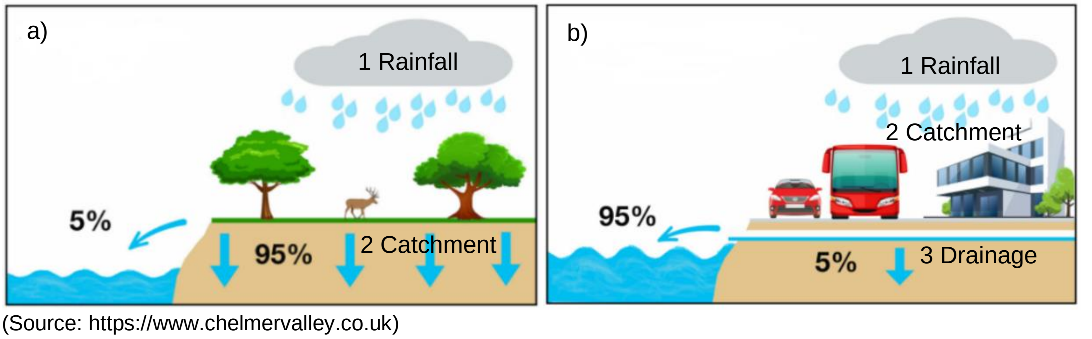

(Source: https://www.chelmervalley.co.uk)

Figure 5. Rainfall and Runoff Processes for a) Pre- and b) Post-Development Conditions

Referring to the Malaysian guideline (Malaysian Department of Irrigation and Drainage [DID], 2012), stormwater system started with rainfall which could be in the forms of design rainfall or historical rainfall. From the rainfall, it generated surface runoff on the catchment surfaces which was termed catchment flow. The mentioned catchment flow could be estimated using rational method:

$$Q_R = \frac{C.I.A_D}{360} \tag{1}$$

where,

QR = Catchment flow (m^3/s);
C = Runoff coefficient (unitless);
I = Rainfall intensity (mm/hr); and
AD = Drainage area (ha).

The rainfall intensity came from the selected design or historical rainfall events. For pre-development condition, a C value of at least 0.4 was applied to represent grassed land; and a C value of 1.0, for urban land. The drainage area could be estimated from the selected study area.

The catchment flow was usually directed to the urban drainage system. The design of the usually concrete drain could be referred to the Manning formula:

$$Q_M = \frac{1}{n} A_F R^{2/3} {S_F}^{1/2} \quad (2)$$

where,
QM= Drain flow (m^3/s);
N = Manning's roughness coefficient (unitless);
AF = Flow area of drain (m^2);
R = Hydraulic radius of drain (m); and
SF = Friction slope of drain (m/m).

Specific drainage components applied different equations according to the associated hydraulic processes. A stormwater detention structure was represented as the water balance of water in and out of the structure:

$$St = \sum_i (Q_i - Q_0) \Delta t_s \quad (3)$$

where,
St = Storage volume (m^3);
Qi = Inflow (m^3/s);
Qo = Outflow (m^3/s);
Ts = Duration of storm (s).

Storm Water Management Model

Storm Water Management Model (SWMM) version 5.0 was developed by the United States Environmental Protection Agency. The simulation engine of the software was modelling the hydrological and hydraulic processes from sky to land (Zeng, Yuan, Liang, Li, 2021). The catchment flow in SWMM applied a nonlinear differential equation of sheet flow:

$$Q_C = W \frac{1.49}{n} \left(d - d_p\right)^{5/3} {S_C}^{1/2} \quad (4)$$

where,
Q_c = Catchment flow (m^3/s);
W = Width of catchment (m);
S_c = Slope of catchment (m);
n = Manning roughness value (unitless);
d_p = Maximum depression storage (m);
d = Depth of water over the catchment (m).

SWMM used nodes and links to represent the drainage network. Once the catchment flow was directed to a node, the drain flow was routed from node to node through the channel using kinematic wave approximation:

$$Q_D = \frac{\partial A}{\partial t} + \alpha m A^{(m-1)} \frac{\partial A}{\partial x} \tag{5}$$

where,

Q_D = Routed drain flow (m^3/s);
A = Cross-sectional area of the drain (m^2);
x = Distance along the flow path (m);
t = Time step (s);
〈 = Flow geometry due to drain (unitless);
m = Surface roughness of drain (unitless).

Developed SWMM models of the study area with the three measures are presented in Figure 6. The main differences of the models were the placement of detention structure for the different measures. SWMM used storage unit to represent detention structures of various shapes and sizes by specifying the associated storage volumes (Equation 3). A storage unit was equipped with an orifice outlet which influenced by the orifice size and water level:

$$Q_O = A_O C_O \sqrt{2H_O g} \tag{6}$$

where,

Q_o = Flow from orifice outlet (m^3/s);
A_o = Orifice diameter (m^2);
C_o = Discharge coefficient of orifice (unitless);
H_o = Maximum head to centre of orifice (m);
g = Acceleration due to gravity (m/s^2).

Model Verification

Model verification was carried out by comparing the theoretical and modelled values of three major flow components, namely the catchment, storage and drain flows (Figure 7). Scattered plots of catchment flow (Figure 8a) produced a R square value of 0.67 which compared the rational method (Equation 1) with SWMM (Equation 4).

Next, the storage inflow (Figure 8b) produced a R square value of 0.65 which comparing the rational method (Equation 1) with SWMM (Equation 4). This was because the inlet to storage was close to the catchment. Therefore, the catchment flows were taken as the inflows. Take the parking lot detention, its surface area functioned as the catchment that drained water to the detention structure. Similarly, the veranda detention received water directly from the roof that functioned as catchment.

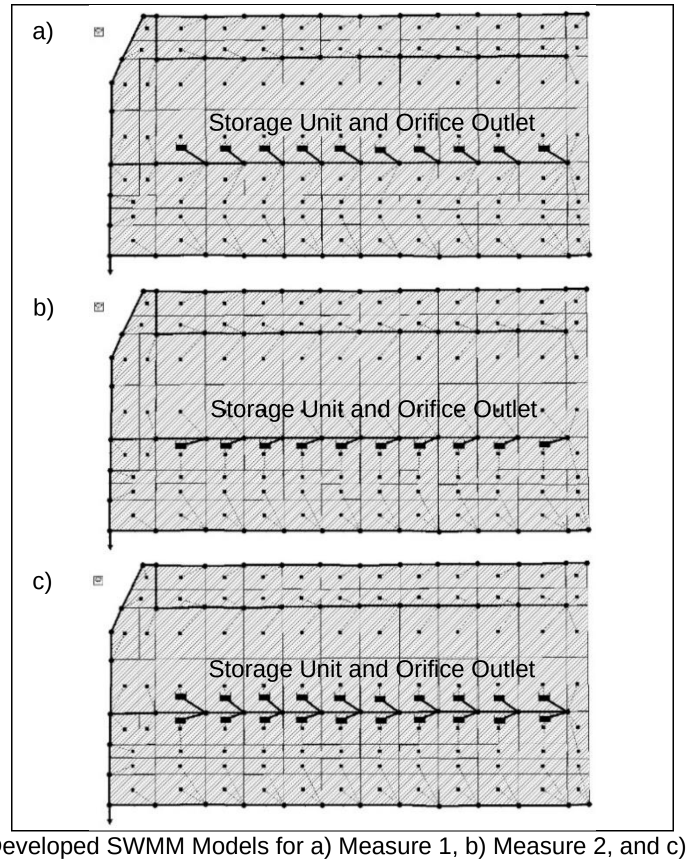

Figure 6. Developed SWMM Models for a) Measure 1, b) Measure 2, and c) Measure 3

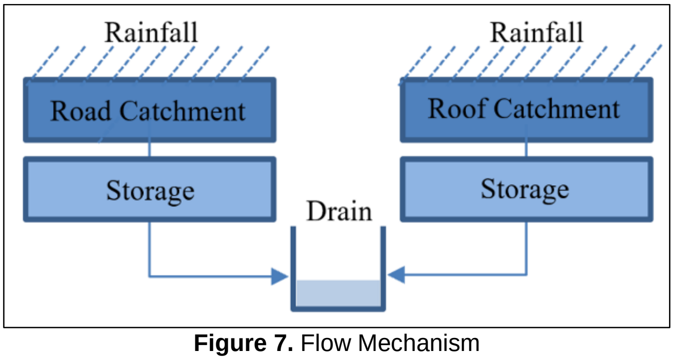

Figure 7. Flow Mechanism

On the other hand, drain flow (Figure 8c) had a R square value of 0.83 which compared the Manning formula (Equation 2) with SWMM (Equation 5). With these R square values greater than 0.6, the developed SWMM models were deduced to give reasonable estimation of the measures (Zakizadeh, Moghaddam Nia, Salajegheh, Sañudo-Fontaneda, Alamdari, 2022).

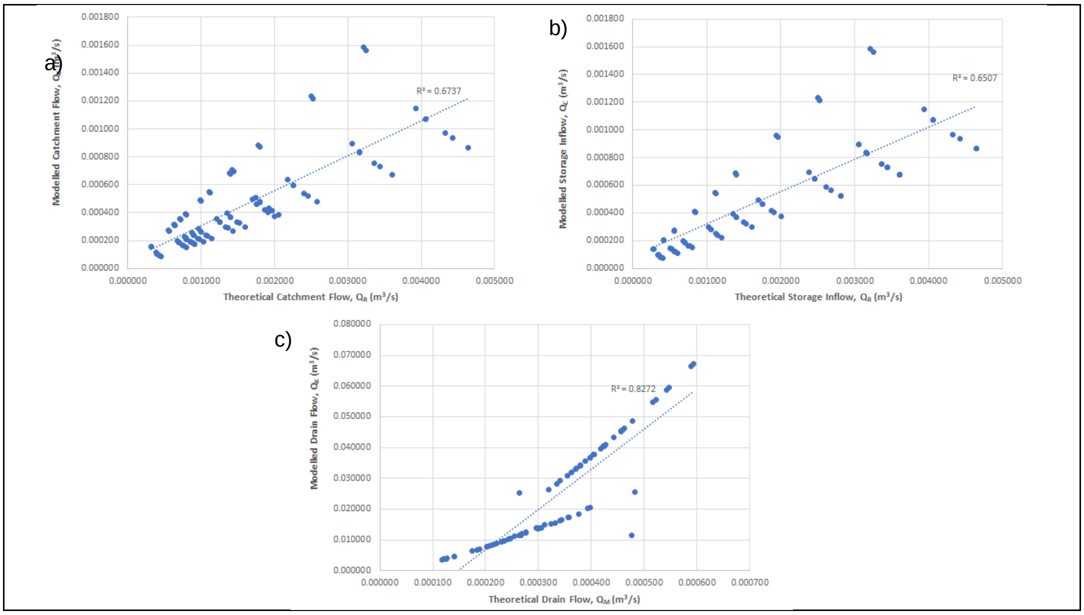

Figure 8. Scattered Plots of The Theoretical and Modelled Values for a) Catchment Flow, b) Storage Inflow and c) Drain Flow

RESULTS AND DISCUSSION

Flow Analyses at Outfall

The flow characteristics of the investigated measures in the commercial centre could be observed with the modelled flow hydrographs at the outfall (Figure 9). These hydrographs were the catchment-wide responses of the commercial centre. The modelled flow patterns from the four sub-figures were obvious with the post-development hydrographs the highest, pre-development hydrographs the lowest and the hydrographs due to the measures sandwiched in between. Measure 3 had the highest reduction of peak hydrographs from post-development conditions up to 30%. Besides, Measure 3 hydrographs were the nearest to the pre-development conditions.

For storm events with maximum rainfall depths between 40-50 mm (Events 1-3), the estimated post-development peaks ranged from 0.04-0.05 m^3/s, and the estimated pre-development peaks ranged from 0.015-0.02 m^3/s. For storm event with maximum rainfall depth more than 50 mm (Event 4), the post-development peak was estimated at 0.07 m^3/s and the pre-development peak, about 0.03 m^3/s.

Stormwater management target was to lower the post-development peak as much as possible. In general, all measures had introduced reduction of peak hydrographs. Referring to Figures 9a-c, Measure 2 had the least reduction, about 12% compared with post-development peaks. This was followed by Measure 1 with 16% and Measure 3 with 28%. The similar peak reduction patterns were repeated in Figure 9d, in which Measure 2 had lowered 13%, Measure 2 with 17% and Measure 3 with 30%.

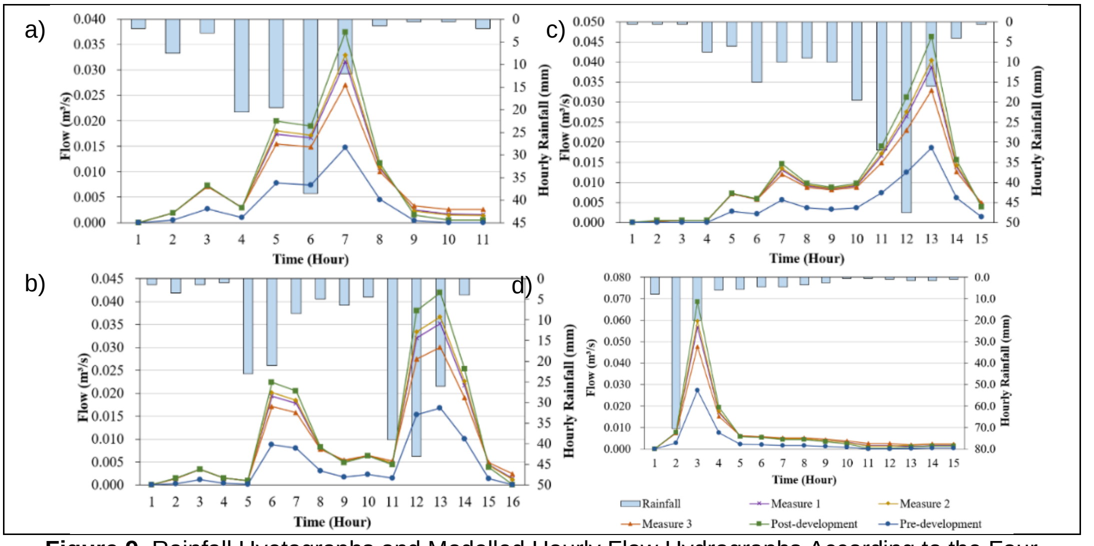

Figure 9. Rainfall Hyetographs and Modelled Hourly Flow Hydrographs According to the Four Measures Subjected to a) Event 1 (18 Jan 2015), b) Event 2 (19 Jan 2015), c) Event 3 (17&18 Dec 2017) and d) Event 4 (11&12 Dec 2019)

Storage Performance Analyses

Analysing the detention structures, on the other hand, the modelled water depths told a different turn. Presented in Figure 10, all detention structures showed water depths had reached the maximum level, 0.3 m in all cases of storm events.

Contrary to Figure 9 that was plotted with hourly historical rainfall, Figure 10 is presented with the accumulated rainfall curve from the historical rainfall data. In the same graphs, detention structures in the walkway under the veranda are presented in bar charts. The walkway structures were sub-divided into the corner lot and intermediate lot for having different shop lot width. The car parking spaces were sub-divided alike.

As such, the surface areas were defined as 9 m x 3 m for walkway – corner lot, 7 m x 3 m for walkway – intermediate lot, 9 m x 5m for parking space – corner lot and 7 m x 5 m for parking space – intermediate lot. The height of the storage structures maintained at 0.3 m throughout. The orifice outlets installed to the structures were also maintained at 0.05 m throughout.

Under the intensity of Event 1 (Figure 10a), all the structures reached its maximum level from hour 6-8, after the maximum rainfall depth was reached. However, under Event 2 (Figure 10b), the structures were full after hour 7 onwards before the maximum rainfall depth of the storm. Similarly, under Event 3, the structures were full after hour 10 onwards before the maximum rainfall depth of the storm.

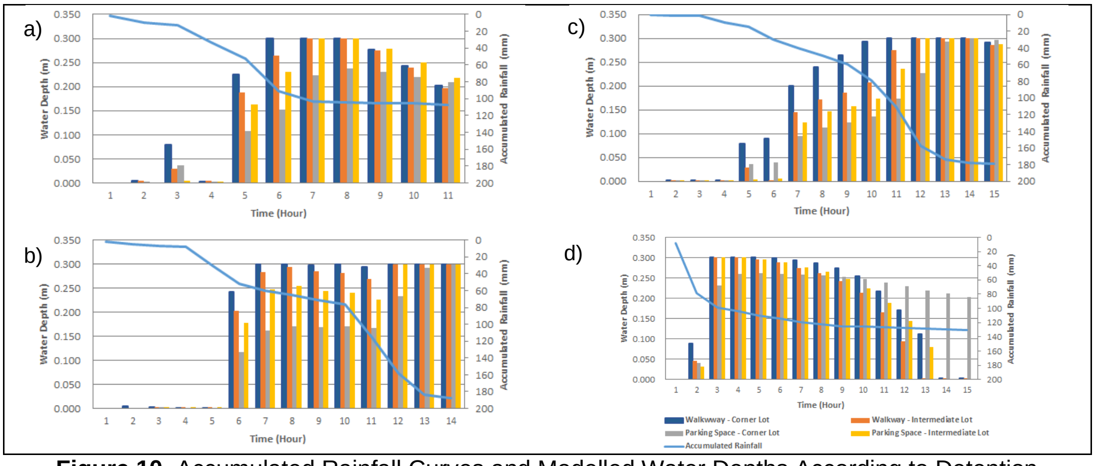

Figure 10. Accumulated Rainfall Curves and Modelled Water Depths According to Detention Structures Subjected to a) Event 1 (18 Jan 2015), b) Event 2 (19 Jan 2015), c) Event 3 (17&18 Dec 2017), and d) Event 4 (11&12 Dec 2019)

Under Event 4, the structures were full in between hour 3 to 6 after the maximum rainfall depth. The relationships of maximum rainfall depth and the maximum water depth in the storage were not clear. However, with the accumulated rainfall curves from the four events, it was found that the detention structures, regardless of it types, would be full when the accumulated rainfall was greater than 60 mm. The durations to reach the full tank varied greatly from case to case, namely Event 1 would take 5 hours, Event 2 about 7 hours, Event 3 about 9 hours and Event 4 about 2 hours.

DISCUSSION

In the first part of the analyses, it was found the catchment sizes that directed water to detention structures played a role in the reduction rates of post-development peak hydrographs. Take the example of Measure 3, the veranda and car parking detentions received water from 30% surface area of the total commercial centre. The reduction rates were estimated 28-30% compared with post-development peaks. The reduction was small considering that the rest of 70% surface area continued to discharge water to the urban drain. As such, it was suggested by Rosenberger, Leandro, Pauleit and Erlwin (2021) that a robust combination of measures was needed to restore the runoff characteristics of the commercial centre to pre-development condition.

In the second part of the analyses, the modelling results of storage performances were expected to overflow. As the selected historical data were flooding events, subjecting the detention structures to the flooding events would point to the extends that caused the flooding. It was found that the detention structures were able to sustain the accumulated rainfall lesser than 60 mm. However, this was preliminary in nature which limited to four historical extreme rainfall events and the types of detention structures specified in this study. It also hinted a plausible relationship existed between accumulated rainfall and detention storage capacity which the research team could only crudely describe at the moment.

Limitation of the current modelling efforts was the exclusion of overflow outlets in the detention structures. The overflow outlets were usually placed at the upper part of the structures, while the orifice outlets were placed at the bottom. SWMM could only model the orifice outlets but could not accommodate both outlets at the same simulation. The overflow outlets could have lengthened the time to reach full tank and shortened the time span of having full tank over the course of storm.

CONCLUSION

The veranda and car parking lot detention structures in this study was previously designed to 23 mm design rainfall. As such, the structures had water storing capacity limited by the 10-year ARI design rainfall. It was in line with the local guideline on minor stormwater system. However, using historical extreme rainfall events, as demonstrated, it was found the said detention structures could withstand up to 60 mm accumulated rainfall, but with a wide range of durations from 2 to 9 hours. It appeared that a relationship could be further explored on the accumulated rainfall and detention capacity.

ACKNOWLEDGEMENT

The authors acknowledged the financial support from the International Matching Grant Scheme between Universiti Malaysia Sarawak and Universitas Pembangunan Jaya under the research program entitled “Flood Infrastructure for Sustainable Urban Development”.

REFERENCES

Bateni, N., Lai, S. H., Putuhena, F. J., Mah, D. Y. S., Mannan, M. A., Chin, R. J. (2020) Hydrological Impact Assessment on Permeable Road Pavement with Subsurface Micro-Detention Pond. Water and Environment Journal, 34(S1): 960-969. Doi:10.1111/wej.12613.

Bilodeau, K., Pelletier, G., Duchesne, S. (2018) Real-Time Control of Stormwater Detention Basins as an Adaptation Measure in Mid-Size Cities. Urban Water Journal, 15(9): 858-867. Doi:10.1080/1573062X.2019.1574844.

Campisano, A., Modica, C., Gullotta, A. (2020) Long-Term Experiments for the Evaluation of the Potential for SDtorm Water Control of Modular Blue Roofs in Mediterranean Climate. Urban Water Journal, 18(1): 33-42. Doi: 10.1080/1573062X.2020.1850807.

Department of Irrigation and Drainage (DID) of Malaysia. (2012). Urban Stormwater Management Manual for Malaysia, 2nd Edition. Kuala Lumpur: Percetakan Nasional Malaysia.

Hamouz, V., Pons, V., Sivertsen, E., Raspati, G. S., Bertrand-Krajewski, J.-L., Muthanna, T. M. (2020) Detention-based Green Roofs for Stormwater Management under Extreme Precipitation due to Climate Change. Blue-Green Systems, 2(1): 250-266. Doi: 10.2166/bgs.2020.101.

Kaykhosravi, S., Khan, U. T., Jadidi, M. A. (2022) A Simplified Geospatial Model to Rank LID Solutions for Urban Runoff Management. Science of the Total Environment, 831: 154937. Doi:10.1016/j.scitotenv.2022.154937.

Mah, D. Y. S., Ayog, J. L., Salehe, A. H. M. (2022) Dual-System Concept for Stormwater Control in Commercial Centre. International Journal of Advanced Technology and Engineering Exploration, 9(86): 1-15. Doi:10.19101/IJATEE.2021.874685.

Mah, D. Y. S., Bateni, N., Bustami, R. A., Adam, J. H., Salehe, A. H. M. (2021) Accommodating Stormwater Storage Structure in the Veranda of Shop Building International Journal of Advanced Technology and Engineering Exploration, 8(82): 1208-1221. Doi:10.19101/IJATEE.2021.874433.

Maulana, S., Samad, M. H. A., Nordin, J. (2022) The Role of Extensive Green Roof to Reduce Flood Risk in Urban Scale Using Multi-Criteria Decision Analysis. Malaysian Construction Research Journal, 15(Special issue 1): 169-184.

Maurer, L., Zumsteg J., Lutz, C., Ottermatte, M. P., Wanko, A., Heintz, D., Villette, C. (2021) Towards a Model for Road Runoff Infiltration Management. npj Clean Water, 4: 44. Doi:10.1038/s41545-021-00136-z.

Ostendorf, M., Morgan, S., Celik, S., Retzlaff, W. (2021) Evaluating the Potential Stormwater Retention of a Living Retaining Wall System. Journal of Living Architecture, 8(1): 1-18. Doi: 10.46534/jliv.2021.08.01.001.

Pour, S. H., Wahab, A. K. A., Shahid. S., Asaduzzaman. M., Dewan. A. (2020) Low Impact Development Techniques to Mitigate the Impacts of Climate-Change-Induced Urban Floods: Current Trends, Issues and Challenges. Sustainable Cities and Society, 62: 102373. Doi: 10.1016/j.scs.2020.102373.

Public Utilities Board (PUB) of Singapore. (2010). Technical Guide for On-Site Detention Tank Systems. Singapore: National Water Agency.

Rainey, J. L., Brody, S. D., Galloway, G. E., Highfield, W. E. (2021) Assessment of the Growing Threat of Urban Flooding: A Case Study of a National Survey. Urban Water Journal, 18(5): 375-381. Doi:10.1080/1573062X.2021.1893356.

Rey-Mahía, C., Álvarez-Rabanal, F. P., Sañudo-Fontaneda, L. A., Hidalgo-Tostado, M., Menéndez Suárez-Inclán, A. (2022) An Experimental and Numerical Approach to Multifunctional Urban Surfaces through Blue Roofs. Sustainability, 14(3): 1815. Doi:10.3390/su14031815.

Rosenberger, L., Leandro, J., Pauleit, S., Erlwin, S. (2021) Sustainable Stormwater Management under the Impact of Climate Change and Urban Densification. Journal of Hydrology, 596: 126137. Doi:10.1016/j.jhydrol.2021.126137.

Shams, S., Ismail, P. H. R. I. B. P., Zania, A. B. H., Mohamad, A. B. H. (2018) Challenges and Opportunities of Green Roof in Building Design: A Case Study in Bandar Seri Begawan. Malaysian Construction Research Journal, 5(Special Issue 3): 113-123.

Xiong, L., Yan, L., Du, T., Yan, P., Li, L., Xu, W. (2019) Impacts of Climate Change on Urban Extreme Rainfall and Drainage Infrastructure Performance: A Case Study in Wuhan City, China. Irrigation and Drainage, 68(2): 152-164. Doi:10.1002/ird.2316.

Xu, H., Liu, L., Ding P. (2021) Building Climate Resilient City through Multiple Scale Cooperative Planning: Experiences from Copenhagen. IOP Conference Series: Materials Science and Engineering, 1203: 032063. Doi:10.1088/1757-899X/1203/3/032063.

Yang, W., Zhang, J., Krebs, P. (2022) Low Impact Development Practices Mitigate Urban Flooding and Non-Point Pollution under Climate Change. Journal of Cleaner Production, 347: 131320. Doi:10.1016/j.jclepro.2022.131320.

Zakizadeh, F., Moghaddam Nia, A., Salajegheh, A., Sañudo-Fontaneda, L. A., Alamdari, N. (2022) Efficient Urban Runoff Quantity and Quality Modelling Using SWMM Model and Field Data in an Urban Watershed of Tehran Metropolis. Sustainability, 14(3): 1086. Doi:10.3390/su14031086.

Zeng, Z., Yuan, X., Liang, J., Li, Y. (2021) Designing and Implementation an SWMM-based Web Service Framework to Provide Decision Support for Real-Time Urban Stormwater Management. Environmental Modelling and Software, 135: 104887. Doi:10.1016/j.envsft.2020.104887.

This page intentionally left blank

ARTIFICIAL NEURAL NETWORK (ANN) CRACK WIDTH PREDICTION MODEL FOR REINFORCED CONCRETE BEAM-COLUMN JOINT UNDER CYCLIC LATERAL LOADING

Reventheran Ganansan[1], Chee Ghuan Tan[2], Zainah Ibrahim[2], Mustapha Kamil Omran[1], Ramappa Ramesh Nayaka[3] and Ahmed El-Shafie[2]
[1]*Department of Transportation Engineering Technology, Faculty of Engineering Technology, Universiti Tun Hussein Onn Malaysia, Malaysia.*
[2]*Department of Civil Engineering, Faculty of Engineering, Universiti Malaya, Malaysia.*
[3]*Department of Civil Engineering, National Institute of Technology Warangal (NIT), India.*

Abstract
When it comes to individual structural RC elements, current ANNs models predict reasonable accuracy of crack width; however, not many studies have been found when it comes to the jointed part of the RC element subjected to lateral cyclic loadings. The ANN crack width prediction model based on Neural Net and Decision Tree was developed in this paper with a focus on the RC beam-column joint (BCJ) area, taking drift ratio, shear links, and length of the anchorage within the joint region into account. Based on the lowest errors, the best crack width model is chosen and further optimised using data splitting ratios.

Keywords: *Crack Widths; RC Beam-Column Joint; Machine Learning; Prediction Models; Data Splitting Ratios.*

INTRODUCTION

Since the uncontrollable nature of crack formation in reinforced concrete structures can seriously affect the structure's stability and strength, it has been the subject of numerous studies in recent years (Elshafey et al., 2013). Such cracks begin as narrow and elongated cracks with openings of less than 0.5 mm, which are frequently not visible with the naked eye (Souza, 2019). Although design codes impose crack width restrictions based on empirical formulas, uncertainty is frequently associated with determining crack width propagation due to cyclic / seismic loads (ACI., 2001 : Normalisation, 2004). Many computational methods and neural network models were used to assess crack propagation and crack duration. Artificial Neural Network (ANN) and Finite Element Modelling (FEM) have been widely used over the last decade to analyse and predict crack formation, crack propagation, and crack width, allowing the surface of reinforced concrete structures to be predicted with reasonable accuracy.

A review of existing research reveals that no methods for determining the crack widening mechanism are available, especially when reinforced concrete structures are subjected to seismic charging events such as earthquakes (Xu et al., 2017). In particular, studies have lacked the development of models for predicting crack width in RC beam-column joint (BCJ) members subjected to cyclic lateral loading. As a result, for engineering practise, a robust approach is required to develop a prediction model with insight into the crack width in RC BCJ structures. This paper used Rapidminer machine learning to analyse and predict the evolution of crack width using two types of prediction models. Inputs for the RC BCJ design parameters included the number of shear links, anchorage length, and lateral cyclic drift ratio loading. Based on the least error observed compared to experimental crack widths, the best crack width ANN model was chosen from the simulation results. Additional analysis and optimization were carried out using the data splitting process.

EXPERIMENTAL DESIGN

This study includes seven exterior RC BCJs of the same dimensions (column: 2000 mm x 200 mm 200 mm, beam: 1250 mm x 200 mm x 250 mm). Table 1 contains the specifics. Figure 1 depicts a schematic drawing of the specimen layout along with the test setup. The test specimens were considered partially fixed at both ends of the column. The tops of the columns were connected to a 500 kN horizontal hydraulic actuator, while the bottoms of the columns were braced on the surface of a strong floor. The ends of the beams were secured by a circular axial steel pin attached to the strong base of the floor.

Table 1. Designed Specimen Description

Specimen	Detailing					Remarks
	Column		Beam		At joint	
	Main Bar	Shear Link Spacing (mm)	Main Bar	Shear Link Spacing (mm)	Anchorage Length (mm)	
BCJ-1	4T12	-	4T12	-	250	Design based on British Standard (Allen, 2014)
BCJ-2	4T12	R8-75 (600*)	4T12	R8-75 (300*)	250	Strengthen at joint based on EC8 (Low to moderate seismic) (Fardis et al., 2015)
BCJ-3	4T12	R8-75 (850)	4T12	R8-75 (600*)	250	Designed as in BCJ-2 with 30% increased number of shear links
BCJ-4	4T12	R8-50 (600)	4T12	R8-50 (300*)	250	Designed as in BCJ-2 with minimum link spacing allowed in the seismic design
BCJ-5	4T12	R8-75	4T12	R8-75 (300*)	180	Designed as in BCJ-2 without anchorage length (U-bar)
BCJ-6	4T12	R8-75	4T12	R8-75 (300*)	500	Designed as in BCJ-2 with twice anchorage length
BCJ-7	4T12	R8-75	4T12	R8-75 (300*)	750	Designed as in BCJ-2 with thrice anchorage length

(*Shear span of additional shear links)

The increased anchorage length and additional shear link spacing (see Figure 1) in BCJ-2, BCJ-3, BCJ-4, BCJ-5, BCJ-6, and BCJ-7 specimens were arranged as "strong column / weak beam" for low to moderate seismicity based on ductility class medium (DCM) (Fardis et al., 2015 : Standards Malaysia, 2017). The displacement control mode was used to test these specimens with simulated earthquake loading under lateral cyclic loading (Roy & Laskar, 2018). Figure 2 depicts the cyclic load history in accordance with ACI 374.2R-13 (Rautenberg et al., 2013). The cycles were repeated three times at each drift ratio (Δy) level of 0.25%, 0.50%, 0.75%, 1.00%, 1.25%, 1.50%, and so on until the specimen failed. The drift ratio (Δ) was calculated as lx/H, where lx represents the lateral displacement and H is the column height (Truong et al., 2017).

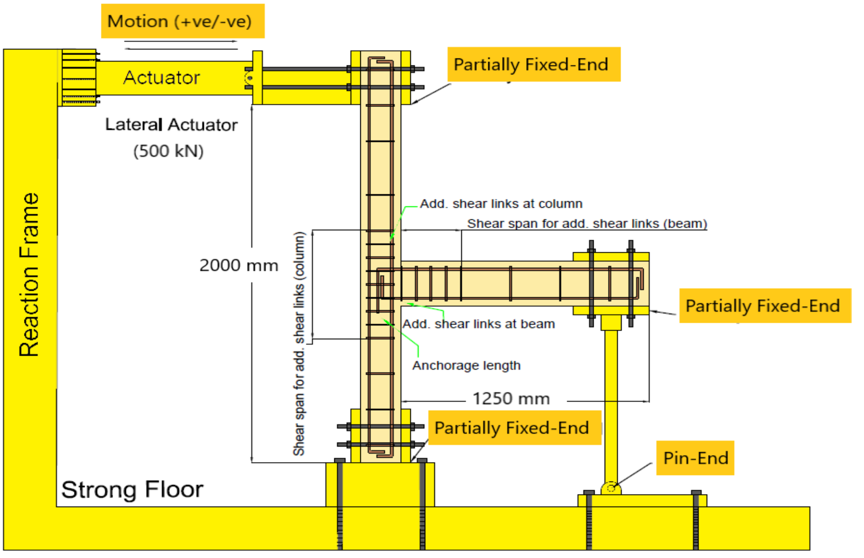

Figure 1. Typical Setup and Detailing of RC BCJ Specimen

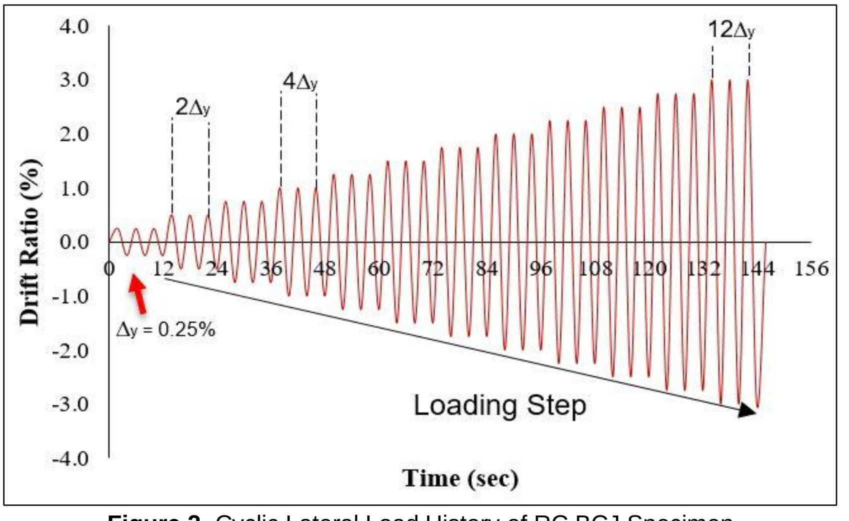

Figure 2. Cyclic Lateral Load History of RC BCJ Specimen

Table 2. List of Data Chosen for Modelling Purposes as Input Parameters

Num	Parameters Obtained Before and After Experimental Testing	Abbrev.	Unit
1.	Reinforcement area	A_s	mm^2
2.	Shear link spacing at beam	OL_B	mm
3.	Shear link spacing at column	OL_C	mm
4.	Shear span for additional shear links at beam	SSL_B	mm
5.	Shear span for additional shear links at column	SSL_C	mm
6.	Anchorage length at joint	AL	mm
7.	Concrete compression strength	C_c	MPa
8.	Drift ratio	DR	%
9.	Maximum positive load carrying capacity	$Q_{max(+ve)}$	kN
10.	Maximum negative load carrying capacity	$Q_{max(-ve)}$	kN

As shown in Table 2, many data were documented before and after experimental testing and were defined as potential input parameters for experimental crack width modelling. The data on crack widths is the most important output factor for prediction models. During testing, a dinolite microscope camera was used to measure and evaluate the crack width in each drift ratio (DR) point, as previously recommended in studies (Akter Hosen et al., 2016; Borg et al., 2018).

ANN FRAMEWORK MODEL CONFIGURATION

Creating an accurate structural quality prediction model can be difficult, especially when modelling crack width in the RC BCJ area subject to lateral cyclic loading with respect to different DR levels. In this project, two types of ANN prediction models were used: Neural Net (NN) and Decision Tree (DT) from Rapidminer software. NN is a feed-forward model in which no direct cycle is formed by connecting the units. In this network, information travels only one way from the input nodes to the output nodes: through the hidden nodes (if any) (Singh & Chauhan, 2009). As illustrated in Figure 3, the basic framework for NN requires three layers (Input, Hidden and Output) (Da Silva et al., 2017). The input layer is the first layer where data / features are obtained, and certain standardisation techniques are applied to these inputs to limit the inputs to a specific set. Standardized inputs improve the function of the neural network, resulting in higher precision. The hidden layer (intermediate or invisible) may be a collection of layers, depending on the network application. These layers are in charge of identifying a process or system's pattern. The NN's activities are mostly carried out in these layers. Additionally, neurons in the output layer are used to reflect the final network outputs generated by the previous layers of neuron processing. Feed-forward NN has sparked a lot of interest in material and civil engineering issues (Awodele & Jegede, 2009). As a basic but user-friendly approach, the model demonstrates a feasible approach used in weather forecasting, water management regulation, and concrete strength prediction (ranging in different number scales) (Khashei & Bijari, 2012; Kin et al., 2012; Sampaio et al., 2009).

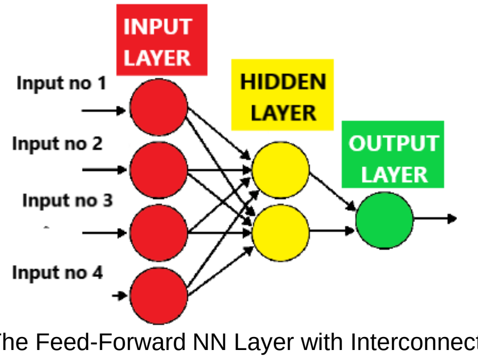

Figure 3. The Feed-Forward NN Layer with Interconnected Nodes

DT is a supervised method of learning that is used for classification and regression tasks. DT was derived from the term Classification and Regression Tree (CART), which was introduced in 1984 by Breiman and his colleagues (Breiman et al., 1984). DT is usually produced by creating algorithms that divide a dataset (instances) into branch-like segments. Such segments form an inverted decision tree that begins at the top of the tree with a root node (Mastorakis et al., 2015). Figure 4 shows that the DT model can have both continuous and discrete attributes (Deepnarain et al., 2019). Several DT applications in engineering practise have promoted numerical and categorical data with satisfactory results, demonstrating that the model can handle data at various scales, make it easy to understand, and facilitate the development of rules for predicting complex relationships. (Karbassi et al., 2014; Khosravi et al., 2018). However, because DT is not a stable model for small datasets, large amounts of data are required for this standard computing model to perform well. Furthermore, the DT model will build overly complex trees (overfitting) that are poorly generalised from the training data (Brandmaier et al., 2013; Deng et al., 2011; James et al., 2013).

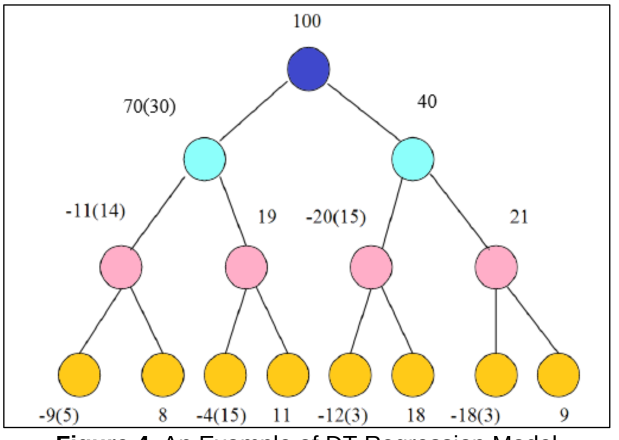

Figure 4. An Example of DT Regression Model

Rapidminer's system model was created as shown in Figure 5, which was similar for both prediction models. The labelling data set evaluated the classification regression output for all models, where input data was assigned label roles and experimental crack width data was assigned an attribute with a predictive function. The label attribute contains the actual observed values, whereas the prediction attribute contains the predicted label values from the regression models. The models are created by training with a collection of sample data known as a training set. Trained models were then given a test set to predict the accessible accuracy of crack width data. The simulation used 9 input vector numbers and a split data ratio of 75:25 (training: testing) for both prediction models. Section 4.1 describes the predicted models of crack widths in greater detail.

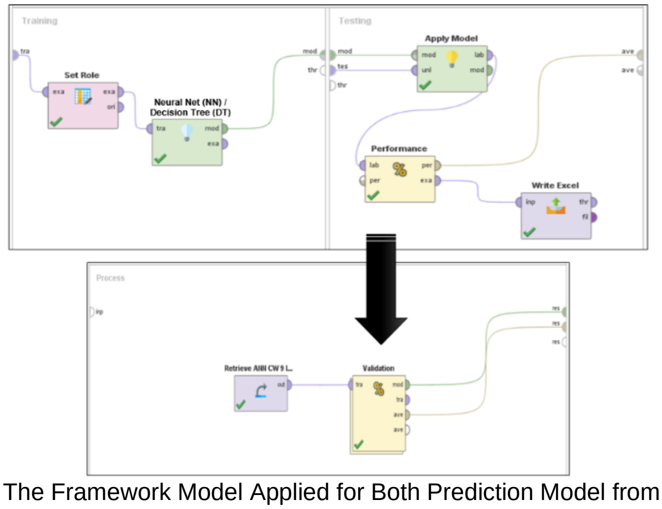

Figure 5. The Framework Model Applied for Both Prediction Model from Software

RESULTS AND DISCUSSION

Comparison of Prediction Models from Machine Learning

A total of 1000 experimental crack width datasets from all seven specimens were collected at each DR stage for training and testing in the Rapidminer programme. Table 3 shows two types of crack width prediction models. Figure 6 depicts the regression analysis plots for the distribution of predicted crack width in all prediction models.

Table 3. Detailed on Four Types of Prediction Models

Num	Model	Prediction Method
1.	Neural Net (NN)	**Shuffle:** This specifies that, before learning, input data should be shuffled. While it increases memory usage, if data is sorted before it is recommended.
2.	Decision Tree (DT)	**Least square:** For splitting, an attribute is chosen, which minimizes the square distance between the node averages in terms of the true value.

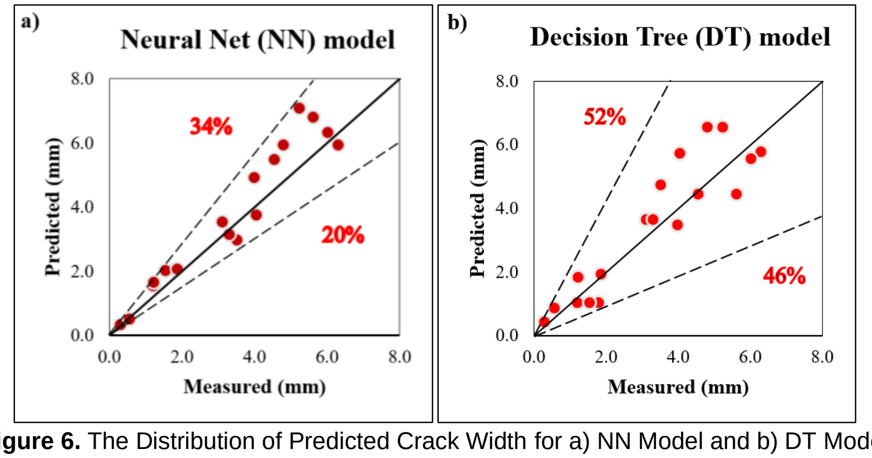

Figure 6. The Distribution of Predicted Crack Width for a) NN Model and b) DT Model

The figure includes an equity line as a reference, which represents the condition of equal values for the predicted and measured crack widths. The analysis shows that the NN model had a better prediction with the lowest error, with the predicted distribution being lower (20% error) and higher (34% error) than the DT model (46% and 52%). The DT model revealed that nearly all of the predicted points were clustered around the measured crack widths, resulting in over-fitting. Because the DT model was unreliable due to a lack of a large number of simulation datasets, as stated in the previous section, these high errors suggested that insufficient data was the main factor (James et al., 2013; Deng et al., 2011; Brandmaier et al., 2013). The NN model's accuracy of expected crack widths was consistently improved within the equity rows, demonstrating regression technique with input-output relations. This was supported further by the regression technique developed for concrete strength prediction (Kin et al., 2012) which demonstrated that the NN prediction is in reasonably good agreement with the measured data. As a result, NN demonstrated the best learning technique for this regression task, and it was chosen for further optimization analysis using data splitting, as described in the following subsection.

Data Splitting Ratio Analysis in NN Model

When an explicit testing set was not available, the split validation operator was used to predict the model's fit to a hypothetical testing set. Split validation also allows for training on one data set and testing on another explicit testing data set. The goal of categorising data in this prediction model was to avoid over- and under-fitting while only optimising the training dataset accuracy. As a result, there is a need for a model that performs well on datasets that it has never seen before (test data), which is referred to as generalisation. Figure 7 depicts three different results based on linear sampling for the prediction model's split ratio between training and testing of 70:30, 75:25, and 80:20.

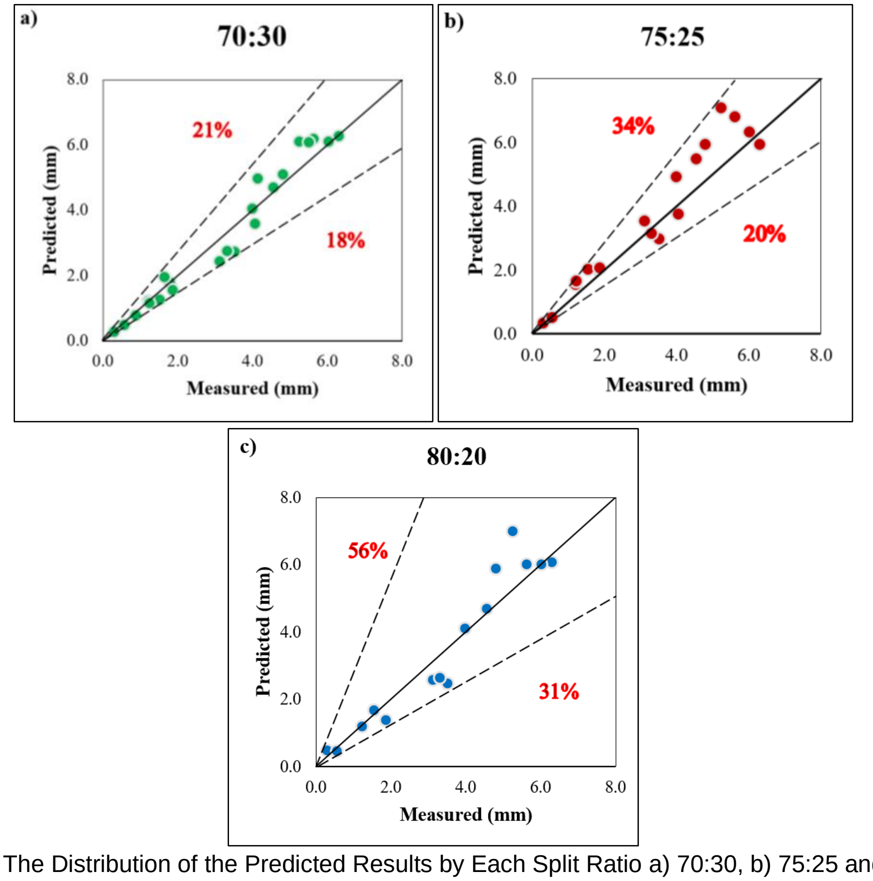

Figure 7. The Distribution of the Predicted Results by Each Split Ratio a) 70:30, b) 75:25 and c) 80:20

The split ratio of 70:30 near the reference line resulted in the lowest error of predicted crack widths (18% and 21%). It is thus a greater split ratio than the split ratios of 75:25 (20% and 34%) and 80:20 (31% and 56%). Due to unbalanced data from a smaller number of datasets, the majority of the predicted points for the 80:20 split ratio was far below the equity/measured line, resulting in a high predictive variance that can significantly change testing accuracy. In other words, significant over-fitting in the 80:20 split ratio may result in redundancy in experimental output data. According to previous research, the proportion chosen for fewer data set numbers (1000 data) in the analysis was 70% for the training set and 30% for the test set. Less test data means more variance efficiency for the model algorithm, while more training data means less variance in parameter estimates (Murthy &

Suresha, 2015; Torresani & Lee, 2007). As a result, for this data set, the 70:30 split falls within the experimental range and is a reasonable choice.

CONCLUSION

In this study, predictive models were developed to analyse and predict crack width in the area of reinforced concrete beam-column joints (RC BCJ) under cyclic lateral loading. Rapidminer machine learning software was used to create the prediction models, which took into account the numbers in the drift ratio (DR) level as well as the number of offset shear links and anchorage length within the joint zone. The results demonstrated that the neural net (NN) model outperformed other models in the crack width prediction process. In this analysis, the following conclusions are reached:

- The NN prediction model was chosen because it had a 34% lower discrepancy between measured and predicted crack width than the DT prediction model (52%).
- The 70:30 split testing and training smaller number dataset for NN prediction model data splitting ratio was comparable with the experimental range, making this study a decent and reasonable choice.

For future research, the current datasets will be implemented in various types of ANN prediction models (Rapidminer machine learning software), including several optimization approaches, with the goal of achieving the lowest error with a predicted value of 5-10%.

ACKNOWLEDMENT

This research was supported by Universiti Tun Hussein Onn Malaysia (UTHM) through Tier 1 (vot Q153) and Universiti Malaya through Impact – Oriented Interdisciplinary Research Grant Programme (IIRG): IIRG004B-2021IISS.

REFERENCES

ACI. (2001) ACI 224R-01: control of cracking in concrete structures. Farmington Hills (Michigan, USA): American Concrete Institute.

Akter Hosen, M., Jumaat, M. Z., Saiful Islam, A., Obaydullah, M., Darain, M., and Huda, N. (2016) Investigation on Energy Absorption Capacity of Reinforced Concrete Beams by the Near-Surface Mounted Technique Using Ductile Materials. Science of Advanced Materials, 8(8), 1536-1546.

Allen, A. (2014) Reinforced Concrete Design to BS 8110 Simply Explained: CRC Press.

Awodele, O., and Jegede, O. (2009) Neural networks and its application in engineering. Science & IT.

Borg, R. P., Cuenca, E., Gastaldo Brac, E. M., and Ferrara, L. (2018) Crack sealing capacity in chloride-rich environments of mortars containing different cement substitutes and crystalline admixtures. Journal of Sustainable Cement-Based Materials, 7(3), 141-159.

Brandmaier, A. M., von Oertzen, T., McArdle, J. J., and Lindenberger, U. (2013) Structural equation model trees. Psychological methods, 18(1), 71.

Breiman, L., Freidman, H., Olshen, A., and Stone, C. (1984) Classification and regression trees. Monterey CA: Wadsworth & Brooks/Cole Advanced Books & Software.

Da Silva, I. N., Spatti, D. H., Flauzino, R. A., Liboni, L. H. B., and dos Reis Alves, S. F. (2017) Artificial neural networks. Cham: Springer International Publishing.

Deepnarain, N., Nasr, M., Kumari, S., Stenström, T. A., Reddy, P., Pillay, K., and Bux, F. (2019) Decision tree for identification and prediction of filamentous bulking at full-scale activated sludge wastewater treatment plant. Process Safety and Environmental Protection, 126, 25-34.

Deng, H., Runger, G., and Tuv, E. (2011) Bias of importance measures for multi-valued attributes and solutions. Paper presented at the International Conference on Artificial Neural Networks.

Elshafey, A. A., Dawood, N., Marzouk, H., and Haddara, M. (2013) Crack width in concrete using artificial neural networks. Engineering Structures, 52, 676-686. doi: https://doi.org/10.1016/j.engstruct.2013.03.020.

Fardis, M. N., Carvalho, E. C., Fajfar, P., and Pecker, A. (2015) Seismic design of concrete buildings to Eurocode 8. CRC Press, Boca Raton, U.S.

James, G., Witten, D., Hastie, T., and Tibshirani, R. (2013) An introduction to statistical learning (Vol. 112): Springer.

Karbassi, A., Mohebi, B., Rezaee, S., and Lestuzzi, P. (2014) Damage prediction for regular reinforced concrete buildings using the decision tree algorithm. Computers & Structures, 130, 46-56.

Khashei, M., and Bijari, M. (2012) Hybridization of the probabilistic neural networks with feed-forward neural networks for forecasting. Engineering Applications of Artificial Intelligence, 25(6), 1277-1288.

Khosravi, K., Pham, B. T., Chapi, K., Shirzadi, A., Shahabi, H., Revhaug, I., Prakash, I., and Bui, D. T. (2018) A comparative assessment of decision trees algorithms for flash flood susceptibility modeling at Haraz watershed, northern Iran. Science of the Total Environment, 627, 744-755.

Kin, C. C., Don, M. M., and Ahmad, Z. 2012. Compressive strength prediction of concrete recycled aggregates made from ceramic tiles using feedforward artificial neural network (FANN) Computer Aided Chemical Engineering (Vol. 31, pp. 320-324): Elsevier.

Mastorakis, N., Bulucea, A., and Tsekouras, G. (2015) Computational Problems in Science and Engineering (Vol. 343): Springer.

Murthy, A. K., and Suresha. (2015) XML URL Classification Based on their Semantic Structure Orientation for Web Mining Applications. Procedia Computer Science, 46, 143-150. doi: https://doi.org/10.1016/j.procs.2015.02.005.

Normalisation, C. E. d. (2004) Eurocode 2: design of concrete structures: Part 1-1: General rules and rules for buildings. London (UK): British Standards Institution.

Rautenberg, J. M., Pujol, S., Tavallali, H., and Lepage, A. (2013) Drift capacity of concrete columns reinforced with high-strength steel. ACI Structural Journal, 110(2), 307.

Roy, B., and Laskar, A. I. (2018) Cyclic Performance of Beam-Column Subassemblies with Construction Joint in Column Retrofitted with GFRP. Structures, 14, 290-300. doi: https://doi.org/10.1016/j.istruc.2018.04.002.

Sampaio, T. P., Ferreira Filho, V. J. M., and Neto, A. D. S. (2009) An application of feed forward neural network as nonlinear proxies for use during the history matching phase. Paper presented at the Latin American and Caribbean Petroleum Engineering Conference.

Singh, Y., and Chauhan, A. S. (2009) Neural Networks in Data Mining. Journal of Theoretical & Applied Information Technology, 5(1).

Souza, J. C. (2019). "What Do The Cracks in Concrete Structures Mean?" [O que as rachaduras nas estruturas de concreto querem dizer?] from <https://www.archdaily.com/879953/what-do-the-cracks-in-concrete-structures-mean/>.

Standards Malaysia. (2017) Malaysia National Annex to Eurocode 8: Design of structures for earthquake resistance -Part 1: General rules, seismic actions and rules for buildings. Malaysia: SIRIM Berhad.

Torresani, L., and Lee, K.-c. (2007) Large margin component analysis. Paper presented at the Advances in neural information processing systems.

Truong, G. T., Dinh, N. H., Kim, J.-C., and Choi, K.-K. (2017) Seismic Performance of Exterior RC Beam–Column Joints Retrofitted using Various Retrofit Solutions. International Journal of Concrete Structures and Materials, 11(3), 415-433. doi: 10.1007/s40069-017-0203-x.

Xu, L. Y., Nie, X., Zhou, M., and Tao, M. X. (2017) Whole-process crack width prediction of reinforced concrete structures considering bonding deterioration. Engineering Structures, 142, 240-254. doi: https://doi.org/10.1016/j.engstruct.2017.03.060.

CHARACTERISTICS OF SIX-STRUT TENSEGRITY MODEL DURING SHAPE CHANGE

Nik Elisa Lidya Nik Badrul[1], Oh Chai Lian[1*], Mohd Raizamzamani Md Zain[1], Norrul Azmi Yahya[1], Lee Siong Wee[2] and Toku Nishimura[3]
[1]School of Civil Engineering, College of Engineering, Universiti Teknologi Mara (UiTM) Shah Alam, Shah Alam, Selangor, Malaysia.
[2]School of Civil Engineering, College of Engineering, Universiti Teknologi MARA Johor, Pasir Gudang Campus, UiTM, Masai, Johor, Malaysia.
[3]Department of Architectural Engineering, Institute of Disaster and Environmental Science, Kanazawa Institute of Technology, Ishikawa, Japan.

Abstract
Active and deployable tensegrity structures are extensively studied due to the unique characteristics of tensegrity such as highly deformable and controllable. This paper presents the numerical application of the shape change strategy on a six-strut model. The shape change method solves the optimisation problem for forced elongation in cables and minimises distance between the targeted coordinates and monitored nodes. A total of four numerical cases for a six-strut tensegrity model were studied, with one or two nodes monitored to approach the targeted coordinates prescribed in either x-, y- or z- directions. This paper aims to evaluate the effectiveness of the shape change method and determine the structural characteristics of a six-strut model during the shape change analysis. It is found that the six-strut model in all cases has successfully displaced and advanced to the prescribed targets via the shape change method. The numerical analysis results also show that the six-strut model performed axial and twisting deformations with the axial forces maintained within the elastic limit.

Keywords: *Tensegrity; Shape change; Six-strut; Optimisation.*

INTRODUCTION

Since the 1990s, there has been a rising focus on studying the deformation and deployment of tensegrity structures. Due to its unique structural characteristics like higher deformation capacity, good shock resistance ability, high strength-to-weight ratio, and foldability (Caluwaerts & Carbajal, 2015; Cimmino et al., 2017), tensegrity is suitable for shape change and deployment. Shape change of a tensegrity structure can be performed by altering the lengths of elements in the structure. One of the shape change strategies is to employ active cables with changeable length while the struts remain passive with no forced elongation (Van de Wijdeven & De Jager, 2005). Moreover, tensegrities are capable of undergoing large displacements despite their lightweight characteristic. Through the distribution and balancing of its mechanical stresses, tensegrity structures are self-stressed and stable (Tur & Juan, 2009). Tensegrities can convert a small local pressure into a large global deformation while continuously searching for a new balanced topology arrangement (Oh et al., 2020).

Shape change studies of tensegrity began in the 1990s. Past researchers incorporated various strategies to achieve a shape change of their tensegrities. Shape change strategies differ over different tensegrity models since there are no universal rules on the study of tensegrity (Rhode-Barbarigos et al., 2012). For instance, different methods were employed, such as the optimisation method (Caluwaerts & Carbajal, 2015) and force analytic method (Du et al., 2016) for the shape change study of the six-strut tensegrity model.

This paper presents the shape change analysis of a six-strut tensegrity model to achieve the targets via the computational method presented in author's previous works (Oh et al., 2022; Oh et al., 2019). The predetermined target positions in terms of nodal coordinates of either one or a set of two monitored nodes of the tensegrity model is described in this study. This paper aims to investigate the effectiveness of the shape change method through numerical application to a six-strut tensegrity model. The structural behaviours such as the deformed shape and the axial member forces throughout the shape change analysis are discussed.

LITERATURE REVIEW

An American architect named Richard Buckminster Fuller had developed a variety of inventions, mainly focusing on architectural designs. The term tensegrity which combines the word 'tension' and 'integrity' was first coined by Fuller. Tensegrity is a stable system in a constant self-equilibrated state consisting of islands of compression members in an ocean of continuous tension members (Rhode-Barbarigos et al., 2012). Figure 1 shows a class one three-strut tensegrity where continuous cables surround the struts. Tensegrity systems consist of compression elements (i.e., struts or bars) and tension elements (i.e., cables or strings) that exist in their pre-stressed form. In this structure, compression elements are not connected to each other at a node.

Since tensegrities can be folded or unfolded, the members and elements in tensegrity systems can be altered to its varying length. The pre-stressed interaction in the elements in the system preserves stability, thus adopting another steady configuration in tensegrity. Due to its characteristics, tensegrity is recommended as a good system for shape change study (Oh et al., 2019). Past researchers have studied tensegrity for space applications (Fazli & Abedian, 2011), deployable footbridges (Rhode-Barbarigos et al., 2012; Veuve et al., 2016), composite solar façades and wind generators (Cimmino et al., 2017). A study of tensegrity robots found that elastic cables provide excellent deformation capability (Du et al., 2016). Thus, the shape change of tensegrity considering the alterable length of cables is investigated in this study.

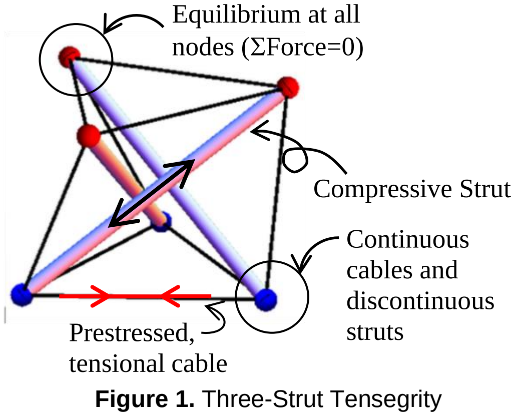

Figure 1. Three-Strut Tensegrity

Shape change methods combine measurements and control-command to produce the desired shape. Applying shape change methods like cable elongation to a deployable structure offers a unique prospect to study the shape change potentials of a multi-modular system (Oh et al., 2022). The concept of shape-changing tensegrity has also been proposed, especially in the design of deployable structures and robots. Shape-changing structures are promising replacements for present structures applied in the construction, robotics, space engineering and medical industries (Van de Wijdeven & De Jager, 2005). Although many studies on the shape change of tensegrity, there is still limited application due to the complication in computation and the characteristics of the structure. In this study, the proposed shape change strategy by author's previous work is employed to study the characteristics of a six-struts tensegrity model.

METHODOLOGY

Topology

The effectiveness of shape change strategy is evaluated through a numerical application to a six-strut tensegrity model presented in (Xu & Luo, 2011). It is to note that a pre-stressed characteristic is required to achieve a stable form before the application of any external loadings. The self-equilibrated six-strut tensegrity model at initial state is shown in Figure 2. The model is pin-jointed at the connection between members and consists of six struts and twenty-four cables. While there is no strut-to-strut connection, the struts are assumed rigid, and no elongation of struts were allowed. The nodal coordinate and element connectivity of the model is shown in Table 1.

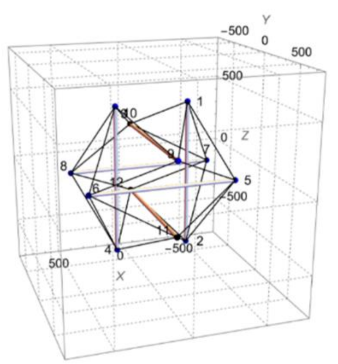

Figure 2. Self-Equilibrated Six-Strut Tensegrity Model

Shape Change Strategy

The shape change strategy proposed by the author's previous work involves four states: initial state, deformed state, shape change state and target state as shown in Figure 2 (Oh et al., 2022; Oh et al., 2019). This study employed a strategy to study the shape change of a six-strut tensegrity model. The initial topology of the six-strut tensegrity model was obtained from (Xu & Luo, 2011). The methodology of this study involves two parts: (1) determination of self-equilibrium state of the six-strut tensegrity model and (2) optimisation of forced elongation of cable for shape change analysis of the tensegrity model. The struts in the tensegrity model only show elastic elongation whereas the cables show both the forced and elastic elongation during the shape change analysis.

Table 1. Nodal Coordinate and Element Connectivity of The Six-Strut Tensegrity Model

Nodal Coordinate				**Element Connectivity**							
Node	*x*	*y*	*z*	Member	*i*	*j*	*T*	Member	*i*	*j*	*T*
1	-250	0	500	1	1	5	Cable	16	4	12	Cable
2	-250	0	-500	2	1	7	Cable	17	5	9	Cable
3	250	0	500	3	1	9	Cable	18	5	11	Cable
4	250	0	-500	4	1	10	Cable	19	6	9	Cable
5	-500	250	0	5	2	5	Cable	20	6	11	Cable
6	500	250	0	6	2	7	Cable	21	7	10	Cable
7	-500	-250	0	7	2	11	Cable	22	7	12	Cable
8	500	-250	0	8	2	12	Cable	23	8	10	Cable
9	0	500	250	9	3	6	Cable	24	8	12	Cable
10	0	-500	250	10	3	8	Cable	25	1	2	Strut
11	0	500	-250	11	3	9	Cable	26	3	4	Strut
12	0	-500	-250	12	3	10	Cable	27	5	6	Strut
				13	4	6	Cable	28	7	8	Strut
				14	4	8	Cable	29	9	10	Strut
				15	4	11	Cable	30	11	12	Strut

Note: *x, y, z* are coordinates and *i*, *y*, T are near end, far end and types of elements, respectively.

Figure 3 illustrates the shape change strategy involving four main states. At the initial state (t=0), the static equilibrium in forces of the six-strut tensegrity is obtained. The six-strut tensegrity model is in self-equilibrium and stands freely without constraints or pressure. At the initial state, while preparing the nodal coordinates and element connectivity, no boundary conditions or external loadings were applied to the tensegrity model. Axial forces of the model demonstrate the pre-stressed condition of the tensegrity, and there is no deformation at this state. At step t=1, when the monitored node and target coordinates have been assigned accordingly, the structure is in its deformed state and endures linear elastic deformation under self-weight loading and pin-supported at the base. The model performs its shape change state with their forced elongation in active cables. The monitored nodes eventually reached their specified target coordinates in their final state after the iterative step reaches N. It is to note that, N is the absolute number of incremental iterations to achieve a target state of the six-strut tensegrity and it is the end of a shape change analysis.

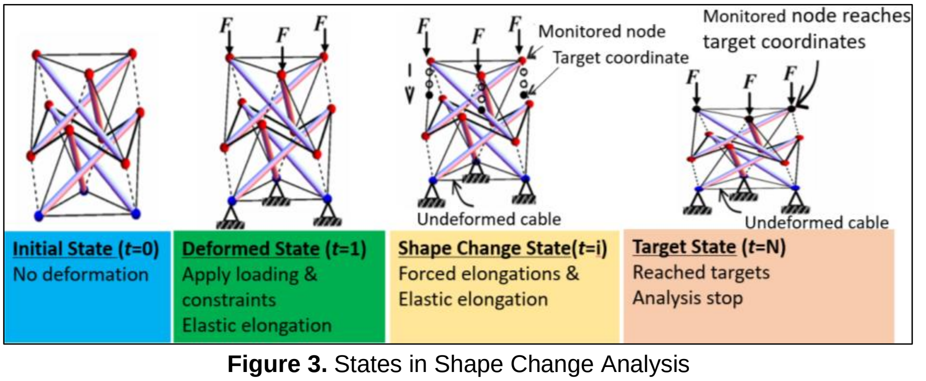

Figure 3. States in Shape Change Analysis

Figure 4 shows the shape change analysis algorithm that incorporate the four main states in the shape change analysis. The shape change method involves Sequential Quadratic Programming (SQP) to solve the nonlinear optimisation problem as shown in Equation 1.

$$\min_{x\in R^n} f(\boldsymbol{x}) = \boldsymbol{g}^T\,{}^t\boldsymbol{l} + \frac{1}{2}\,{}^t\boldsymbol{l}^T \boldsymbol{H}\,{}^t\boldsymbol{l}$$
$$\text{subject to } \boldsymbol{A}_2\,{}^t\boldsymbol{l} \geq \boldsymbol{b}_2 \tag{1}$$

where ${}^t\boldsymbol{l}$ is a $m_{cf} \times 1$ vector of incremental forced elongation which corresponds to the optimisation variable, $\boldsymbol{H}$ is a positive-definite approximation of Hessian matrix of the Lagrangian function. m_{cf} is the number of cables excluding the undeformed cables. Matrix $\boldsymbol{A}_2$ and vector $\boldsymbol{b}_2$ are the inequality constraints corresponding to the limitation in allowable axial forces and forced elongation.

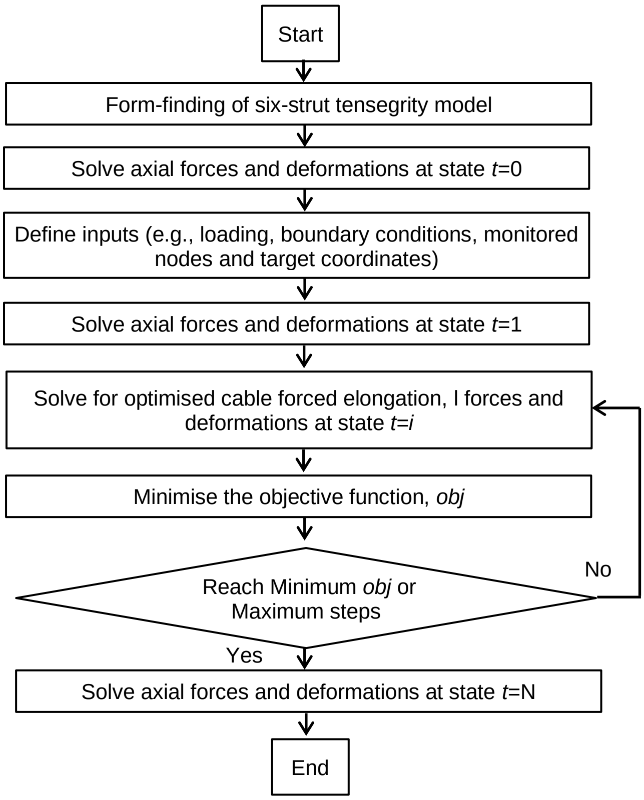

Figure 4. Shape Change Analysis Algorithm

For elastic material properties, the lower and upper axial force limit for cables and struts are defined as in Equation 2.

$$0 \leq n_c \leq \sigma_c A_c$$
$$\max\left\{-\frac{\pi^2 E_s I_s}{l_s^2}, -\sigma_s A_s\right\} \leq n_s \leq \sigma_s A_s \tag{2}$$

Where n_c, σ_c and A_c are axial forces, yield stress and cross-sectional area for cable elements, respectively; n_s, E_s, I_s, L_s, σ_s and A_s are axial forces, Young modulus, moment of inertia, element current length, yield stress and cross-sectional area for strut elements, respectively. In this study, all strut elements have circular cross-section.

RESULTS AND DISCUSSION

The shape change strategy has been proven in 4 different cases where the target coordinate for the randomly selected monitored nodes was prescribed in either x, y, or z-coordinate system under uni-direction mode. Different monitored nodes and target coordinates have been assigned to each case to represent the various shape changes of the six-strut tensegrity model. The six-strut tensegrity model is fixed at node 2 (N2) and node 4 (N4); hence, movement of N2 and N4 are not permitted. In addition to elastic elongation, the cables undergo force elongation, which also means changes of length, either shortening or lengthening, in the cables of the six-strut tensegrity are optimised to achieve the target coordinates for all four cases.

Table 2 shows the monitored nodes and target coordinates for the analysis cases, i.e., Case 1 to Case 4. For Cases 1-3, only one node was randomly selected as the monitored node. The chosen node was monitored during the shape change analysis to approach the target coordinates prescribed in *x*-, *y*-, or *z*- coordinates. For instance, Node 8 was monitored to reach the target which set at a *z*-coordinate of -100 in Case 1. This also means that the *z*-coordinate of Node 8 at the target state must be at a magnitude of -100, whereas the *x*-, and *y*- coordinates can be in any magnitudes. While for Case 4, two nodes were chosen to be monitored to approach in y directions.

Table 2. Monitored Nodes and Target Coordinates for All Four Cases

Case	Monitored Nodes	Target Coordinates		
		x	*y*	*z*
Case 1	N8	-	-	-100
Case 2	N1	-100	-	-
Case 3	N5	-	-100	-
Case 4	N5	-	-100	-
	N8	-	100	-

Convergence Curve

The monitored node in each case successfully reaches its target coordinates after some iterations, as shown in Table 3. Figure 5 shows the normalised objective function (NOF) graph against computational steps for Cases 1, 2, 3 and 4. All the cases illustrate almost linear trend of the NOF curves. An insignificant change of slope along the NOF curve Case 3 and Case 4 was also observed. The objective function was set based on the minimisation of distance between the nodal coordinate at the current step and the targeted coordinates. The slight change of slope in NOF curve may be due to the compliance of the constraints bound within the limits of the axial force in the struts or cables during the iterative shape change analysis in the minimisation of the objective function. Out of all the cases, Case 4 has recorded the highest number of iterations of 69 steps. Since there are two monitored nodes assigned having two different target coordinates to be achieved, it is reasonable to take more iterations in Case 4 to achieve the objective functions. Although all cases have different monitored nodes and target coordinates, the objective function was successfully achieved at their own respective pace. Overall, it can be concluded that this shape change program is effective for a six-strut model to reach the prescribed targets despite assigning different monitored nodes and target coordinates in either *x*-, *y*-, or *z*- axis.

Table 3. Total Computational Steps

Case 1	Case 2	Case 3	Case 4
22	24	61	69

Axial Forces

Figure 6 shows the axial forces of the six-strut tensegrity model at each iterative step for Case 1, Case 2, Case 3, and Case 4. There are 30 members in the model, particularly members 1 to 24 are cables while members 25 to 30 are struts. The six-strut tensegrity model has one self-equilibrated mode. The axial forces at initial state were obtained, indicating the six-strut tensegrity model is pre-stressed, satisfying the equilibrium in forces at all nodes. The changes in axial forces were first observed in deformed state when the model is under their self-weight loading. Fluctuation in the axial forces in all members was observed throughout the iteration steps in the shape change state. Despite changes in axial forces, the cables always in tension force and struts in compressive force validate the shape change method. The method ensures the satisfaction of the axial force constraint in solving the minimisation problem. It is to note that all the forces are within the lower and upper limits of the tension and compression forces.

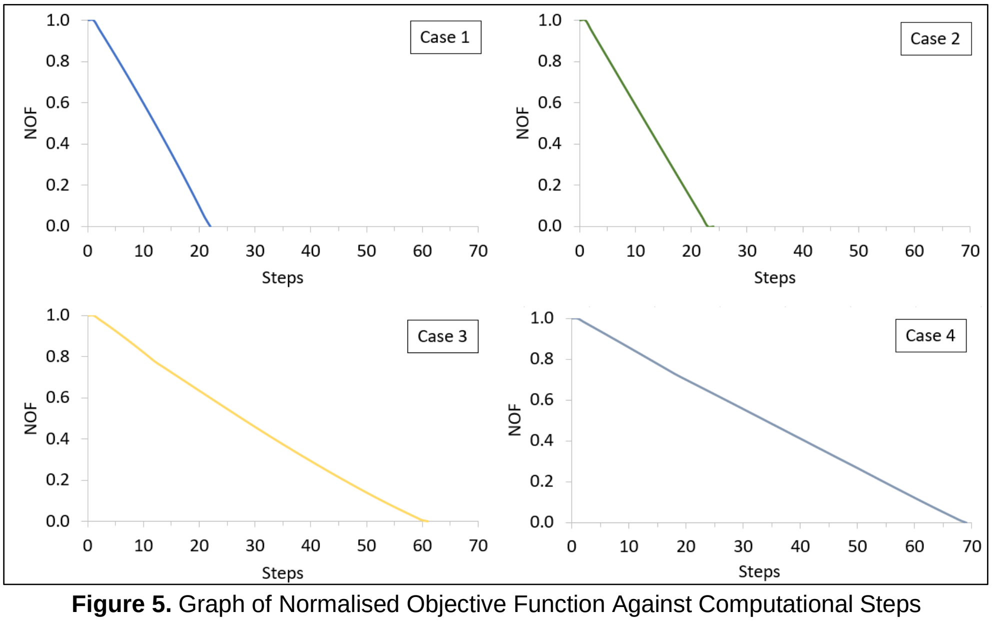

Figure 5. Graph of Normalised Objective Function Against Computational Steps

The changes of axial forces either in obvious or gradual fluctuations, are closely related to the deformation of the model in advancing towards the target. All the members have their axial forces changed in the same way in Cases 1 and 2. In Cases 3 and 4 on the other hand, different groups of members present same trend of changes in axial force, with a few members present unique trend (e.g., member 30 in Case 3, members 29 and 30 in Case 4).

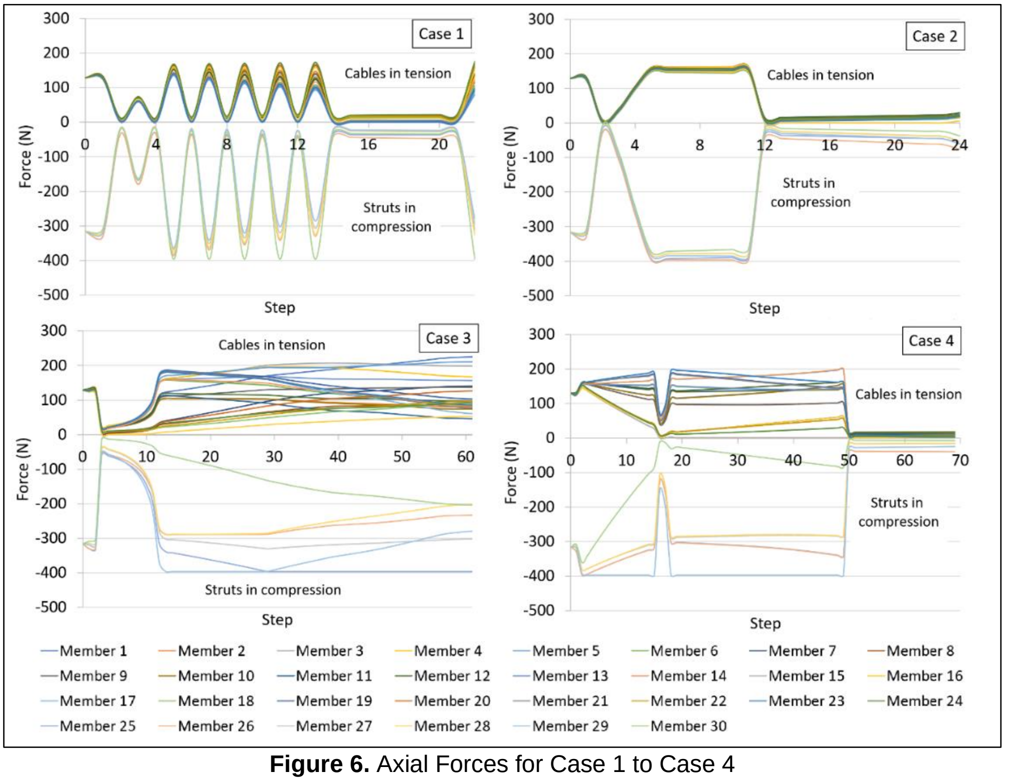

Figure 6. Axial Forces for Case 1 to Case 4

Deformed Shape

Figure 7 represents the shape change of the six-strut tensegrity model for Cases 1, 2, 3, and 4. Six-strut tensegrity model at the initial state (at step 1), shape change state (at half of the computational steps) and at target state (at maximum iteration) are presented for each case. To emphasise, all the defined monitored nodes in all cases reaches the target coordinates at the target state. For example, Figure 7(a) shows the displacement of node 8 towards the target throughout the shape change analysis. As seen in the figure, the target coordinate for each case is plotted in a red dot. The model in Case 1 during the iteration shows that the cables connected to the monitored node have been stretched and the entire six-strut tensegrity has slanted while leaning towards the direction of the target. The model in Case 2 on the other hand, records significant forced elongation in cables connected to Node 1. The strut connecting Node 1 and Node 2 is displaced in an inclined way towards the target in *x*-direction. In observing the shape change of the model in Case 3, it can be found that the six-strut tensegrity model undergoes a twist of about 30 degrees towards the target.

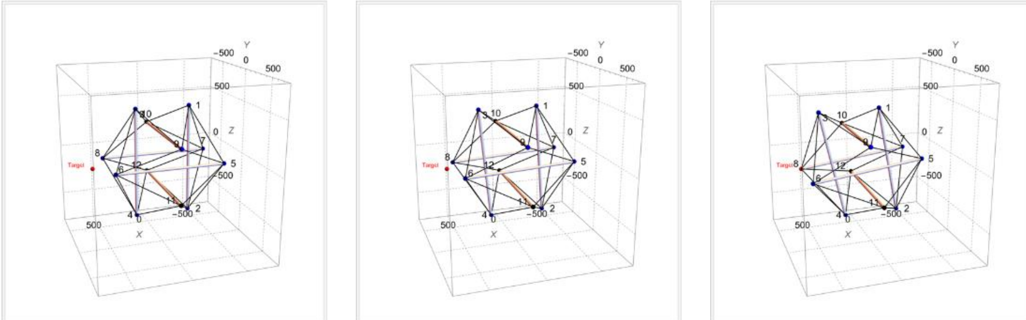

(i) Step 1 (ii) Step 2 (iii) Step 3

(a) Case 1

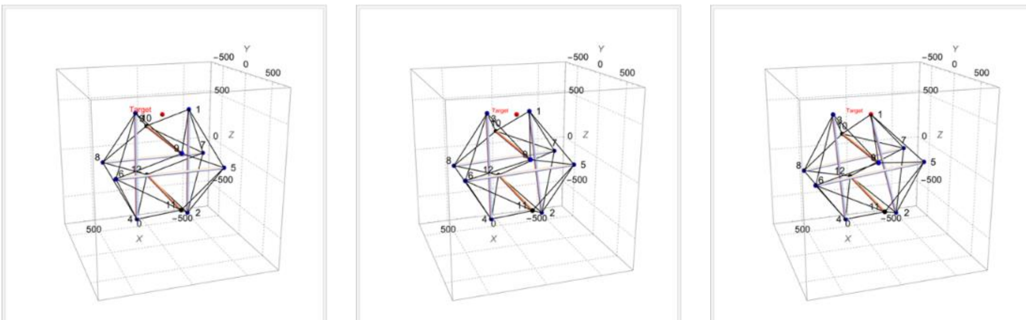

(i) Step 1 (ii) Step 2 (iii) Step 3

(b) Case 2

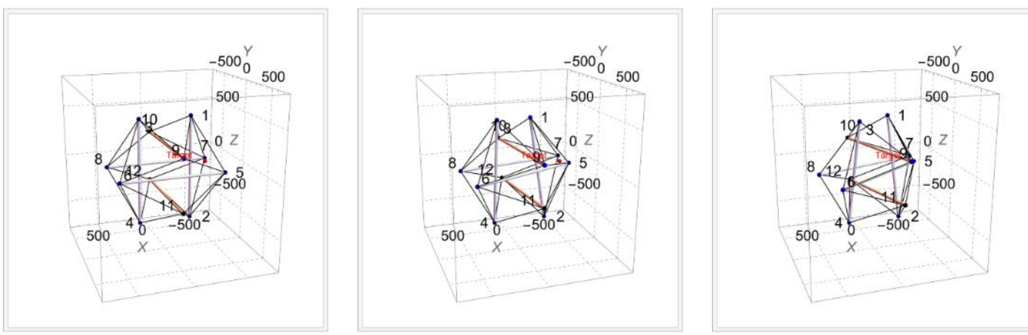

(i) Step 1 (ii) Step 2 (iii) Step 3

(c) Case 3

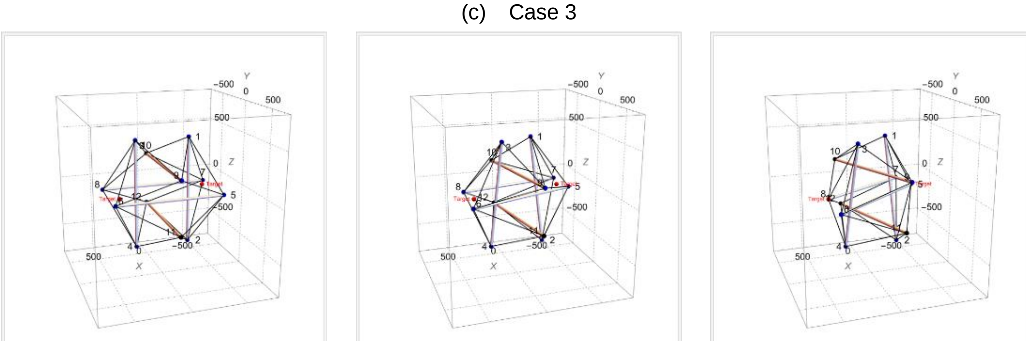

(i) Step 1 (ii) Step 2 (iii) Step 3

(d) Case 4

Figure 7. Deformation of Six-Strut Tensegrity

Before a twist, the cables surrounding Node 5 elongated while the struts displaced inwards and towards the target. The shape change of six-strut tensegrity in Case 4 is similar to the shape change in Case 3, which also undergoes a twisting. However, the model in Case 4 shows a movement on both the left and right-hand side of the model. It is found that six-strut model performed axial and twisting deformations during the shape change analysis.

CONCLUSIONS

The paper presents shape change analysis on a six-strut model in four different cases. The target coordinates were prescribed in either x-, y- or z- directions for one or two randomly selected monitored nodes. The numerical analysis shows in all the cases, the monitor node of the six-strut model successfully reaches the target by using the shape change method. A few conclusions can be made from the paper as follows:

1) The shape change method effectively solves the minimization problems where the monitored nodes reach the prescribed target coordinate in all the analysis cases.
2) The convergence curves in all numerical cases are linear, indicating effective and fast solutions to the minimization of objective function in the shape change method.
3) The axial member forces for cables and struts fluctuate over the shape change analysis but stay within the limits of the elastic range.
4) The six-strut model deforms in axial and twisting modes to advance to the target nodes during the shape change.

ACKNOWLEDGEMENTS

This research was funded by Ministry of Higher Education Malaysia, FRGS grant (FRGS/1/2021/TK0/UITM/02/11). In addition, the authors would also like to thank the School of Civil Engineering, College of Engineering, Universiti Teknologi MARA, Shah Alam, Selangor.

REFERENCES

Caluwaerts, K., & Carbajal, J. P. (2015). Energy conserving constant shape optimization of tensegrity structures. International Journal of Solids and Structures, *58*, 117-127.

Cimmino, M., Miranda, R., Sicignano, E., Ferreira, A., Skelton, R., & Fraternali, F. (2017). Composite solar façades and wind generators with tensegrity architecture. Composites Part B: Engineering, *115*, 275-281.

Du, W., Ma, S., Li, B., Wang, M., & Hirai, S. (2016). Force analytic method for rolling gaits of tensegrity robots. IEEE/ASME Transactions on Mechatronics, *21*(5), 2249-2259.

Fazli, N., & Abedian, A. (2011). Design of tensegrity structures for supporting deployable mesh antennas. Scientia iranica, *18*(5), 1078-1087.

Oh, C. L., Choong, K. K., Nishimura, T., & Kim, J.-Y. (2020). Form-finding of spine inspired biotensegrity model. Applied Sciences, *10*(18), 6344.

Oh, C. L., Choong, K. K., Nishimura, T., & Kim, J.-Y. (2022). Multi-Directional Shape Change Analysis of Biotensegrity Model Mimicking Human Spine Curvature. Applied Sciences, *12*(5), 2377.

Oh, C. L., Choong, K. K., Nishimura, T., Kim, J.-Y., & Hassanshahi, O. (2019). Shape change analysis of tensegrity models. Latin American Journal of Solids and Structures, *16*.

Rhode-Barbarigos, L., Ali, N. B. H., Motro, R., & Smith, I. F. (2012). Design aspects of a deployable tensegrity-hollow-rope footbridge. International Journal of Space Structures, *27*(2-3), 81-95.

Tur, J. M. M., & Juan, S. H. (2009). Tensegrity frameworks: Dynamic analysis review and open problems. Mechanism and Machine Theory, *44*(1), 1-18.

Van de Wijdeven, J., & De Jager, B. (2005). Shape change of tensegrity structures: design and control. Proceedings of the 2005, American Control Conference, 2005.,

Veuve, N., Safaei, S. D., & Smith, I. F. (2016). Active control for mid-span connection of a deployable tensegrity footbridge. Engineering Structures, *112*, 245-255.

Xu, X., & Luo, Y. (2011). Multistable tensegrity structures. Journal of Structural Engineering, *137*(1), 117-123.

This page intentionally left blank

PASSIVE COOLING OF BREATHABLE ROOF SYSTEM IN RESIDENTIAL HOUSES: A CASE STUDY IN MALAYSIA

Sam Tan Chek Siong[1], Lim Fang Lee[2], Wai Soon Han[2*] and Chai Chang Saar[3]
[1]Ken Holdings Berhad, Menara KEN TTDI, No. 37, Jalan Burhanuddin Helmi, Taman Tun Dr Ismail, Kuala Lumpur, Malaysia.
[2]Department of Environmental Engineering, Faculty of Engineering and Green Technology, Universiti Tunku Abdul Rahman, Kampar, Perak, Malaysia.
[3]School of Engineering, Faculty of Engineering, Computing and Science, Swinburne University of Technology Sarawak, Kuching, Sarawak, Malaysia.

Abstract
Roof may transfer a huge amount of heat from the sun radiation into interior space of a building. In ordinary roof system, heat may trap in attic space and transfer into the interior building even at night-time. This will lead to thermal discomfort and reliance of air-conditioning system which increase the electricity consumption. A new passive cooling roof concept namely "breathable roof system" is introduced to mitigate this problem. This preliminary case study aims to investigate the cooling effects of the breathable roof system of residential houses in Shah Alam, Malaysia. Thermocouples were used to measure temperature in intermediate double storey terrace houses which were facing North-South and East-West directions, to quantify the effectiveness of the breathable roof system compared to the conventional roof system. Besides that, the comparisons of temperature between different house orientations and investigation of heat profile in the rooms were also conducted. The result shows that breathable roof system can reduce the heat by 12.3-19.5% compared to the conventional roof system. North-South facing houses were measured with lower temperature compared to East-West facing houses. In conclusion, the use of breathable roof system could be used as an alternative solution in conserving energy to achieve sustainable development.

Keywords: *Breathable Roof; Ventilated Roof; Sustainable Development; Passive Cooling; Thermal Comfort.*

INTRODUCTION

Cooling devices, such as air-conditioning, are commonly used in households to cool the indoor space and provide thermal comfort to the dwellers. Nowadays, more and more households in tropical countries are installing air conditioning to adapt to the climate change and gradually high temperature. The increase usage of air-conditioners has increased the electricity expenditure tremendously (Sena et al., 2021). It is estimated about 37.0% of global electricity will be used for space cooling by 2050 (IEA, 2018). Increase in electricity energy consumption will cost higher electricity bills to the dwellers. This will particularly affect low-income households in which they might need to divert a larger portion of their income for cooling demand purpose and reduce budget for other expenditures, for instance food and education (Teresa Randazzo et al., 2020).

In Malaysia, non-renewable resources are the main sources used to generate electricity, such as natural gas, crude oil and diesel (Energy Commission of Malaysia, 2017). The increasing trend of electricity demand and generation lead to rapid increase in green house gaseous and carbon dioxide emission which have significant environmental degradation and public health issues (Mrabet et al., 2019). Hence, alternative methods that are able to conserve energy and improve thermal comfort of the building occupants are required to be studied.

Roof system is one of the key factors that determine the indoor thermal conditions (Hashemi, 2016). Heat is mainly transferred through the roof system to different part of the building in single and double storey residential houses. Concrete and brick are the main construction materials in Malaysia buildings (Harun et al., 2020). When thermal mass materials, such as concrete and brick structure, exposed to heat during daytime, they have the ability to absorb and retain heat within the structure and release heat at night-time (Shafigh et al., 2018). An effective and eco-friendly roof system in tropical country should be able to promote heat dissipation and conserve energy that used for cooling indoor space purpose. Besides building materials, passive design strategies such as building orientation, thermal insulation and air tightness, shading devices, glazing area and natural ventilation, could lower energy consumption of a building (Yao et al., 2018). Therefore, this study aims to investigate the performance of breathable roof system and the measured temperature differences between houses with different orientations.

METHODOLOGY

Study Design

The design of this study is arranged in such a way that it takes into the consideration that the orientation of the houses which can influence the solar and thermal conditions and ventilation potential and building envelope material as in the Lafarge ventilation plaster board (Noor Aziah, 2015). This is in contrast stark to finding from Al-Tamimi et al. (2011) that natural ventilation strategies including orientation of the building are not as reliable and ideal for urban context. However, optimum orientation, together with passive cooling breathable roof as introduced in this study will help in achieving better indoor thermal comfort. The passive cooling breathable roof is in line with the direct non-mechanical evaporative cooling of ventilation air which is served as one of the passive and low energy systems suggested by Givoni (1990). Also, a comparative study conducted by Tatarestaghi et al., 2018 reveals that the concept of passive cooling is an alternative thermal comfort strategies applicable to tropical climates country like Malaysia.

A preliminary case study was carried out in four full-scaled double storey residential houses at Shah Alam, Malaysia from May 2013 to July 2013. Four intermediate houses, with two facing North-South direction and another two facing East-West direction, were selected for temperature monitoring in this case study. For each type of house-orientation, one house was installed with breathable roof system, another house was installed with conventional roof system. Intermediate type of residential houses was selected in this study to minimize the heat gain effect through other building envelopes, which are walls and windows.

Data Collection and Analysis

In each of the intermediate house, thermocouple temperature data loggers were installed to measure the temperature data for 24 hours continuously, with sampling interval of 15 minutes. Figure 1 shows the measurement locations of the thermocouple at various parts of the roof system and building envelope. Figure 2 and Figure 3 present the breathable roof systems installed at the double storey houses. The recorded temperature data were then compiled and keyed in into spreadsheet for data analysis. Line graphs were created to compare the trends of temperature at center attic, ridge tile and master bedroom for houses installed with breathable roof and non-breathable roof, and to compare the temperature at centre attic, ridge tile and master bedroom ceiling for East-West and North-South facing houses that equipped with non- breathable roof. Then, the heat profile for the master bedroom and bedroom 3 were further analysed by comparing the temperature recorded at the centre attic, ceiling of the rooms and indoor temperature of the rooms, for both types of roofs and directions.

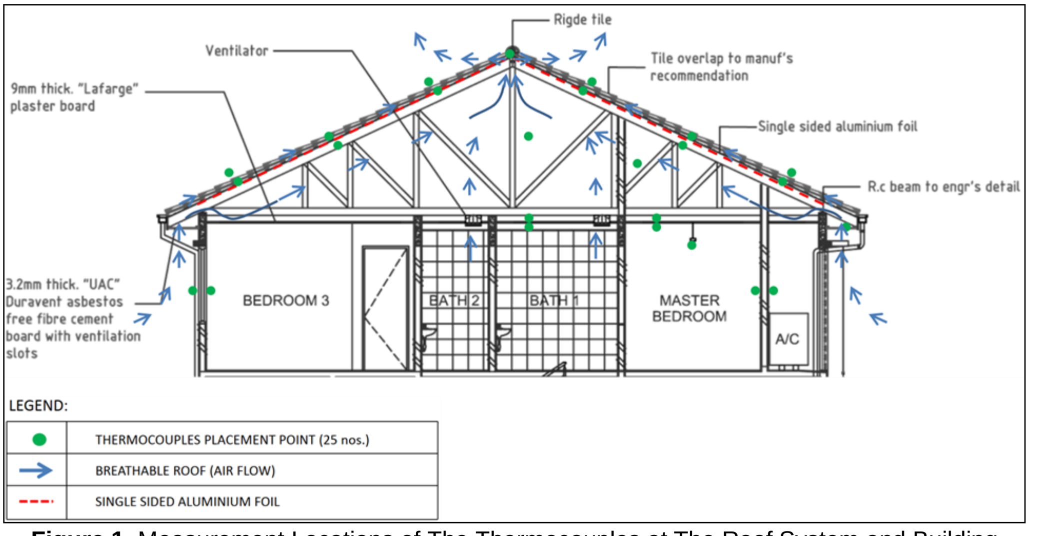

Figure 1. Measurement Locations of The Thermocouples at The Roof System and Building Envelope of The House

Figure 2. Breathable Roof System Installed at The Corner of The Double Storey Residential Houses

Figure 3. Breathable Roof Installed at The Side of The Double Storey Residential House

RESULTS AND DISCUSSION

Houses Installed with Ventilated and Conventional Roof Design

Figure 4, Figure 5 and Figure 6 showed the temperature recorded at the centre attic, ridge tile and master bedroom for both houses installed with ventilated and conventional roof, which facing the North-South direction. The highest temperatures recorded at the centre attic, ridge tile and master bedroom of house equipped with breathable roof were 36.4˚C, 31.4˚C and 33.0˚C, respectively. The highest temperature recorded at the centre attic, ridge tile and master bedroom of house with conventional roof were 41.5˚C, 39.0˚C and 35.5˚C, respectively. Compared to house installed with breathable roof, house installed with conventional rood design had higher temperature data. This suggests that the breathable roof system provides good ventilation in the roof and reduces the temperature in the ridge tile up to 7.6˚C. This finding is in line with the Karam et al. (2014) where the cooler attic would eventually result in a cooler indoor environment. An indoor thermal study carried out by Ng et al. (2019) at a two-storey corner terrace house in Kuala Lumpur, Malaysia, reported mean air temperature of 45°C measured in the attic space, mean temperature of 42°C at top surface ceiling, mean temperature of 40°C at the bottom surface ceiling and followed by mean indoor air temperature of 34°C at the family area. In conventional roof system, the heat absorbed by the ceiling will be transferred into the interior space of master bedroom by convection mechanism. However, our monitoring results showed the breathable roof system able to reduce the heat transferred into the house interior space and will have lower indoor temperature. Thus, houses installed with breathable roof system in tropical countries could be more energy efficient as less electrical energy will be utilised to cool the indoor space.

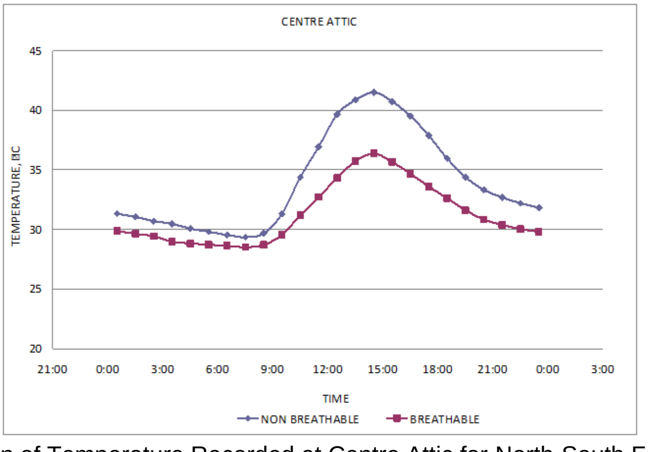

Figure 4. Comparison of Temperature Recorded at Centre Attic for North-South Facing Houses Which Equipped with Breathable Roof and Conventional Roof

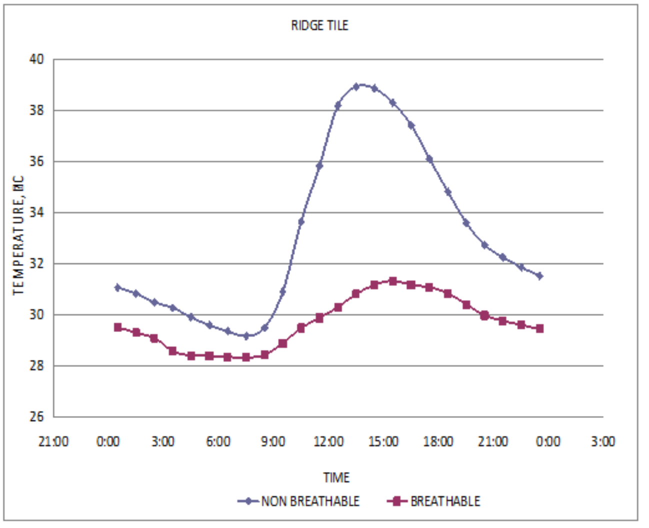

Figure 5. Comparison of Temperature Recorded at Ridge Title for North-South Facing Houses Which Equipped with Breathable Roof and Conventional Roof

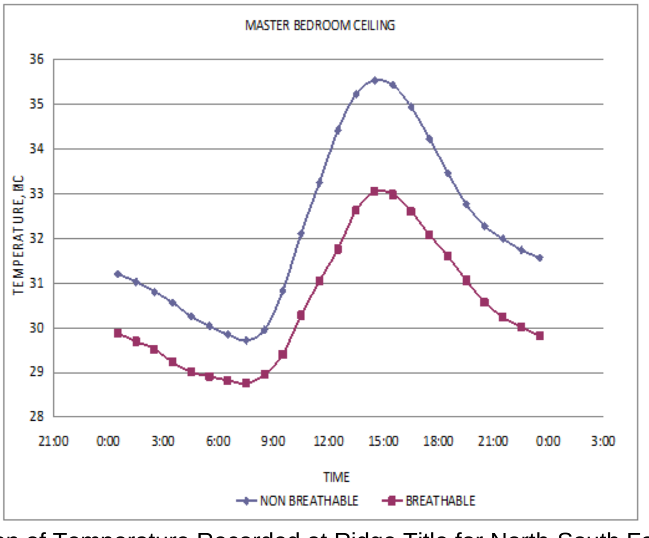

Figure 6. Comparison of Temperature Recorded at Ridge Title for North-South Facing Houses Which Equipped with Breathable Roof and Conventional Roof

Figure 7, Figure 8 and Figure 9 show the temperature recorded at the centre attic, ridge tile and master bedroom for both houses installed with breathable and non-breathable roof system, which facing the East-West direction. The highest temperatures recorded at the centre attic, ridge tile and master bedroom of house equipped with breathable roof were 38.3˚C, 40.5˚C and 34.5˚C, respectively. While the highest temperature recorded at the centre attic, ridge tile and master bedroom of house with non-breathable roof were 44.0˚C, 46.2˚C and 37.4˚C, respectively. Temperature differences at centre attic and ridge tile at these two different houses were up to 5.7 ˚C. This similar trend of higher recorded temperature at house with non-breathable roof further supports our earlier findings.

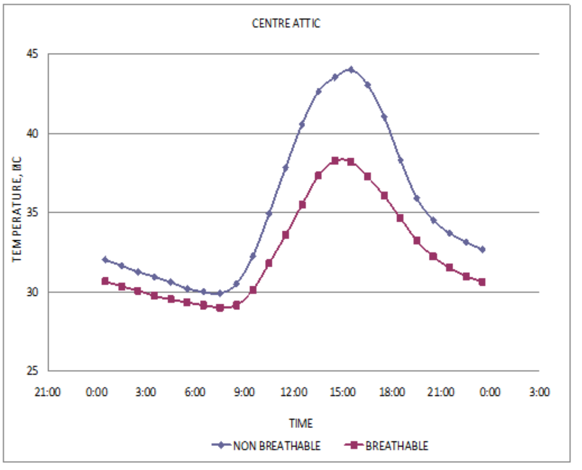

Figure 7. Comparison of Temperature Recorded at Centre Attic for East-West Facing Houses That Equipped with Breathable Roof and Non-Breathable Roof

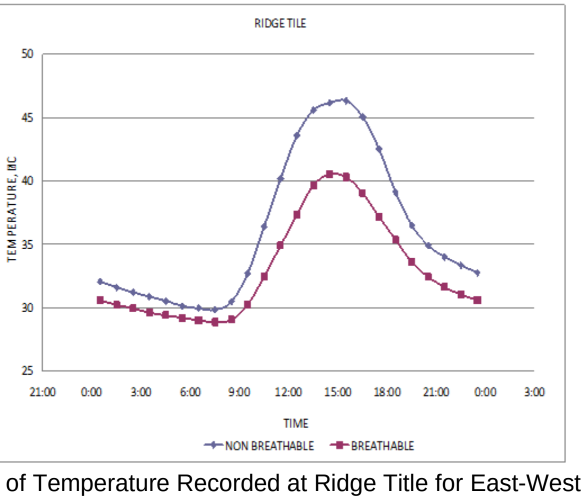

Figure 8. Comparison of Temperature Recorded at Ridge Title for East-West Facing Houses That Equipped with Breathable Roof and Non-Breathable Roof

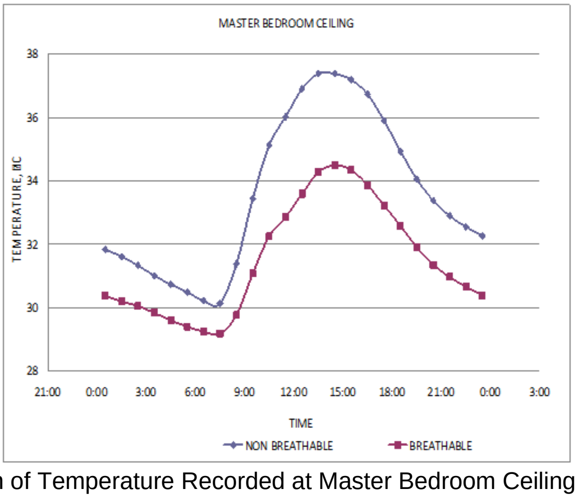

Figure 9. Comparison of Temperature Recorded at Master Bedroom Ceiling for East-West Facing Houses That Equipped with Breathable Roof and Non-Breathable Roof

Houses Orientation

Figure 10 shows the temperature profiles of roof centre attic at houses with non-breathable roof which facing the North-South and East-West direction. From the graph, it was observed that the house facing North-South direction had relatively lower temperature at the roof centre attic compared to those facing East-West direction. The lowest temperatures recorded at the roof attic was at around 7am, which were 29.3˚C for house facing North-South direction and 29.9˚C for house facing East-West direction. The highest temperatures recorded at the roof attics were 44.0˚C and 41.5˚C for house facing East-West and North-South direction, respectively. House facing North-South direction has lower temperature because it has relatively less direct sun exposure compared to those facing the East-West direction. Similar trend of finding was reported in other previous study that solar heat gain in building facing East-West directions were higher than heat gain in buildings facing North-South directions (Hashemi and Khatami, 2017; Yao et al., 2018). This is due to heat radiation from the sun is stronger in the east and west orientations (Wong and Li, 2007). Thus, houses that facing east and west orientations are exposed to more solar radiation and will trap more heat in the building envelops and being released into the interior space of the building.

Figure 11 shows the heat profile of ridge tile for houses installed with conventional roof which facing North-South and East-West direction. It was observed that the temperature increased significantly from 7 am to 1 pm from 29.2-39.0˚C for North-South direction and 29.9-46.3˚C for East-West direction. The drastic increase in heat at ridge tile for East-West direction was mainly caused by the longer hours of direct sunlight exposure onto the roof tile.

Figure 12 shows the temperature profile at the ceiling of the master bedroom for conventional roof house facing North-South and East-West direction. The highest temperatures at the master bedroom ceiling at approximately 2.30pm were 37.7˚C and 35.5˚C respectively for East-West and North-South direction.

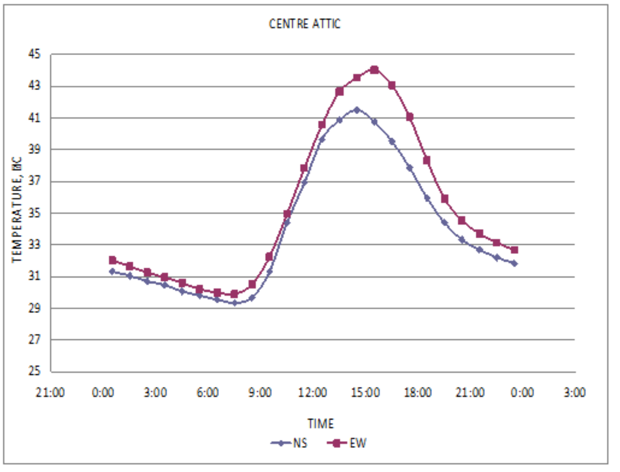

Figure 10. Comparison of Temperature Recorded at Centre Attic for East-West and North-South Facing Houses That Equipped with Non-Breathable Roof

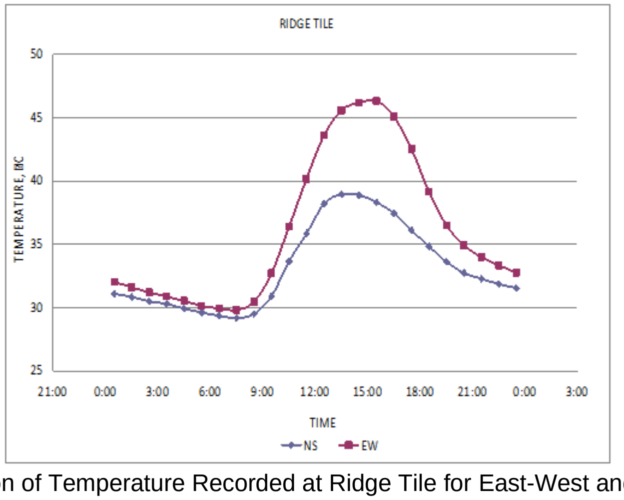

Figure 11. Comparison of Temperature Recorded at Ridge Tile for East-West and North-South Facing Houses That Equipped with Non-Breathable Roof

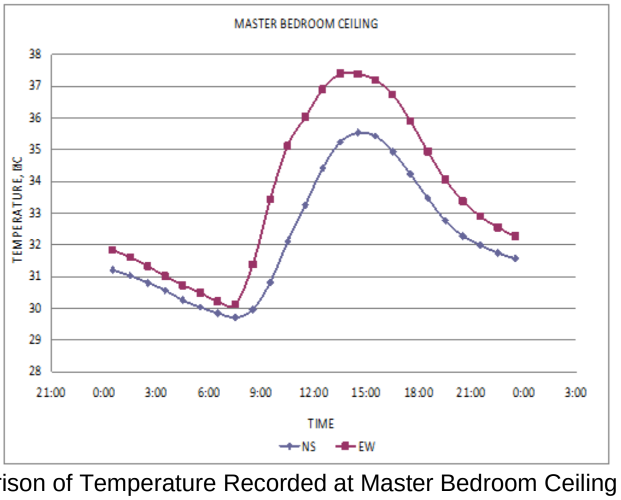

Figure 12. Comparison of Temperature Recorded at Master Bedroom Ceiling for East-West and North-South Facing Houses That Equipped with Non-Breathable Roof

Heat Profile of Room with Breathable and Non-breathable Roof System

Figure 13 and Figure 14 show the heat profile of the master bedroom for houses facing North-South direction that installed with conventional and breathable roof, respectively. The centre attic shows the highest temperature followed by the master bedroom ceiling and the lowest temperature was recorded in the indoor environment of the master bedroom between 9am to 1am. The radiant heat from the sunlight increased the temperature significantly at the centre attic and ceiling of master bedroom between 8am to 3pm and dropped drastically after that. However, the radiant from the sunlight only give little impact to the indoor temperature of the master bedroom. From the Figure 6 (a) and 6 (b), it was observed that the indoor temperature of the master bedroom increased slowly from 9 am to 7pm. There was a delay of approximately 4 hours of time between the highest temperature in the centre attic and master bedroom ceiling as compared to the indoor heat in the master bedroom. The temperature in the master bedroom cooled slowly since the room was properly closed without allowing ventilation to happen. It is suggested that the cooling process in the master bedroom can be expedited by opening the windows or by installing exhaust fan to provide better ventilation. Good ventilation after the sunset will allow cool air to flow into the master bedroom. Thus, the master bedroom can cool down in a shorter time through convection mechanism.

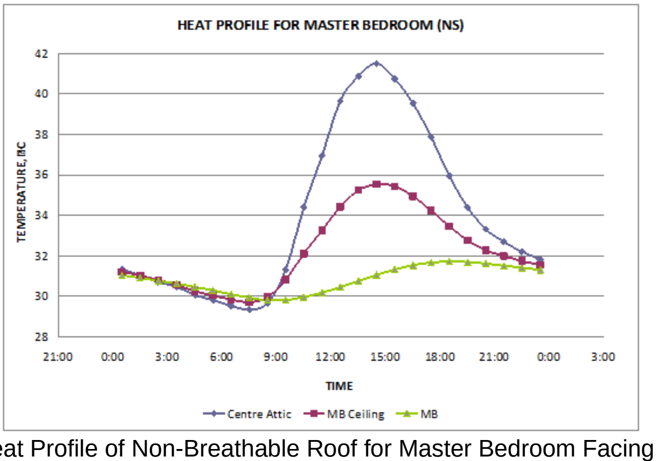

Figure 13. Heat Profile of Non-Breathable Roof for Master Bedroom Facing North-South

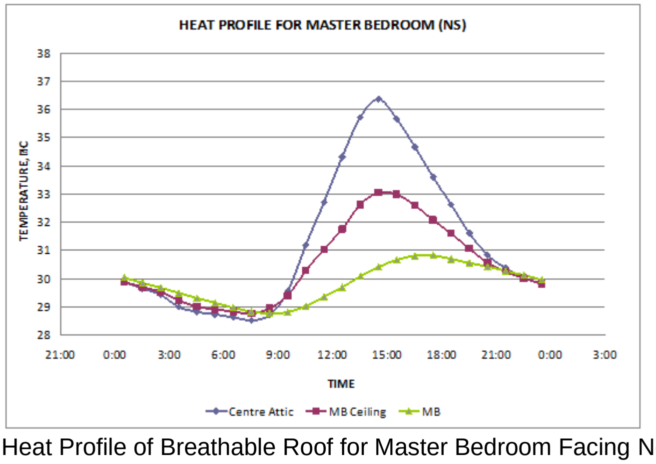

Figure 14. Heat Profile of Breathable Roof for Master Bedroom Facing North-South

Figure 15 and Figure 16 show the heat profile of the master bedroom for conventional and breathable roof house facing East-West direction, respectively. The master bedroom which is facing East direction is strongly influenced by the radiant heat of the sun. It was observed that the indoor temperature and the temperature at the ceiling of the master bedroom increased rapidly from 9am and reached the peak at approximately 2pm and followed by a quick drop after that as the sun sets in the West. In present study, the centre attic and the ceiling of the master bedroom which is well ventilated by the breathable roof expedite the reduction in temperature. The indoor temperature in the master bedroom installed with conventional roof demonstrated as low reduction in temperature since the room was poorly ventilated. Similar findings were reported by other studies that carried out in poorly ventilated house or room at two-storey terraced houses in Malaysia. Kubota et al. (2009) reported indoor air temperature range from 29.5°C – 32.4°C in houses with no ventilation at Johor Bahru; while Ng et al. (2019) reported indoor air temperature range from 30.9°C – 32.2°C in rooms without ventilation at Kuala Lumpur.

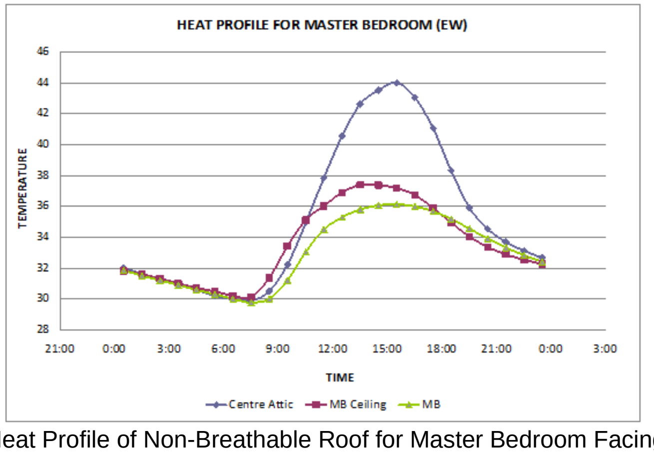

Figure 15. Heat Profile of Non-Breathable Roof for Master Bedroom Facing East-West

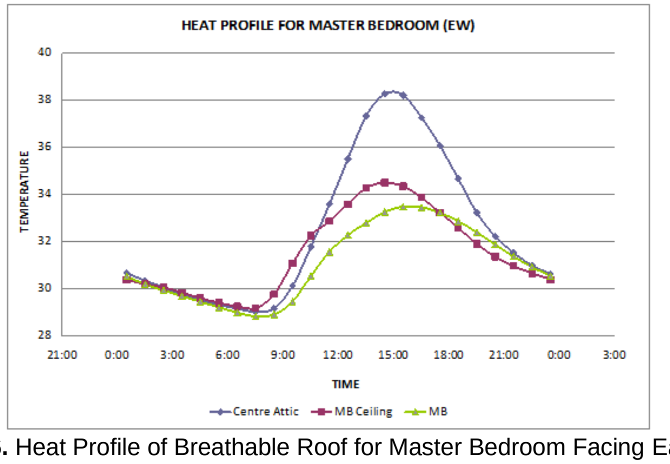

Figure 16. Heat Profile of Breathable Roof for Master Bedroom Facing East-West

Figure 17 and Figure 18 show the heat profile for Room 3 installed with conventional roof and breathable roof which facing North-South direction, respectively. It was observed that the heat at the centre attic increased rapidly as the sun rising. The temperature of ceiling and indoor temperature of Room 3 increased slowly through convection from the centre attic in the morning and afternoon. The indoor temperature of Room 3 reduced slowly after the sunset since it was poorly ventilated. In this study, the indoor temperature in Room 3 was slightly higher than the centre attic and ceiling at night-time which might be due to the heat trapped in the interior space of the enclosed room. The thermal comfort in the room can be further improved by providing good ventilation.

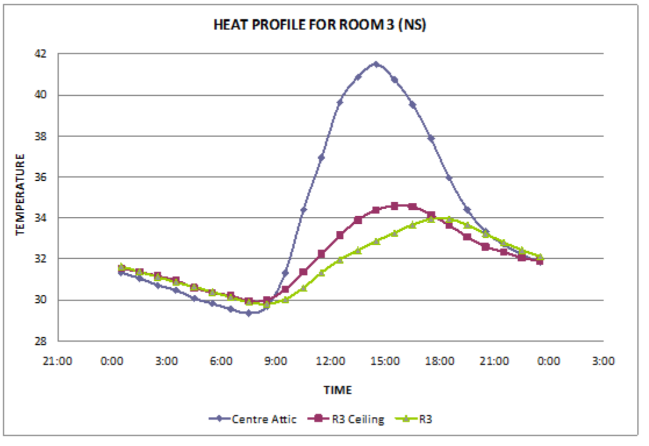

Figure 17. Heat Profile of Non-Breathable Roof for Room 3 Facing North-South

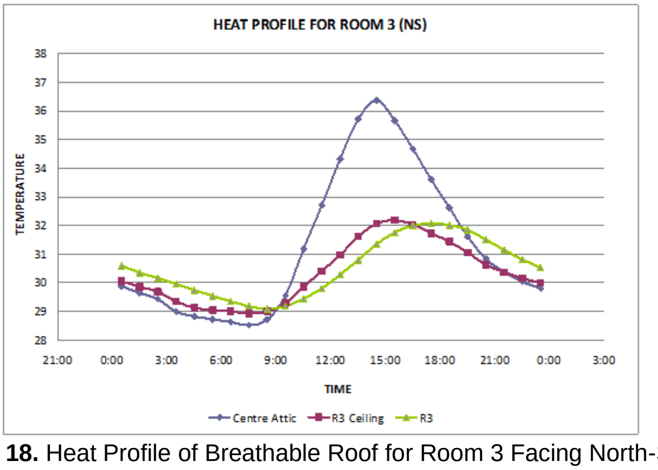

Figure 18. Heat Profile of Breathable Roof for Room 3 Facing North-South

Figure 19 and Figure 20 show the heat profile of Room 3 installed with conventional roof and breathable roof which facing East-West direction, respectively. Room 3 which was facing West direction is strongly influenced by the radiant heat of the sun in the evening. It was observed that the indoor temperature of Room 3 increased gradually from 9am to 6pm and cooled down slowly after that. Similar trend of results was reported in a previous study where the room that installed with conventional 4-mm thick cement board ceiling and facing west orientation, was measured with higher mean indoor temperature during evening and night-time due to external wall of the room acted as a thermal mass to absorb heat in the evening and release heat to the room during the night (Ng et al., 2019).

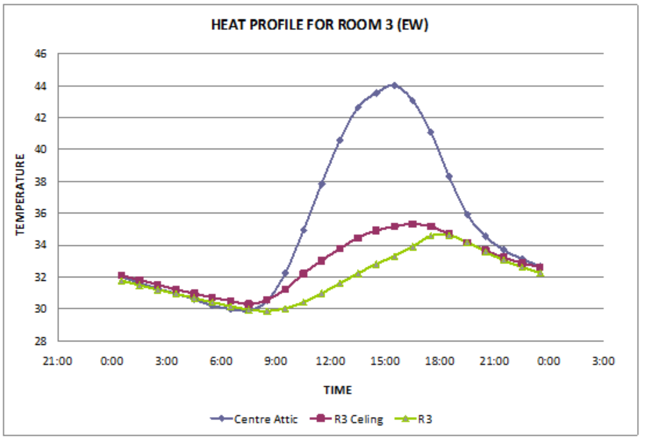

Figure 19. Heat Profile of Non-Breathable Roof for Room 3 Facing East-West

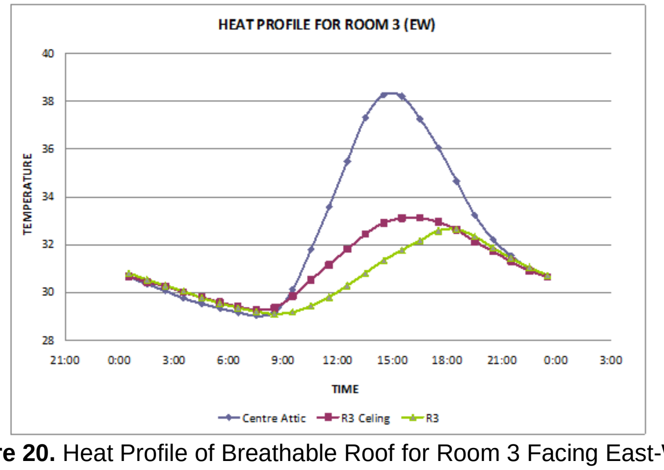

Figure 20. Heat Profile of Breathable Roof for Room 3 Facing East-West

Different types of passive cooling techniques have been studied in recent decades. In China, Chen et al. (2015) found that the passive evaporation cooling wall (PECW) which is constructed by using a pipe-shaped ceramics could reduce the surface temperature of about 4°C to 6°C below the ambient and is suitable for dry and hot climates because the design utilises the concept of capillary force to absorb water. As for cooling roof, Alturki and Zaki (1990) found that the effect of intermittent spraying of a building's roof could reduce the cooling load of 40% for hot dry conditions in the context of Saudi Arabia through a numerical modelling. However, this approach is rather an active mean to reduce air conditioning load rather than a passive mean. In addition, Wang et al. (2007) found that a combination of cooling ceiling and microencapsulated phase change material (MPCM) slurry storage to enhance the evaporative cooling potentials so as to achieve the passive cooling effect for building. The study highlighted the hybrid system could save energy of a building up to 60% in northwestern China climate and up to 10% in southeastern China climate. Thus, it can be concluded that the effectiveness of passive cooling technique is mainly dependent on geographic location where the weather variables such as temperature, precipitation, pressure, wind, humidity and cloudiness play a significant role in determining the evolution of passive cooling technology. Apart from the geographic location, passive cooling studies focus either single system or hybrid system.

The common passive cooling techniques that have been studied in Malaysia with hot and humid climate including night ventilation, roof cover, roof or ceiling insulation, windcatcher, window and wall shading, small courtyard concept and microclimate modification (Nejat et al., 2021; Ng et al., 2020; Toe & Kubota, 2015; Kubota, Chyee & Ahamad, 2009). However, there is lack of local research on innovative roof with passive cooling strategy. As such, a Malaysian context passive cooling technique known as breathable roof system is proposed in this study.

A well-design ventilated roof improves the overheating condition at the attic (Ciampi et al., 2005). Ismail et al. (2012) further enhanced that the ventilated roof could play a role in reducing indoor temperature by as much as 8^0C. Existing practices of ventilated roof often tends to be active in nature with solar ventilators installed on the roof to disperse the trapped hot air. Also, Abdul Rahman et al. (2019) highlighted that the efficiency of stack effect which occurs because of the hot air travelling from an area with low pressure to an area with high pressure is depended on the ease of air movement inside the building. This study, however, further enhance the stack effect by incorporating the ventilated plaster board as shown in Figure 2. The hot trapped air is dispersed through a roof top which includes a plurality of rafters, arranged at a sloping angle to meet at the peak of a roof and forming a triangular shaped roof top, with such rafter attaching to a plurality of battens to support a plurality of roof tiles which are installed on the surface of the battens, wherein such battens will raise the roof tiles off the rafter leaving space in between to create the first air passage way. This is supported by a study conducted by Ibrahim et. al. (2014) where the more easier the hot air trapped underneath the roof the more indoor comfort could be achieved by the houses.

The roof top is positioned over the ceiling to provide an attic space and a breathable membrane with pre-punched hole which is attached at the peak of the roof top and covered by ridge tiles which is placed on breathable membrane with pre-punched holes to provide a second air passageway that connected to the first air passageway of the roof top as shown in Figure 1.

CONCLUSION

In this study, it can be concluded that breathable roof concept is efficient in reducing heat transfer into the interior space of the building through housing roof element. Good ventilation in the roof system could reduce the temperature up to 5.1°C at the attics up to 5.1°C, up to 2.1°C at master bedroom and Room 3. House orientation that facing North-South direction has showed lower temperature up to 1.9°C at the centre attic, 2.7°C at master bedroom and

0.4°C at Room 3 as compared to house facing East-West direction. Thus, houses installed with breathable roof and facing North-South direction could be an alternative of sustainable and green choice to reduce the dependency on air-conditioning which require higher electricity energy expenditure.

The breathable roof system demonstrates that it could be an alternative passive roof ventilation to achieve better indoor comfort. As the breathable roof utilised the combination of ventilators located at the upper floor's bathrooms and the fibre cement board with ventilation slots installed at roof eaves, it basically incurs no additional construction cost. As such, the breathable roof shall be widely adopted and it could even be accepted as one of the roofing design to achieve the assessment criteria of indoor environmental quality for the Green Building Index (GBI) in Malaysia.

ACKNOWLEDGEMENT

This study was self-funded by Ir Sam Tan Chek Siong. The roof has been filed for Malaysian Patent (PI2014701635) on the 18th of June 2014 and granted a patent with grant number MY-181538-A on the 26th of December 2020.

REFERENCE

Abdul Rahman, M. A., Abdul Samad, M. H., Bahauddin, and A., Ismail., M. R. (2009). Towards a Low-Energy Building Design for Tropical Malaysia. Penerbit Universiti Sains Malaysia, Penang, Malaysia, 198. pp.

Al-Tamimi, N. A. M., Syed Fadzil, S. F., and Wan Harun, W. M. (2011). The Effects of Orientation, Ventilation and Varied WWR on the Thermal Performance of Residential Rooms in the Tropics. Journal of Sustainable Development, 4(2): 142-149. DOI:10.5539/jsd.v4n2p142.

Al-Turki, A. M., Zaki, G. M. (1991). Energy Saving through intermittent evaporative roof cooling. Energy and Buildings, 17(1): 35-42. https://doi.org/10.1016/0378-7788(91)90069-F.

Chen, W., Liu, S., Lin, J. (2015). Analysis on the passive evaporative cooling wall constructed of porous ceramic pipes with water sucking ability. Energy and Buildings, 86: 541-549. https://doi.org/10.1016/j.enbuild.2014.10.055.

Ciampi, M., Leccese, F., and Tuoni, G. (2005). Energy Analysis of Ventilated and Microventilated Roofs. Solar Energy 79(2): 183-192. https://doi.org/10.1016/j.solener.2004.08.014.

Givoni, B. (1991). Performance and Applicability of Passive and Low-energy Cooling Systems. Energy and Buildings, 17(1991): 177-199. https://doi.org/10.1016/0378-7788(91)90106-D.

Dimoudi, A., Androutsopoulos, A., and Lykoudis, S. (2006). Summer Performance of a Ventilated Component. Energy and Building, 38(2006): 610-617. https://doi.org/10.1016/j.enbuild.2005.09.006.

Energy Commission of Malaysia. (2017). Peninsular Malaysia Electricity Supply Industry Outlook 2017. Energy Commission of Malaysia: Kuala Lumpur.

Givoni, B. (1991). Performance and Applicability of Passive and Low-energy Cooling Systems Energy and Buildings, 17(1991): 177-199. DOI:10.1016/0378-7788(91)90106-D.

Hashemi, A. & Khatami, N. (2017). Effects of solar shading on thermal comfort in low-income tropical housing. Energy Procedia, 111, 235-244.

Hashemi, A. (2016). Climate resilient low-income tropical housing. Energies, 9, 468. doi: 10.3390/en9060468.

Ibrahim, S.H., Azhari, N.A., Nawi, M.N.M., Baharun, A., and Affandi, R., (2014). Study on the effect of the roof opening on the temperature underneath. Int. J. Appl. Eng. Res. 9 (23), 20099–20110.

International Energy Association (IEA). The Future of Cooling. Opportunities for Energy-Efficient Air Conditioning OECD/IEA (2018).

Ismail, M., Malek, A., and Rahman, A., (2012). Stack ventilation strategies in architectural context: a brief review of historical development, current trends and future possibilities. IJRRAS 11 (2), 291–301.

Karam, M. A., Mazran, I., Abdul M. A. R. (2014). A Review of the Potential of Attic Ventilation by Passive and Active Turbine Ventilators in Tropical Malaysia. Sustainable Cities and Society, 10: 232-240. https://doi.org/10.1016/j.scs.2013.10.001.

Kubota, T., Chyee, D. T. H. & Ahmad, S. (2009) The effects of night ventilation technique on indoor thermal environment for residential buildings in hot-humid climate of Malaysia, Energy and Buildings, 41, 8, 829-839. https://doi.org/10.1016/j.enbuild.2009.03.008.

Li, D., Zheng, Y., Liu, C., Qi, H., and Liu, X. (2016). Numerical Analysis on Thermal Performance of Naturally Ventilated Roofs with Different Influencing Parameters. Sustainable Cities and Society, 22(2016): 86-93. https://doi.org/10.1016/j.scs.2016.02.004.

Nejat, P., Ferwati, M. S., Calatit, John, C., Ghahramani, A., Sheikhshahrokhdehkordi, M. (2021) Passive cooling and natural ventilation by the windcatcher (Badgir): An experimental and simulation study of indoor air quality, thermal comfort and psaaive cooling power, Journal of Building Engineering, 41, 102436. https://doi.org/10.1016/j.jobe.2021.102436.

Ng, W. T., Zaki, S. A., Hagishima, A., Rijal, H. B. and Yakub, F. (2020) Affordable retrofitting methods to achieve thermal comfort for a terrace house in Malaysia with a hot-humid climate. Energy and Buildings, 223, 110072. https://doi.org/10.1016/j.enbuild.2020.110072.

Ng, W. T., Zaki, S. A., Hagishima, A., Rijal, H. B., Zakaria, M. A., and Yakub, F. (2019) Effectiveness of free running passive cooling strategies for indoor thermal environments: example from a two-storey corner terrace house in Malaysia. Building and Environment, 160, 106214. https://doi.org/10.1016/j.buildenv.2019.106214.

Noor Aziah, M. A. (2015). Thermal Comfort and Energy Solutions for a better Residential Environmental Malaysia. In Planning Malaysia. Volume XIII (2015): 37-50. DOI: http://dx.doi.org/10.21837/pm.v13i5.138.

Payam, S., Asadi, I., and Mahyuddin, N. (2018) Concrete as a thermal mass material for building applications - A review, Journal of Building Engineering, 19, 14-25. https://doi.org/10.1016/j.jobe.2018.04.021.

Ramos, J., Aires, L. (2020). The Effect of a Naturally Ventilated Roof on the Thermal Behaviour of a Building under Mediterranean Summer Conditions. Journal of Sustainable Development of Energy, Water and Environment Systems. 8(30): 508-519. DOI: http://dx.doi.org/10.13044/j.sdewes.d7.0297.

Sena, B., Zaki, S. A., Rijal., H. B., Ardila-Rey, J. A., Yusoff, N. M., Yakub, F., Ridwan, M. K., and Muhammad Sukki, F. (2021). Determinant factors of electricity consumption for a Malaysian household based on a field survey. Sustainability, 13, 818. doi: 10.3390/su13020818.

Sunwoo Lee, Sang Hoon Park, Myong Souk Yeo, and Kwang Woo Kim. (2009). An Experimental Study on Airflow in the Cavity of a Ventilated Roof. Building and Environment, 44(7): 1431-1439. https://doi.org/10.1016/j.buildenv.2008.09.009.

Tatarestaghi, F., Ismail, M. A., and Ishak, N. H. (2018). A Comparative Study of Passive Design Features/Elements in Malaysia and Passive House Criteria in the Tropics. Journal of Design and Built Environment, 18(2): 15-25. https://doi.org/10.22452/jdbe.vol18no2.2

Teresa Randazzo, Enrica De Cian, and Malcolm N. Mistry. (2020). Air conditioning and electricity expenditure: the role of climate in temperate countries, Economic Modelling, 90, 273-287.

Toe, D. H. C. & Kubota, T. (2015) Comparative assessment of vernacular passive cooling techniques for improving indoor thermal comfort of modern terraced houses in hot-humid climates of Malaysia, Solar Energy, 114, 229-258. https://doi.org/10.1016/j.solener.2015.01.035.

Wang, X., Niu, J., van Paassen, A. H. C. (2008). Raising Evaporative Cooling Potentials using Combined Cooled Ceiling and MPCM Slurry Storage. Energy and Buildings, 40(9): 1691-1698. https://doi.org/10.1016/j.enbuild.2008.02.028.

Wong, N.H., and Li, S. (2007). A Study of the Effectiveness of Passive Climate Control in Naturally Ventilated Residential Buildings in Singapore. Building and Environment. 42(2007): 1395-1405. https://doi.org/10.1016/j.buildenv.2005.11.032.

Yao, R., Costanzo, V., Li, X., Zhang, Q. & Li, B. (2018) The effect of passive measures on thermal comfort and energy conservation. A case study of the hot summer and cold winter climate in the Yangtze River region. Journal of Building Engineering, 15, 298-310.

Zambri Harun, Eslam Reda, Alaa Abdulrazzaq, Ashraf Amer Abbas, Yusri Yusup, and Sheikh A. Zaki. (2020) Urban heat island in the modern tropical Kuala Lumpur: Comparative weight of the different parameters, Alexandria Engineering Journal, 59, 6, 4475-4489. https://doi.org/10.1016/j.aej.2020.07.053.

Zouhair Mrabet, Mouyad Alsamara, Ali Salman Saleh, Sajid Anwar. (2019). Urbanization and non-renewable energy demand: A comparison of developed and emerging countries. Energy, 170, 832-839. DOI: 10.1016/j.energy.2018.12.198.

REDUCTION OF CARBON FOOTPRINT WITH GEOPOLYMERIC CONCRETE AND RECYCLED AGGREGATE – A CRITICAL REVIEW

Vidhya Kanakaraj[1] and Clementz Edwardraj Freeda Christy[1,2*]
[1,2]Department of Civil Engineering, Karunya Institute of Technology and Sciences (Deemed to be University), Karunya Nagar, Coimbatore 641 114. Tamil Nadu, India.
[2]Department of Civil Engineering, Kalasalingam Academy of Research and Education (Deemed to be University), Anand Nagar, Krishnankoil – 626 126. Tamil Nadu, India.

Abstract
The infrastructure development increased the of cement production requirement. During the cement manufacturing process, more emission of carbon dioxide pollutes the environment. For an eco-friendly concrete, need for an alternative binder material arises. For the material to be an eco-friendly, instead of cement as the binder, the alkaline activators in combination with sodium / potassium silicates as the binder and with the recycled aggregate as a part of the coarse aggregate may be used. Reuse of recycled aggregate from concrete waste lead to economic utilization of raw materials and increases the sustainability concept. But the cement mortar adhered over the recycled aggregate forms the weak porous layer that affects the interfacial behaviour of the aggregate phase and cement phase that reduces the strength. A critical review has been made on the recycled aggregates in geopolymer concrete were summarized and presented in this article. More studies are still needed to enhance the strength and the durable properties with additives in geopolymer concrete with the recycled aggregate.

Keywords: *Geopolymer; Recycled Aggregate; Carbon Footprint; Binder; Alkaline activator; Geopolymerization.*

INTRODUCTION

In the infrastructure development, concrete is a widely utilized material. In Portland cement concrete, the cement pastes bind the aggregates and make the concrete hard and strong. But, the production of cement affects the sustainability (Rao, 2000) as, it releases one tonne of carbon dioxide (CO_2) (i.e.) greenhouse gases, into the environment for every tonne production of cement (Joseph Davidovits, 1993; Gartner, 2004). These gases affect the environment to a greater level which may lead to the global warming and leaves the carbon footprint. An alternative binding material is required to reduce the carbon footprint in turn to reduce the carbon footprint (Rangan, 2008). Geopolymer concrete (GC) is reported to be an alternative material that reduces the carbon footprint. It ensures sustainability and gain the acceptance worldwide (Duxson et al., 2007). The sustainable reasons for GC are indicated in Figure 1.

Geopolymer Concrete

Geopolymer concrete reduces the cement production and thereby reduces the carbondioxide emission and leads to a sustainable environment (Duxson et al., 2007; Meyer, 2009, Malayali, 2002). Geopolymer concrete enhances the concrete sustainability with the reduction of about 80% of embodied carbon (Ahmad et al., 2021) than the conventional concrete. Geopolymers, are the inorganic polymers with amorphous microstructure than crystalline structure (Bakri et al., 2011; Srinivasan and Sivakumar, 2013; Nergis et al., 2018). Based on the requirement of the end users, availability, cost and application, the source materials for geopolymer concrete can be chosen.

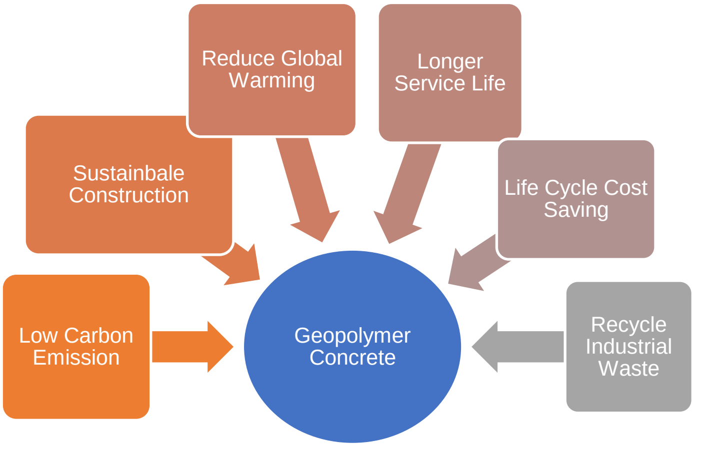

Figure 1. Sustainable Reasons for Geopolymer Concrete (Duxson et al., 2007)

Geopolymerization

In 1970's Davidovits developed geopolymers with the industrial waste products like flyash, SiO_2, rice-husk ash, steel slag granules, etc that are rich in aluminosilicate. The powdery aluminosilicates are activated with the basic activator like NaOH or KOH in combination of sodium/potassium silicate solution and form as binder paste and hardens within short duration by exothermic polymerisation reaction (Xu and Van Deventer 2000, Cong and Cheng, 2021). The geopolymerization takes place with the alkaline activator that catalyse the aluminosilicate from industrial waste / by-product and bind the materials. The aluminosilicate gel formation determines the geopolymer characteristics (Živica et al., 2014).

Recycled Aggregate Concrete (RAC)

The demolished concretes are disposed as landfills, possesses threat to humanity. Utilization of recycled aggregates as construction materials are inevitable (Vaishnu Devi et al., 2021). The demolished concretes can be crushed or uncrushed and the aggregates may be recycled to reduce the disposal problem and to control the environmental pollution to a greater extent. The mechanical characteristics are investigated with the mineral admixtures in geopolymer concrete. The variables and contents of the recycled aggregate are summarised in Table 1.

Properties of GRAC

Concrete with Geopolymeric binder produce wide range of strength development mechanism with mechanical properties (Nuruddin et al., 2016). Mechanical properties and the durability properties of geopolymer concrete and with recycled aggregate are discussed.

Table 1. Variables and The Contents of The Recycled Aggregate in GRAC

Reference	Source Material	Curing	Variable	Recycled Aggregate Content
Shaikh (2016)	Class F Fly ash	Steam curing	Recycled coarse aggregate content	15, 30 & 50%
Liu et al. (2016)	Class F Fly ash	Ambient temperature	Water cement ratio	55% coarse aggregate, 18% medium aggregate and 27% fine aggregates
Nuaklong et al. (2016)	Calcium rich flyash	Heat curing	NH concentrations	100%
Nuaklong et al. (2018)	High calcium flyash	Heat curing	Metakaolin	100%
Ridzuan et al. (2014)	Wastepaper sludge ash	Ambient temperature	NH concentrations Curing - ambient, oven & external	100%
Shi et al. (2012)	Class F Flyash	Heated at 80°C in the oven for a day, and further under ambient temperature	Recycled coarse aggregate content	0, 50 & 100%
Xie et al. (2019)	Flyash & GGBS	Demoulded after 24 h and heated at 80°C for 24 hours in the oven, and further 20^0 C till the date of testing	GGBS/fly ash weight ratio and water to binder ratio	100%
Xie et al. (2019)	Flyash & GGBS (1:1)	Heated at 80°C in the oven for 24 hours after demoulding and further 20^0 C till the date of testing.	Water/binder ratio and recycled aggregate	0,30,50,70 & 100%
Koushkbaghi et al. (2019)	Metakaolin	Ambient temperature	Recycled concrete aggregate and sodium silicate (SS) to sodium hydroxide (SH) ratios	10, 20 & 30%

Compressive Strength

Geopolymer concrete with the recycled coarse aggregate as part of the conventional aggregate as 15%, 30% & 50%, and observed 6% higher compressive strength (Xie et al., 2019; Nuaklong et al., 2018; Liu et al., 2016). The geopolymeric recycled aggregate concrete (GRAC) showed increased compressive strength with the concentration of additives. The concentration of NaOH influence the compressive strength of geopolymer concrete with recycled aggregate concrete (Ridzuan et al., 2014). The geopolymer concrete prepared with the conventional aggregates at 8, 12, and 16 Molarity of NaOH resulted in the compressive strength of 40.0, 41.4, and 38.4 MPa respectively and with the recycled concrete aggregates found as 30.6, 38.4, and 34.8 MPa respectively and 12 Molarity concentration was found to be optimum. The gel formation depends on the alkali-hydroxide ion concentration (Herwani, 2018). The weak chemical reaction with the low alkali hydroxide concentration in geopolymer concrete reduced the compressive strength (Nuaklong et al., 2016). The hydrated cement mortar overlayed on the recycled aggregates also modify the properties of concrete (Serina and Engelsen, 2018; Rao et al., 2011; Thomas et al., 2022). The presence of metakaolin in geopolymer concrete enhanced the compressive strength with the conventional aggregate as well as recycled aggregate (Nuaklong et al., 2016). Curing method also impact the compressive strength of the geopolymer concrete. Generally, steam curing and ambient curing methods are preferred. Among these two, the steam cured method showed best results

(Xie et al., 2019) for flyash based geopolymer concrete. It was reported that the hydrated gels of ground granulated blast-furnace slag (GGBS) increase the bond of the GGBS and fly ash matrix within the geopolymer concrete. The GGBS and water–binder ratio can influence the compressive strength of GRAC (Xie et al., 2019). The compressive strength of geopolymerized recycled aggregate concrete with the sodium silicate (SS) and sodium hydroxide (SH) ratio as 2, 2.5 and 3 is shown in Figure 2.

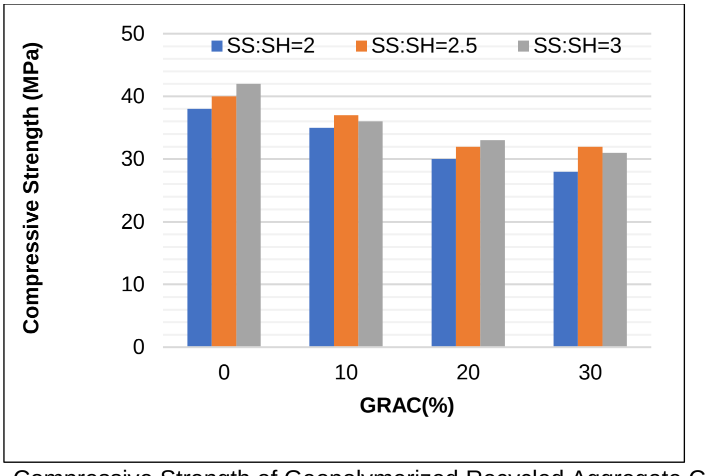

Figure 2. Compressive Strength of Geopolymerized Recycled Aggregate Concrete (Koushkbaghi et al., 2019)

From Figure 2, it was found that the mortar at the interface may affect the strength of aggregate and binder. As the quantity of recycled aggregate is increased, the compressive strength is found to be lowered (Koushkbaghi et al., 2019). Also, it is reported that high water-binder ratio and the porosity reduces the strength. The activation process with GGBS and fly ash can be reduced when the alkali concentration is lowered (Xie et al., 2019). Geopolymer concrete with recycled aggregate (GRAC) exhibited excellent performance compared with the normal concrete and with the recycled aggregate concrete (Xie et al., 2019).

Tensile Strength

It was reported that the tensile strength of geopolymer concrete may be influenced by the recycled aggregate (Shaikh, 2016). Ordinary Portland cement containing 50% recycled aggregate concrete has marginal reduction in indirect tensile strength on 7 and 28 days (Shaikh et al., 2015). The geopolymer concrete with 12 M of NaOH gave the highest split tensile strength with crushed limestone as aggregate (Nuaklong et al., 2016). The strength properties of geopolymerized concrete are shown in Table 2.

The tensile strength of the geopolymer concrete with recycled aggregate was reduced upto 37% than the natural aggregate geopolymer concrete (Nuaklong et al., 2018). An average of 25% reduction is observed in the flexural strength of geopolymer concrete with recycled aggregate than the geopolymer concrete with natural aggregate (Shi et al., 2012), due to the interface separation because of hydrated mortar on the recycled aggregate (Rao et al., 2011; Thomas et al., 2022).

Table 2. Strength Properties of Geopolymerized Concrete with Recycled Aggregate

References	Series	Parameter	Compressive Strength (MPa)		Split Tensile Strength (MPa)		Flexural Strength (MPa)
			7 days	28 days	7 days	28 days	7 days
Shaikh 2016	GPC 0	RA content	41.1	45.3	3.9	4.4	-
	GPC15		40.6	41.8	3.7	4.1	-
	GPC30		37.4	37.6	3.1	3.9	-
	GPC50		35.0	36.8	3	3.7	-
Nuaklong et al. (2016)	8M	NH concentration	30.6		2.9	-	4
	12M		38.4	-	4	-	5.3
	16M		34.8	-	3.9	-	4.6
Nuaklong et al. (2018)	0 MKC	Metakaolin content	32.9	-	2.7	-	3.6
	10 MKC		40.4	-	3.1	-	4.3
	20 MKC		45	-	3.5	-	6.1
	30 MKC		47.2	-	3.4	-	6
Liu et al. (2016)	GRAC-1	w/b ratio	-	27.15	-	-	-
	GRAC-2		-	25.51	-	-	-
	GRAC-3		-	18.04	-	-	-
	OPC-RAC		-	25.68	-	-	-

Flexural Strength

From Table 2, the flexural strength of geopolymer recycled aggregate concrete with 12 Molarity NaOH is found to be 5.3 MPa (Nuaklong et al., 2016) and with 20% Metakaoline geopolymer concrete, the flexural strength has been enhanced to 6.1 MPa and with fibers it enhances the strength further (Nuaklong et al., 2018; Meor Ahmad Faris, 2022).

Elastic Modulus

The structural parameters of geopolymerized concrete containing recycled concrete aggregate are presented in Table 3. The elastic modulus is reduced by 42% when 50 percent of conventional aggregate is replaced with recycled concrete aggregate. The modulus of elasticity is reduced as porosity and weak inter-transition zone of the recycled coarse aggregate led to microcracks in geopolymer concrete (Shaikh, 2016).

From Table 3, the density and the elastic modulus of geopolymer recycled aggregate concrete, GRAC specimen is found lesser than the recycled aggregate concrete (Shi et al., 2012). The elastic modulus of geopolymer recycled aggregate concrete has been improved with GGBS/fly ash ratios of 1:1 and 2:1, due to the interface bond between the geopolymer matrix and the aggregate matrix (Xie et al., 2018; Xie et al., 2019).

Table 3. Structural Properties of Geopolymerized Concrete with Recycled Aggregate

References	Series	Elastic Modulus (GPa)		Poisson's ratio	Density (kg/m^3)
		7 days	28 days		
Shaikh (2016)	GPC0	23	24	-	-
	GPC15	21	20	-	-
	GPC30	17	15	-	-
	GPC50	16	14	-	-
Liu et al. (2016)	GRAC-1	-	14.13	0.25	2124.89
	GRAC-2	-	11.03	0.22	2099.09
	GRAC-3	-	1.86	0.17	2081.84
	OPC-RAC	-	21.20	0.22	2082.74
Shi et al. (2012)	RC0	-	43.6	0.25	2536
	RC50	-	26.8	0.16	2444
	RC100	-	24.2	0.14	2353
	GRC0	-	37.7	0.22	2552
	GRC50	-	27.9	0.16	2451
	GRC100	-	21.0	0.15	2356
Xie et al. (2019)	S25-W0.5	12.3	-	0.21	-
	S25-W0.5	19.2	-	0.22	-
	S25-W0.5	23.1	-	0.23	-
	NC-W0.5	20.2	-	0.18	-
	RC-W0.5	15.6	-	0.17	-
Nuaklong et al. (2016) (NH concentration as variable)	8M	-	-	-	2160
	12M	-	-	-	2190
	16M	-	-	-	2210
Nuaklong et al. (2018) (Quantity of metakaolin as variable)	0 MK-C	-	-	-	2199
	10 MK-C	-	-	-	2195
	20 MK-C	-	-	-	2239
	30 MK-C	-	-	-	2196

Poisson's Ratio

The poisson's ratio enhanced with the fly ash and GGBS based geopolymer concrete with recycled aggregate (GRAC) and could be employed in construction (Liu et al., 2016; Xie et al., 2019). The Poisson's ratio of the concrete with 50% and 100% of recycled aggregate concrete, decreased about 38% and 44% than the conventional concrete (Shi et al., 2012; Xie et al., 2019). From Table 3, the water–binder ratio influence the Poisson's ratio. The poisson's ratio is reduced in the range of 12 to 23 percent as the w/b ratio increased in geopolymer concrete with recycled aggregate (GRAC) (Liu et al., 2016).

Density

The density of geopolymer concrete with recycled aggregate is found to be lower than that of conventional concrete with recycled aggregate concrete (Liu et al., 2016) as indicated in Table 3. Geopolymer concrete with crushed limestone as aggregate (GL) had density of about 2,390 kg/m^3, similar to the density of conventional concrete (2,400 kg/m^3), (Nuaklong et al., 2016). The unit weight of geopolymer concrete with metakaoline, is reduced up to 30% than the conventional concrete (Nuaklong et al., 2018). The densities of the geopolymer concrete with the recycled aggregate concrete (GRAC) showed marginal reduction of about 4% than the recycled aggregate concrete (RAC).

Durability Properties

Sorptivity

Sorptivity of the geopolymer concrete with recycled aggregate has been increased, as the cracks and fissures in the recycled concrete aggregate absorb the transit water (Shaikh, 2016). The adhered mortar of the masonry products on the recycled aggregate surface, increased the water absorption rate and made the concrete porous (Shaikh, 2016). 15% increase of recycled aggregate in concrete have better water uptake capability. The long-term performance of the geoplymerized concrete with recycled aggregate is discussed in Table 4.

Table 4. Durability Properties of Geopolymerized Concrete with Recycled Aggregate

References	Series	Sorptivity (mm/s^0.5)	Absorption (%)	Volume of permeable voids (%)
		28 days	28 days	28 days
Shaikh (2016)	GPC0	0.026	4.9	11.3
	GPC15	0.023	4.8	11.8
	GPC30	0.028	5.6	13.7
	GPC50	0.033	5.9	14.3
Nuaklong et al. (2018)	0 MK-L	38.2×10^{-3}	-	-
	10 MK-L	9.6×10^{-3}	-	-
	20 MK-L	8.4×10^{-3}	-	-
	30 MK-L	7.7×10^{-3}	-	-
	0 MK-C	67.8×10^{-3}	10.31	-
	10 MK-C	19.4×10^{-3}	5.31	-
	20 MK-C	10.6×10^{-3}	4.63	-
	30 MK-C	10.0×10^{-3}	4.58	-

The geopolymer concrete with recycled aggregate concrete (GRCA) always have good water intake behaviour (Nuaklong et al., 2016). The sorptivity is reduced with the metakaolin content, as the fine powdered metakaolin particles penetrate the existing cracks and voids, and strengthen the inter-transition zone of the recycled aggregate (Nuaklong et al., 2018).

Water Absorption

The water absorption rate is increased about 32% with 50% of the recycled aggregate concrete contents (Nuaklong et al., 2016; Shaikh, 2016). The density and porosity matrix of the geopolymer concrete with recycled aggregate concrete absorbed more water (Nuaklong et al., 2018) than the lime concrete as indicated in Figure 3.

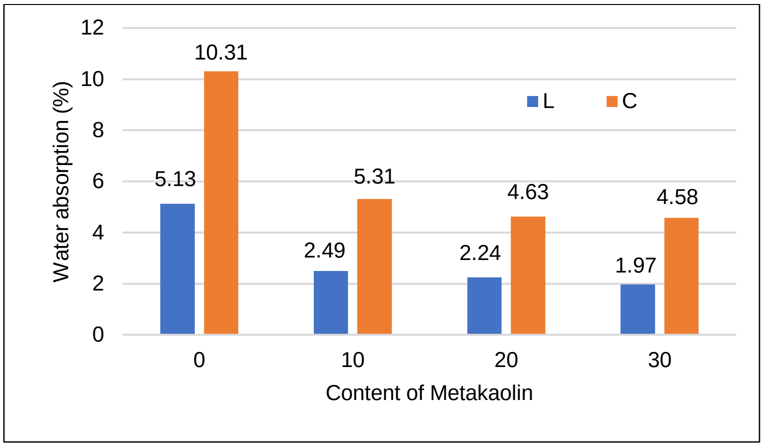

Figure 3. Water Absorption of Geopolymer Concrete with Metakaolin (Nuaklong et al., 2018)

The water absorption of geopolymer concrete with lime aggregate and recycled aggregate decreased with 8M, 12M and 16 Molarity of sodium hydroxide concentration as indicated in Figure 4.

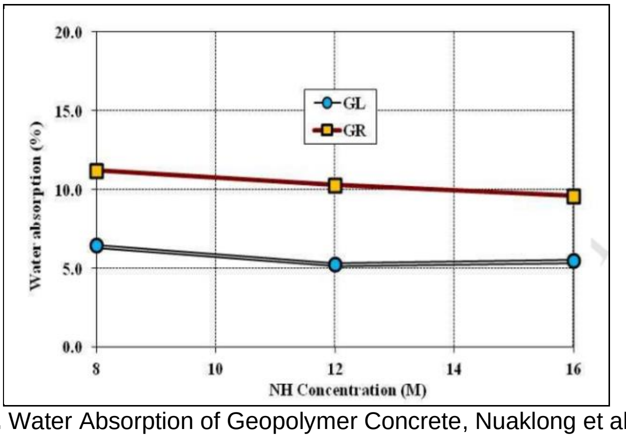

Figure 4. Water Absorption of Geopolymer Concrete, Nuaklong et al. (2016)

The volume of voids may also influence the water uptake behaviour. The water intake behaviour of geopolymer concrete with recycled aggregate (0%, 10%, 20%, 30%) reduced up to 23% than the geopolymer concrete with limestone (Koushkbaghi et al., 2019). The water transport properties were reduced with the enhancement of metakaolin quantity (Nuaklong et al., 2018).

Permeable Voids

Geopolymer concrete with 50% recycled aggregate concrete under steam cured has increased the volume of permeable voids by 22% (Shaikh, 2016) than conventional concrete. It was also reported that the geopolymer mixed with recycled concrete have better pore volume than the geopolymer concrete with limestone (Nuaklong et al., 2016). Generally, the recycled aggregate with mortar on its surface result in higher porosity than the limestone aggregate.

Chloride Ion Penetration

The geopolymer concrete with 10%, 20% and 30% of recycled concrete aggregate under steam cured is prone to the ion's infiltration (Shaikh, 2016) and the chloride ion penetration depth increased by 67%, 90% and 129% than that of an ordinary portland cement concrete as indicated in Figure 5.

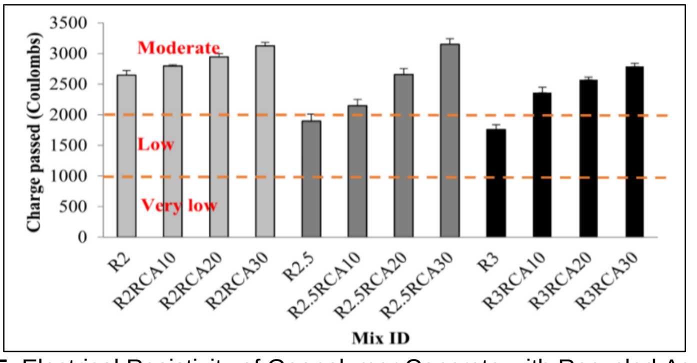

Figure 5. Electrical Resistivity of Geopolymer Concrete with Recycled Aggregate (as per ACI-222) Koushkbaghi et al. (2019)

Also, geopolymer with recycled concrete had higher chloride ion penetration compared with geopolymer concrete with limestone (Nuaklong et al., 2016). The movement of Cl^- ions found to be higher in the geopolymer recycled aggregate concrete (GRAC) because of the adhered mortar and the masonry content on the surface of the recycled aggregate (Nuaklong et al., 2018; Koushkbaghi et al., 2019). But the geocrete had higher chloride resistance as it has less pores and it also influence the long-term strength (Mugahed Amran et al., 2021).

Carbon Footprint

Carbon footprint is obtained across the supply chain, their environmental impact, their benefits and their wastes (Jerome Ignatius et al., 2022). Geopolymer concrete is a cement-less concrete and reduces 80% carbon footprint than the conventional Portland cement concrete (Akbari et al., 2013) as it reduces the cement production. In geopolymer concrete, one of the raw materials is obtained from the waste combustion (i.e.) flyash, rice husk ash, furnace slag etc., with 17% lesser CO_2 equivalent emissions than the conventional concrete (Kelly Cristiane, 2019). Hence, the geopolymer concrete with recycled aggregate concrete reduces the carbon footprint and minimizes the environmental pollution.

CONCLUSION AND RECOMMENDATION

From the published data, the geopolymer concrete with recycled aggregate (GRAC) is a better and booming option in construction industry. The geopolymer based concrete reduces 80% carbon footprint into the environment than the cement concrete production. The fly ash and GGBS based geopolymerized concrete can enhance the strength properties of geopolymer concrete with recycled aggregate. 12 M NaOH concentration can yield better compressive strength for geopolymer concrete. The durability property of geopolymer concrete can be improved with the presence of required amount of metakaolin. Porosity and Cl^- penetration can also be controlled with the recycled aggregate content in geopolymer concrete. Further investigations are required on additives especially nanocomposite materials that may enhance the mechanical and durability characteristics of geopolymer recycled aggregate concrete.

REFERENCES

Abdelaziz Hasnaoui, Elhem Ghorbel, George Wardeh (2021), Performance of metakaolin/slag-based geopolymer concrete made with recycled fine and coarse aggregates, *Journal of Building Engineering*, Vol 42: 102813

ACI 222.3R-11, (2011), Guide to Design and Construction Practices to Mitigate Corrosion of Reinforcement in Concrete Structures, *American Concrete Institute*.

Ahmad L.Almutairia Bassam A.Tayehb Adeyemi Adesinac Haytham F.Isleemd Abdullah M.Zeyad, Potential applications of geopolymer concrete in construction: A review, *Case Studies in Construction Materials*, Vol 15: pp -e00733

Akbari H, Heller T, Shin S,Yang X, Kolay P, Kumar S and. Mohanty M.K (2013), "Geopolymer-based concrete to reduce carbon footprint of the construction industry", *Mining Engineering*, 65 (12): 57-62

Bakri, A.M.M.A., Kamarudin H., Bnhussain M., Khairul Nizar I. & Mastura W. (2011) Mechanism and Chemical Reaction of Fly Ash Geopolymer Cement-A Review. *Asian Journal of Scientific Research*, 1(5), 247-253.

Cong, P. & Cheng, Y. (2021) Advances in Geopolymer Materials: A Comprehensive Review. *Journal of Traffic and Transportation Engineering*, 8 (3): 283-314.

Davidovits, J. (1993) Geopolymer Cements to Minimize Carbon- Dioxide Greenhouse-Warming. *Ceramic Transactions*, 37(1): 165-182.

Djwantoro Hardjito, Steenie E. Wallah, Dody M. J. Sumajouw, and B.Vijaya Rangan (2004), On the Development of Fly Ash Based Geopolymer Concrete, *ACI Materials Journal*, vol 101-M52: 467 - 472

Duxson P., Mallicoat S.W., Lukey G.C., Kriven W.M., & van Deventer J.S.J. (2007) The Effect of Alkali and Si/Al Ratio on the Development of Mechanical Properties of Metakaolin-Based Geopolymers. *Colloids and Surfaces A: Physicochemical and Engineering Aspects*, 292 (1): 8-20.

Duxson P., Provis, J.L., Lukey, G.C., & van Deventer J.S.J. (2007) The Role of Inorganic Polymer Technology in the Development of 'Green Concrete'. *Cement and Concrete Research*, 37(12):1590-1597.

Duxson, P., Fernández-Jiménez, A., Provis, J.L., Lukey, G.C., Palomo A., & van Deventer J.S.J. (2007) Geopolymer Technology: The Current State of the Art. *Journal of Materials Science*, 42: 2917-2933.

Gartner, E. (2004) Industrially Interesting Approaches to Low-CO_2 Cements. *Cement and Concrete Research*, 34 (9): 1489–1498.

Herwani, Ivindra Pane, Iswandi Imran, and Bambang Budiono (2018), Compressive Strength of Fly ash-based Geopolymer Concrete with a Variable of Sodium Hydroxide (NaOH) Solution Molarity, *MATEC Web of Conferences*, vol 147: 01004

Jerome Ignatius, Garcesa Arnel T, Beltrana B, Raymond R. Tana Jason Maximino C.Ongpengb Michael Angelo B.Promentilla (2022), Carbon footprint of self-healing geopolymer concrete with variable mix model, *Cleaner Chemical Engineering*, Vol 2: 100027

Kelly Cristiane, GomesMonica CarvalhoDaniel de Paula DinizRafael de Carvalho Costa AbrantesMichel Alves BrancoPaulo Roberto Oliveira de Carvalho Junior (2019), Carbon emissions associated with two types of foundations: CP-II Portland cement-based composite vs. geopolymer concrete, *Revista Materia*, Vol. 24 (4): e-12525

Koushkbaghi, M., Alipour, P., Tahmouresi, B., Mohseni, E., Saradar, A., & Sarker, P. K. (2019) Influence of Different Monomer Ratios and Recycled Concrete Aggregate on Mechanical Properties and Durability of Geopolymer Concretes. *Construction and Building Materials*, 205:519–528.

Liu Z., Cai C.S., Peng H., & Fan F. (2016) Experimental Study of the Geopolymeric Recycled Aggregate Concrete. *Journal of Materials in Civil Engineering*, 28 (9): 1- 9.

Malayali, A.B., Chokkalingam, R.B., & Muthukannan, M. (2022) Strength Properties of Geopolymer Concrete Modified with Recycled Aggregates. *Iranian Journal of Science and Technology, Transactions of Civil Engineering*, 46: 77–89

Meor Ahmad Faris, Mohd Mustafa Al Bakri Abdullah, Ratnasamy Muniandy, Shamala Ramasamy, Mohammad Firdaus Abu Hashim, Subaer Junaedi, Andrei Victor Sandu, Muhammad Faheem Mohd Tahir (2022), Review on Mechanical Properties of Metakaolin Geopolymer Concrete by Inclusion of Steel Fibers, *Archieves of Metallurgy and Materials*, Vol 67 1, pp 261-267

Meyer, C. (2009) The Greening of the Concrete Industry. *Cement and Concrete Composites*, 31 (8):601-605.

Mugahed Amran, AminAl Fakih, S.H. Chu, Roman, Fediuk, Sani Haruna, Afonso Azevedo, Nikolai Vatin, (2021) Long-term durability properties of geopolymer concrete: An in-depth review, *Case Studies in Construction Materials*, Volume 15: e00661

Nergis, N. D.D., Abdullah, M.M.A.B., & Tahir, M.F.M. (2018) Geopolymers and Their Uses: Review. *IOP Conf. Series: Materials Science and Engineering*, 374: 012019

Nuaklong, P., Sata, V., & Chindaprasirt, P. (2016) Influence of Recycled Aggregate on Fly Ash Geopolymer Concrete Properties. *Journal of Cleaner Production*, 112(4):2300-2307.

Nuaklong, P., Sata, V., & Chindaprasirt, P. (2018) Properties of Metakaolin-High Calcium Fly Ash Geopolymer Concrete Containing Recycled Aggregate from Crushed Concrete Specimens. *Construction and Building Materials*, 161:365-373.

Nuruddin M F, Malkawi A B, Fauzi A, Mohammed B S, Almattarneh H M. (2016), Geopolymer concrete for structural use: Recent findings and limitations, IOP Conference Series: Materials Science and Engineering, vol 133: 1 – 9

Rangan B.V. (2008), Studies on Fly Ash-Based Geopolymer Concrete, *Malaysian Construction Research Journal*, Vol. 3: 1 - 20

Rao, M.C., Bhattacharyya S.K., & Barai, S.V. (2011) Influence of Field Recycled Coarse Aggregate on Properties of Concrete. *Materials and Structures*, 44:205-220.

Rao, P.K. (2000) Sustainable Development: Economics and Policy, Malden MA, USA: Blackwell Publishers Inc.

Ridzuan A. R. M., Abdullah M.M.A.B., Arshad M. F., Tahir M. F. M. & Khairulniza, A. A. (2014) The Effect of NaOH Concentration and Curing Condition to the Strength and Shrinkage Performance of Recycled Geopolymer Concrete. *Materials Science Forum*, vol 803: 194-200.

Serina, N.G. & Engelsen, C.J. (2018) Construction and Demolition Wastes, Waste and Supplementary Cementitious Materials in Concrete, *Woodhead Publishing Series in Civil and Structural Engineering*, AECOM Report: 229-255.

Shaikh F.U.A., Than A.B., Odoh H. (2015) Effect of Nano Silica on Properties of Concrete Containing Recycled Coarse Aggregates. *Proceedings of the Institution of Civil Engineers – Construction Materials*, 168 (2): 68-75.

Shaikh, F.U.A. (2016) Mechanical and Durability Properties of Fly Ash Geopolymer Concrete Containing Recycled Coarse Aggregates. *International Journal of Sustainable Built Environment*, 5 (2): 277-287

Shi X. S., Collins F. G., Zhao X. L., & Wang Q. Y. (2012) Mechanical Properties and Microstructure Analysis of Fly Ash Geopolymeric Recycled Concrete. *Journal of Hazardous Materials*, 237-238:20-29

Singh B, Ishwarya G.M, Gupta S.K., Bhattacharyya. (2015), Geopolymer concrete: A review of some recent developments, *Construction and Building Materials*, vol 85: 78–90

Srinivasan, K. & Sivakumar, A. (2013) Geopolymer Binders: A Need for Future Concrete Construction. *International Scholarly Research Notices* - *ISRN Polymer Science*, pp 1 – 8

Thomas, B.S., Yang, J., A. Bahurudeen, Chinnud, S.N., Abdalla, J.A., & Hawileh, R.A. (2022) Geopolymer Concrete Incorporating Recycled Aggregates: A Comprehensive Review. *Cleaner Materials*, 3:100056

Vaishnavi Devi, Gausikan Ravichandran, S. Chithambaranathan, J. Wilfred Jeffrey (2021), Utilization of recycled aggregate of construction and demolition waste as a sustainable material, *Materials Today: Proceedings*, Volume 45, Part 7: Pages 6649-6654

Xie J., Wang J., Rao R., Wang C. & Fang C. (2019) Effects of Combined Usage of GGBS and Fly Ash on Workability and Mechanical Properties of Alkali Activated Geopolymer Concrete With Recycled Aggregate. *Composites Part B: Engineering*, 164:179-190.

Xie, J., Wang J., Zhang B., Fang C. & Li L. (2019) Physicochemical Properties of Alkali Activated GGBS and Fly Ash Geopolymeric Recycled Concrete. *Construction and Building Materials*, 204:384-398.

Xu, H. & Deventer, J. S. J.V., (2000) The Geopolymerisation of Alumino-Silicate Minerals. *International Journal of Mineral Processing*, 59:247-266.

Yun-Ming, L., Cheng-Yong,H., Bakri, M.M.A. & Hussin, K. (2016) Structure and Properties of Clay-Based Geopolymer Cements: A Review. *Progress in Materials Science*, 83:595-629.

Živica, V., Palou, M.T., & Križma, M. (2014) Geopolymer Cements and Their Properties: A Review. *Building Research Journal*, 61(2): 85-100

INTEGRATED ENVIRONMENTAL SOLUTIONS-VIRTUAL ENVIRONMENT (IES-VE) SOFTWARE ACCURACY VALIDATION ON NATURALLY VENTILATED ROYAL MALAYSIAN POLICE (RMP) LOCKUP'S THERMAL PERFORMANCE SIMULATION

Bismiazan Abd. Razak[1,2*], Mohd. Farid Mohamed[1], Wardah Fatimah Mohammad Yusoff[1] and Mohd. Khairul Azhar Mat Sulaiman[1]
[1]Faculty of Engineering and Built Environment, Universiti Kebangsaan Malaysia (UKM), Bangi, Selangor Darul Ehsan, Malaysia.
[2]Architecture Branch of the Public Works Department, IPJKR Malaysia, Tingkat 11, Menara Tun Ismail Mohamed Ali (TIMA), Jalan Raja Laut, Kuala Lumpur.

Abstract
Along with the rapid emerging technology and research diversification, especially on the building performance simulation program, there are various programs that have been introduced by program developers, researchers and academicians in ensuring data accuracy. Correspondingly, the Integrated Environmental Solutions-Virtual Environment (IES-VE) is one of the simulation programs that is usually being used for a building performance simulation study. However, the IES-VE performance on data accuracy has often been debated and has been compared to other engineering simulation programs. Therefore, the objective of this study is to verify IES-VE reading accuracy by comparing on-site physical measurements with IES-VE simulation result using a naturally ventilated Royal Malaysia Police (RMP) lockup cell with an area of 9.0 m2 as the case study room. Using the air temperature, mean radiation temperature, and relative humidity as the thermal comfort factors and the operative temperature as a thermal comfort index, three sets of Delta Ohm HD32.3 WBGT-PMV (internal parameters) and one set of Seven Elements Integrated Weather Sensor WTS700 (external parameters) had also been used as measurement instruments. The results show that the range of percentage differences between physical measurement and the simulation is from -11.39% to 8.67%), which support the previous studies on IES-VE data accuracy percentage difference which is below 20% and the simulated data that are considered as accurate and valid for thermal performance for the targeted building.

Keywords: *IES-VE; Simulation; Thermal Performance; RMP Lockup.*

INTRODUCTION

Building performance simulation programs are often used by researchers as an alternative in validating reading data that have been obtained from field studies (Leng et al., 2012), evaluating the performance of thermal comfort (Nur 'aini, 2017), energy consumption rates and building performance (Cho et al., 2012; Nguyen et al., 2014), they are also an initiative towards energy efficient, cost effective, and sustainable building design (Ji et al., 2009). Since the 1960s, building performance simulation programs have been developed to analyse building energy consumption and are further extended to assess the dynamic thermal behaviour of buildings from brief use to complex levels (Ahmad & Szokolay, 1994). The use of the simulation program was also detected around the same year by the United States of America (USA) government who had been involved in a collapsed shelter project through the assessment of the thermal environment (Attia et al., 2009). Crawley et al. (2008) has stated that over the past 50 years, hundreds of building energy simulation programs have been developed, improved and used as indicators of building performance including its energy consumption and demand, temperature and humidity measurements as well as costs.

Building performance simulation programs are also used to determine passive systems performance of buildings with natural and hybrid ventilation as well as in optimising operating time in producing innovative and sustainable building designs (Ji et al., 2009). Apart from evaluating and analysing the performance of energy consumption, simulation programs are also used by researchers in evaluating the performance of daytime lighting and natural ventilation based on the variety of building light well designs (Ahadi et al., 2018). In recent years, the building performance simulation program has achieved a high level of maturity through the production of various programs and models that can assess building performance diversity (Attia et al., 2012). Overall, the simulation program is very important to the designers, especially to the architects, in helping to provide some alternative steps towards solving design problems in order to maximise the performance of the building.

The selected case study lockup for this validation process is one of the RMP lockup cells that have been identified to have poor ventilation system and an insufficient opening size which cause thermal discomfort to the detainees such as hot indoor environmental conditions (Abd. Razak et al., 2020; SUHAKAM, 2016). The study is purposely conducted on the RMP lockup cell since very few studies are related to thermal comfort and natural ventilation and are rarely conducted on this type of building or equivalent.

LITERATURE REVIEW

Constraints on the Existing Building Performance Simulation Programs

The development of computer technology and the world of research on the construction industry has triggered the invention of simulation programs that suit the needs of research irrespective of the field of study, professional background, expertise and industry. Rapid changes in technology and the increasing needs have caused the evolution of Building Performance Simulation (BPS) such as ECOTECT, EnergyPlus, IES-VE, TRNSYS, ANSYS and many more which are being used for data validation.

Although various improvements to the existing building performance simulation programs on the market have been made by program developers, researchers, professionals and the academia, there are still unresolved constraints. For example, there is still no ready-to-use simulation programs for the architects to analyse buildings and comfort performance in hot climate environments. The inability of some programs to support and assist the design process at an early stage is also among the constraints that have been identified (Attia et al., 2012).

According to Anand et al. (2017), 132 building performance simulation programs have been listed by the U.S. Department of Energy (US DOE) website and of that number, only about 42 programs can be used for energy simulations on buildings. According to Attia et al. (2012) most simulation programs in the current market are not user friendly, not comprehensive and produce inaccurate thermal comfort results based on the design environment and potential, with a passive or active approach that is to be used by architects in the early stages of design. She has also added that out of the 392 BPS that are listed on the DOE website in 2011, less than 40 programs have been developed for the architects use in the early stage of design.

Integrated Environmental Solution-Virtual Environment (IES-VE)

An online survey by Attia et al. (2009) has been conducted and participated by 249 respondents to understand the difference of 10 major simulation programs that are available in the market, such as ECOTECT, HEED, Energy 10, Design Builder, eQUEST, DOE-2, Green Building Studio, IES VE, Energy Plus and Energy Plus-SketchUp Plugin (OpenStudio). The purpose is to identify an appropriate program that is to be used by architects from an architectural point of view in analysing the building performance from the early stage of a building design. This is because most of the existing programs do not meet an Architectural requirement, working methods, complexity, and they are cumbersome and difficult to operate even with simple tools. The analysis was made based on two main aspects that are often prioritised by architects in the selection of simulation programs. Firstly, usability and information management, and secondly integration of intelligent design that is knowledge based. Apart from these two aspects, the handling of building modelling, the accuracy of the program and the ability to perform complex and detailed simulations of building components are also highly prioritised by architects. Based on the survey by Attia et al. (2009), three main programs are identified to be the suitable choices for architects use, especially for building simulation. They are IES-VE (85%), followed by HEED (82%) and eQuest (77%). The IES-VE was rated based on its user-friendly graphics and template-driven approach which are comprehensive and beneficial compared to the other programs which usually use text as the outcome. The IES-VE is also certified by Attia et al. (2009) as an easy program to operate and very helpful in supporting analytical advances towards thermal performance simulations which in producing rapid results for the initial design stage and detailed analysis for the later stage.

The above statements are also supported by Leng et al. (2012) through simulations of studies conducted using the IES-VE program to see the accuracy of the program through comparison with data recorded from field studies. In this study, test room was used for physical measurements with the HOBOware U-1 instrument to measure the air temperature and relative humidity of the room. The results of this field study were then verified with air temperature and relative humidity readings analysed through IES-VE simulations. The comparison between the field study results and simulation showed a very small difference which ranged from 6.99% to 13.62% for air temperature and 0.002% to 14.90% for relative humidity. Based on the previous study that has been conducted by Maamari et al. (2006), the differences between the field measurement and simulation that range from 10% to 20% is acceptable which indirectly indicate that the IES-VE usage is reliable. The study shows that the IES-VE is among the programs that have high accuracy, flexibility and is valid for the simulation of building thermal performance.

In addition, according to Zaki et al. (2012), various justifications have been expressed by previous researchers regarding the ability of the IES-VE program in the implementation of simulations on building performance as an internationally verified program for the purpose of thermal and visual comfort simulation. Notably, equip with a database designed based on ASHRAE Mohammadi et al. (2010) assist designers especially architects in solving environmental problems and building criteria through the variety of applications that have been offered by Leng et al. (2012), simulation capabilities of airflow and heat transfer Almhafdy et al. (2015), capable of predicting accurate results Ibiyeye et al. (2015) and provide an environmental environment in a detailed design evaluation of a building for the purpose of optimising comfort and energy consumption criteria Lau et al. (2016). IES-VE is also capable of producing air temperature, mean radiant temperature and relative humidity readings results through ApacheSim application which is very much in line with this study where the results are much needed in comfortable temperature setting based on previously selected equations (IES-VE, 2020).

The Integrated Environmental Solutions-Virtual Environment (IES-VE) is known as one of the recommended programs for building performance simulation study. A lot of previous studies have shown that the IES-VE simulation results are acceptable if the percentage differences between the field measurement and simulation results are within 0% to 20%. This statement has also been supported by experts in previous studies namely by Leng et al. (2012) and Qays Oleiwi et al. (2019), that have been conducted in the hot and humid climate of Malaysia. The first study is more focused on the study of software validation for one room using air temperature and relative humidity only, while the second study is more on validation for three rooms using three thermal comfort parameters which are air temperature, mean radiant temperature and relative humidity. Hence, the current study has been conducted on a naturally ventilated RMP lockup cell as the targeted room in order to be more comprehensive and to support the expert's agreement on the IES-VE data accuracy by comparing on-site physical measurements with IES-VE simulation result using four parameters, i.e., air temperature, mean radiation temperature, relative humidity as the thermal comfort factors, and the operative temperature as a thermal comfort index. Also, three sets of Delta Ohm HD32.3 WBGT-PMV (internal parameters) and one set of Seven Elements Integrated Weather Sensor WTS700 (external parameters) have been used as a measurement instrument based on the Class 1 field measurement protocol which has never been implemented by any previous studies.

METHODOLOGY

To achieve the objectives of this study, two procedures have been set, they are the field measurement and the building performance simulation, using the IES-VE software. The results from these two procedures were then compared to see the effectiveness of the IES-VE.

Case Study Room (RMP Lockup Cell)

Figure 1 shows the selected lockup, which is located in Alor Gajah District Police Headquarters, Malacca (2°38′00″ N 102°21′00″ E).

With an area of 9.0 m^2 (3.0 m (W) x 3.0 m (L) x 4.2 m (H)) as shown in Figure 2, the lockup cell has been constructed to accommodate one to three detainees at a time. The lockup cell is on the ground floor of a two-storey building and is equipped with a window opening of 0.6 m (W) x 0.6 m (H) facing south, which is parallel to the direction of the surrounding wind. The design of the existing window is in iron grilles which is conform with the design standards for a lockup cell, as shown in Figure 3a. However, the existing window only offers a 4% ventilation opening which is insufficient as stipulated by the Law of Malaysia (Act 133) (Uniform Building By Law 1986 (Ammendment 2012), 2012) the minimum ventilation opening should be from 10% to 15% of the floor area.

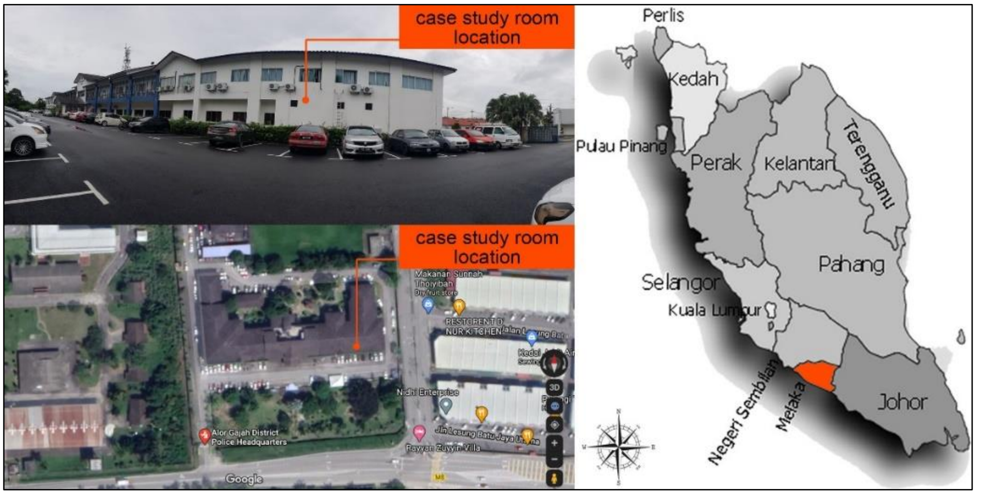

Figure 1. Case Study Room Location (RMP Lockup Cell)

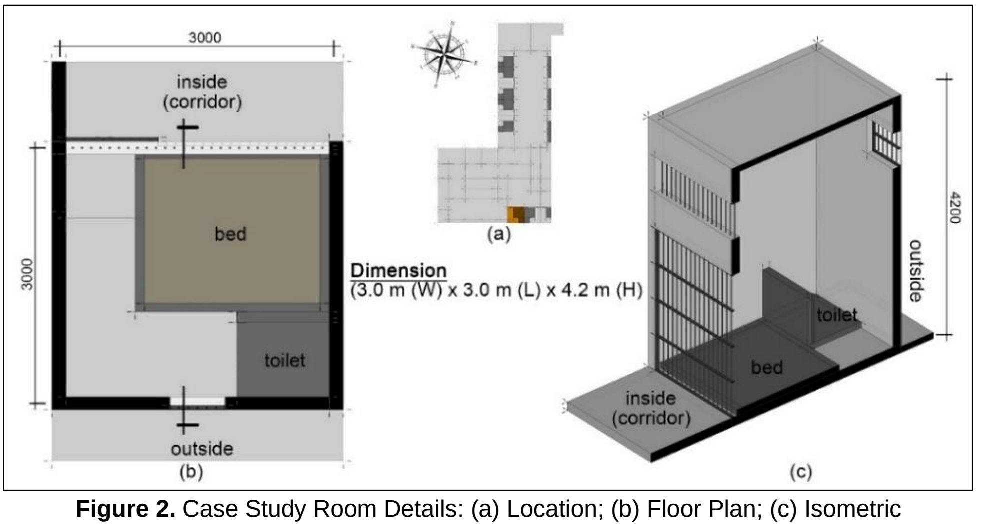

Figure 2. Case Study Room Details: (a) Location; (b) Floor Plan; (c) Isometric

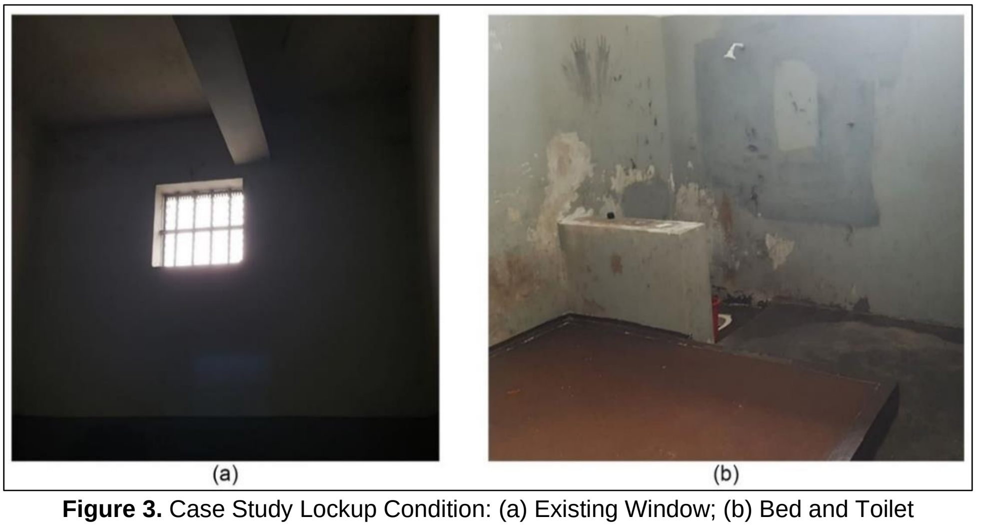

Figure 3. Case Study Lockup Condition: (a) Existing Window; (b) Bed and Toilet

The lockup cell consists of a bed and a toilet as shown in Figure 3b. In general, the external walls are constructed using reinforced concrete with weatherproof paint finishing. While the internal lockup cell walls are constructed using industrialised building system concrete panel with emulsion paint finishing. The floor is made from reinforced concrete with floor hardener finishing while the ceiling is painted with emulsion paint. The finishing that is used for the toilet walls and floor is epoxy paint. For the bed area, the building material is reinforced concrete at 150 mm heights, complete with tongue and groove plank finishes. The bed and toilet are separated by a 1200 mm height partition wall to provide a bit of privacy to the detainees.

Field Measurement Procedure

Based on the Class 1 field measurement protocol, three sets of Delta Ohm HD32.3 WBGT-PMV (internal parameters) with different height above the floor level (Abd. Razak et al., 2020; Maarof, 2014) and one set of Seven Elements Integrated Weather Sensor WTS700 (external parameters) which comply with ISO 7726 requirement (ASHRAE 55, 2017) were used as a measurement instrument. The three Delta Ohm instruments were placed in the middle of the lockup cells bed with a height of 0.6 m above the floor for D1, 1.1 m above the floor for D2 and 3.2 m above the floor for D3, as shown in Figure 4. D3 was placed at a position 1.0 m inward from the centre of the existing window. The data that were obtained from these three Delta Ohm were analysed using DeltaLog10 software. For W700, the location of the instrument was in the open area outside the building without wind flow obstruction with a height of 1.8 m above the ground. It was used to record readings of the external environment of the study area. The data obtained from the W700 were then be analysed using DLG Master software. All instruments used in this field measurement have been calibrated in advance to obtain accurate and precise data.

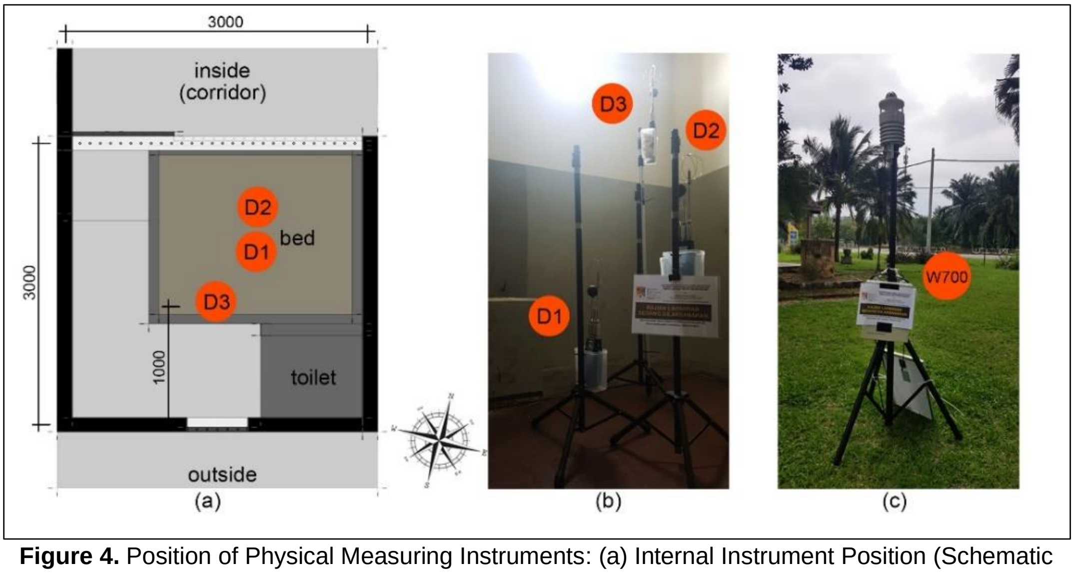

Figure 4. Position of Physical Measuring Instruments: (a) Internal Instrument Position (Schematic Floor Plan); (b) Delta Ohm HD32.3 WBGT-PMV; (c) Seven Elements Integrated Weather Sensor WTS700

Simulation Procedure

The simulation procedure started with the development of a case study room model using Sketchup Pro 2018 software. The case study room labelling was set in Sketchup Pro 2018 software with the Confinement Cells Police Station. The completed model was then exported into the IES-VE [ModelIT] program for the purpose of setting up the orientation of the case study room. The location of the case study room was then made in the IES-VE [ApLocate] program. The Design Weather Data set was based on Malaysia Standard (MS 1525:2014, 2014) with a temperature of 33.3 °C for dry bulb temperature and 27.2 °C for wet bulb temperature. Determination of the model case study room building materials and simulation duration was made through the Building Template Manager IES-VE [ModelIT and Apache] just like the actual lockup cell, as shown in Figure 5 and Table 1. Since the selected case study room was using natural ventilation with open ventilation at all times, the window openings were fixed using IES-VE [MacroFlo] as per actual condition. The whole model was then simulated using IES-VE [ApacheSim] to obtain the required reading data such as air temperature (Ta), relative humidity (RH), mean radiant temperature (Tr) and operative temperature (To) from IES-VE [VistPro].

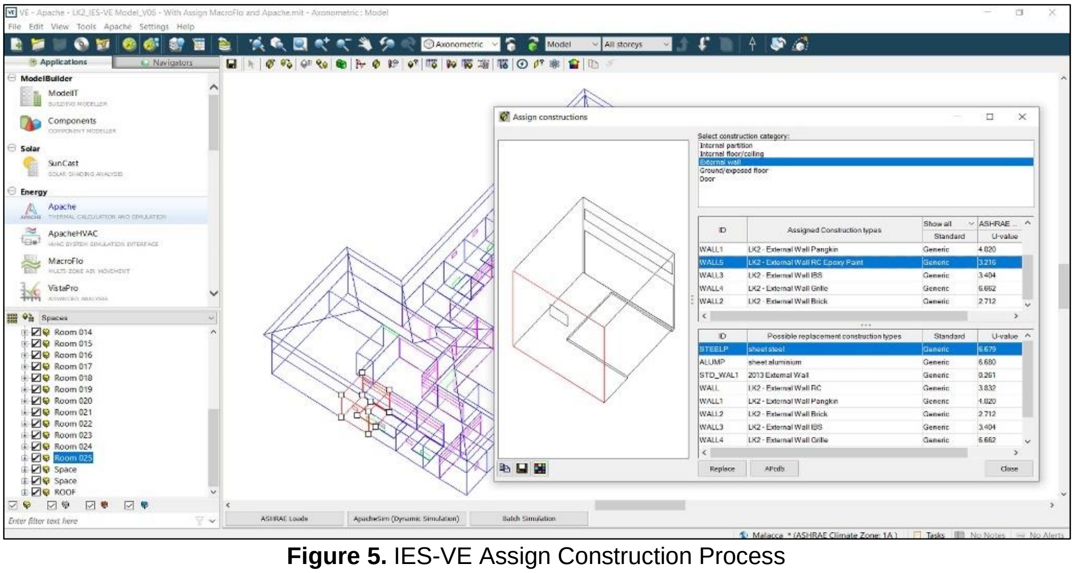

Figure 5. IES-VE Assign Construction Process

Table 1. Assign Project Construction

Category	Construction	Thickness (mm)	U-Value (W/m^2-K)
External wall	Reinforced concrete c/w cement plaster and rendering	150	3.8322
Internal partition	Cast concrete (IBS) c/w cement plaster	150	2.6071
Exposed floor	Reinforced concrete c/w screed	150	3.5853
Internal ceiling	Reinforced concrete c/w cement plaster and screed	150	2.9861
Door and internal grille panel	Iron grille	20	6.6625
Window	Iron grille c/w expanded metal	25	6.6620
Bed	Reinforced concrete c/w gravel and hard wood on top (tongue and groove)	150	1.9964

Research Limitation

The case study room selected for the purpose of this study was a lockup cell with natural ventilation. Although there were wall fans and exhaust fans in some lockup cell areas, they were turned off throughout the study period. The lockup cell was also left empty without detainees in order to obtain a default reading. The field measurement was carried out in five days, 24 hours a day starting from 27th. July to 1st. August 2020 where during this period, Malaysia experienced high average daily temperature from 31.2 °C to 33.2 °C due to monsoon changes (Jabatan Meteorologi Malaysia, 2020; World Meteorological Organisation, 2020). One hour a day was allocated for data collection measurement and instrument reset. During this period, three thermal comfort factors including air temperature (Ta), relative humidity (RH) and mean radiant temperature (Tr) and a thermal comfort index of operative temperature (To) were measured and analysed. All settings implemented on the field measurements were also set in the IES-VE program as close as possible to obtain accurate variance data. However, for weather data setting, Kuala Lumpur has been chosen as the location since there are no weather data for Malacca that is available in the IES-VE, and Kuala Lumpur is the nearest equivalent. The log interval that has been set for each data reading for the field measurement and simulation is 10 minutes.

RESULTS AND DISCUSSION

The data reading results that were obtained from the field measurement and IES-VE simulation were analysed and compared to see the percentage differences in accuracy and precision. Equation (1) was used as recommended by Leng et al. (2012) and Qays Oleiwi et al. (2019) in order to calculate the reading results.

$$PD = [(SM - FM) / FM] \, x \, 100 \qquad (1)$$

Where

PD = Percentage different
SM = Simulation measurement
FM = Field measurement

Maamari et al. (2006) in their previous studies had recommended that the adopted percentage difference between the field measurement and simulation program to be from 10% to 20%. This statement has also been supported through a validation study of the difference in accuracy between the field measurement and simulation programs that have been implemented by Leng et al. (2012) with the obtained percentage of difference from 0% to 15% for the studies involving air temperature and relative humidity, while Qays Oleiwi et al. (2019) have obtained a percentage from 0% to 20% for the studies involving air temperature, relative humidity and mean radiant temperature. For this study, the benchmarks that were recommended by all the three studies were used by setting the maximum accuracy difference between the field measurement and IES-VE simulation program, with not more than or equal to 20% in order to ensure the suitability and reliability of the IES-VE software for this study and in the future.

Figure 6 and Table 2 show the comparison of average air temperature differences between the field measurement and simulation for a five-day duration. The average air temperature readings that were recorded during the five days of field measurements for instruments D1-D3 ranged from 27.97 °C to 28.19 °C, while the readings produced by the IES-VE simulations over the same period were 28.77 °C. The percentage differences that were recorded for the average air temperature between the field measurements and simulations ranged from 2.06% to 2.86%. The readings for the maximum air temperature that were recorded for the field measurements were from 28.35 °C to 28.53 °C, while the readings produced from the IES-VE simulations were 29.74 °C. The percentage differences that were recorded for the maximum air temperature between field measurements and simulations ranged from 4.24% to 4.90%. For the minimum air temperature readings, the that were readings recorded from the field measurements were from 27.59 °C to 27.85 °C, while the readings produced from the IES-VE simulations were 27.73 °C. The percentage difference that was produced for the minimum air temperature was from -0.43% to 0.51%. The range of percentage differences that was recorded for air temperatures was below 20% and thus considered reliable and acceptable as recommended by previous studies and established benchmarks.

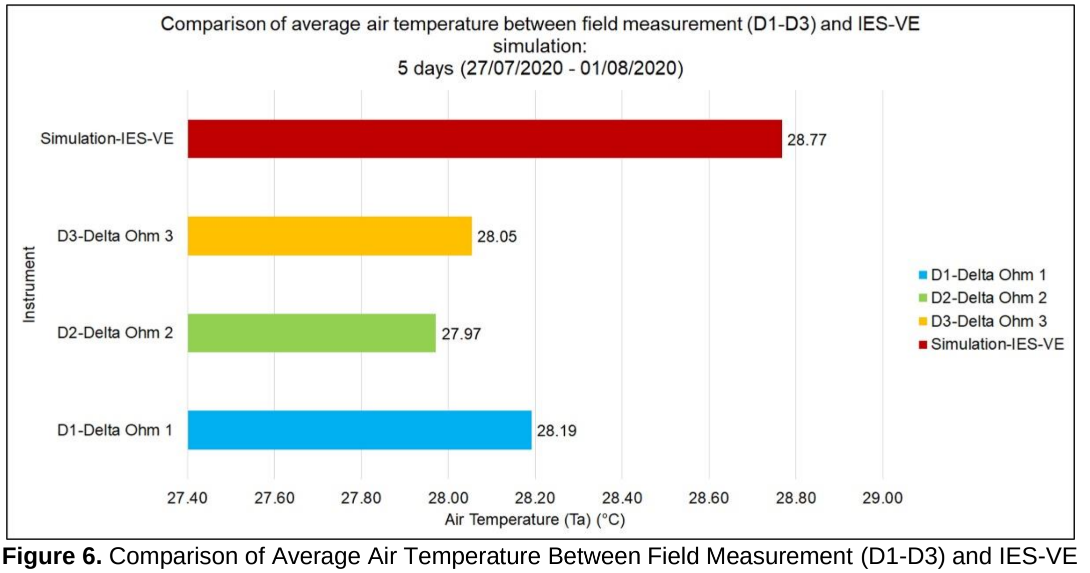

Figure 6. Comparison of Average Air Temperature Between Field Measurement (D1-D3) and IES-VE Simulation

Table 2. Comparison of Average Percentage Differences of Air Temperature Between Field Measurement and IES-VE Simulation for Five Days

	Instrument Delta Ohm (F0ield Measurement) (°C)				**Simulation IES-VE (°C)**	**Percentage Differences (%)**		
	D1	**D2**	**D3**	**W700**		**D1**	**D2**	**D3**
Average	28.19	27.97	28.05	26.02	28.77	2.06%	2.86%	2.57%
Maximum	28.53	28.40	28.35	30.70	29.74	4.24%	4.72%	4.90%
Minimum	27.85	27.60	27.59	23.44	27.73	-0.43%	0.47%	0.51%

D = Delta Ohm HD32.3 WBGT-PMV; W700 = Seven Elements Integrated Weather Sensor WTS700

Figure 7 and Table 3 show the comparison of average relative humidity differences between the field measurement and simulation for a five-day duration. The average relative humidity readings that were recorded during the five days of field measurements for instruments D1-D3 ranged from 79.05% to 82.57%, while the readings produced by the IES-VE simulations over the same period were 74.21%. The percentage differences that were recorded for the average air temperature between field measurements and simulations ranged from -10.12% to -6.12%. The readings for the maximum relative humidity that were recorded for field measurements were between 81.78% to 87.56%, while the readings produced from the IES-VE simulations were 77.59%. The percentage differences recorded for the maximum air temperature between the field measurements and simulations ranged from -11.39% to -5.12%. For the minimum relative humidity readings, the readings that were recorded from the field measurements were from 75.90% to 77.44%, while the readings produced from the IES-VE simulations were 69.86%. The percentage difference that was produced for the minimum air temperature was from -11.39% to -5.12%. The negative readings might be influenced by the window opening which then caused bad internal air circulation. However, the readings were acceptable if they were below 20% as recommended by previous studies and established benchmarks.

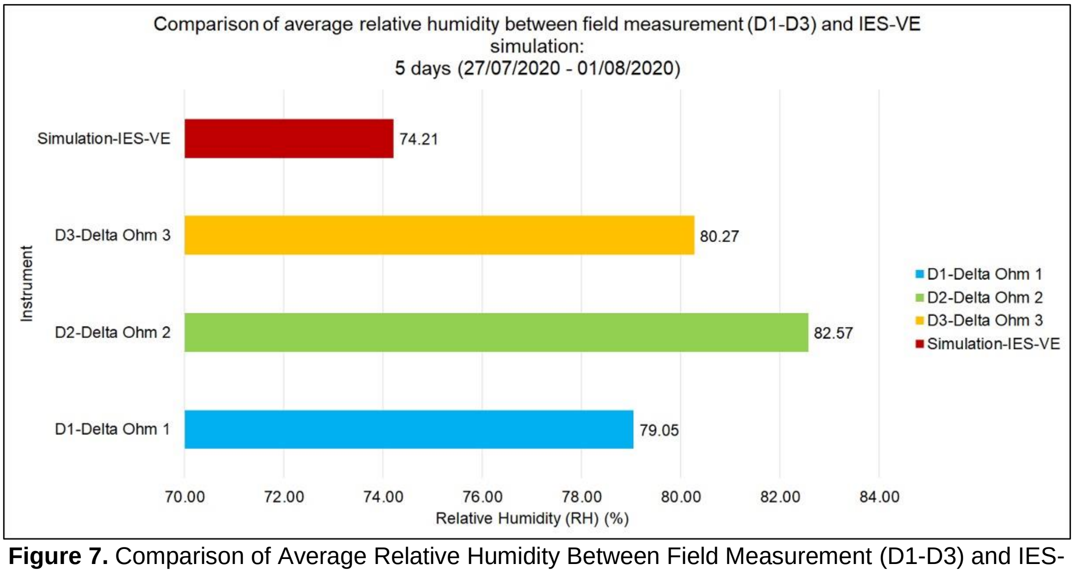

Figure 7. Comparison of Average Relative Humidity Between Field Measurement (D1-D3) and IES-VE Simulation

Table 3. Comparison of Average Percentage Differences of Relative Humidity Between Field Measurement and IES-VE Simulation for Five Days

	Instrument Delta Ohm (Field Measurement) (%)				Simulation IES-VE (%)	Percentage Differences (%)		
	D1	**D2**	**D3**	**W700**		**D1**	**D2**	**D3**
Average	79.05	82.57	80.27	88.44	74.21	-6.12%	-10.12%	-7.55%
Maximum	81.78	87.56	83.25	98.42	77.59	-5.12%	-11.39%	-6.80%
Minimum	75.90	77.44	77.15	69.52	69.86	-7.96%	-9.79%	-9.45%

D = Delta Ohm HD32.3 WBGT-PMV; W700 = Seven Elements Integrated Weather Sensor WTS700

Figure 8 and Table 4 show the comparison of average mean radiant temperature differences between the field measurement and simulation for a five-day duration. The average means radiant temperature readings that were recorded during the five days of field measurements for instruments D1-D3 ranged from 27.58 °C to 27.75 °C, while the readings produced by the IES-VE simulations over the same period were 28.80 °C. The percentage differences that were recorded for the average mean radiant temperature between the field measurements and simulations ranged from 3.78% to 4.42%. The readings for the maximum mean radiant temperature that were recorded for the field measurements were from 27.87 °C to 28.08 °C, while the readings produced from the IES-VE simulations were 29.68 °C. The percentage differences that were recorded for the maximum mean radiant temperature between the field measurements and simulations ranged from 5.70% to 6.49%. As for the minimum mean radiant temperature readings, the readings that were recorded from the field measurements were from 27.21 °C to 27.42 °C, while the readings produced from the IES-VE simulations were 27.81 °C. The percentage difference that was produced for the minimum mean radiant temperature was from -1.42% to 2.21%. The range of percentage differences that was recorded for the mean radiant temperatures was from 1.42% to 6.49% which was below 20%, and thus considered reliable and acceptable as recommended by previous studies and established benchmarks.

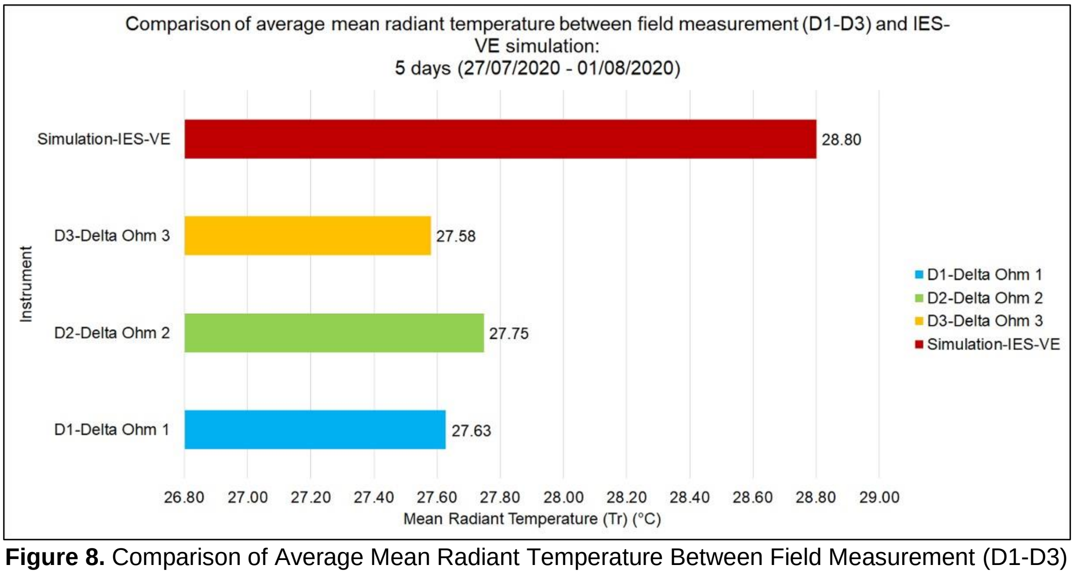

Figure 8. Comparison of Average Mean Radiant Temperature Between Field Measurement (D1-D3) and IES-VE Simulation

Table 4. Comparison of Average Percentage Differences of Mean Radiant Temperature Between Field Measurement and IES-VE Simulation for Five Days

	Instrument Delta Ohm (F0ield Measurement) (°C)			**Simulation IES-VE (°C)**	**Percentage Differences (%)**		
	D1	**D2**	**D3**		**D1**	**D2**	**D3**
Average	27.63	27.75	27.58	28.80	4.23%	3.78%	4.42%
Maximum	27.87	28.08	27.91	29.68	6.49%	5.70%	6.34%
Minimum	27.27	27.42	27.21	27.81	1.98%	1.42%	2.21%

D = Delta Ohm HD32.3 WBGT-PMV

Figure 9 and Table 5 show the comparison of average operative temperature differences between the field measurement and simulation for a five-day duration. The average operative temperature readings that were recorded during the five days of field measurements for instruments D1-D3 ranged from 27.82 °C to 27.91 °C, while the readings produced by the IES-VE simulations over the same period were 28.69 °C. The percentage differences that were recorded for the average operative temperature between the field measurements and simulations ranged from 2.79% to 3.13%. The readings for the maximum operative temperature recorded for the field measurements were from 28.13 °C to 28.24 °C, while the readings produced from the IES-VE simulations were 30.57 °C. The percentage differences that were recorded for the maximum operative temperature between the field measurements and simulations ranged from 8.25% to 8.67%. For the minimum operative temperature readings, the readings that were recorded from the field measurements were from 27.40 °C to 27.56 °C, while the readings produced from the IES-VE simulations were 27.00°C. The percentage difference that was produced for the minimum air temperature was from -2.03% to -1.46%. The range of percentage differences that were recorded for operative temperatures was from -2.03% to 8.67% which was below 20%, and thus considered reliable and acceptable as recommended by previous studies and established benchmarks.

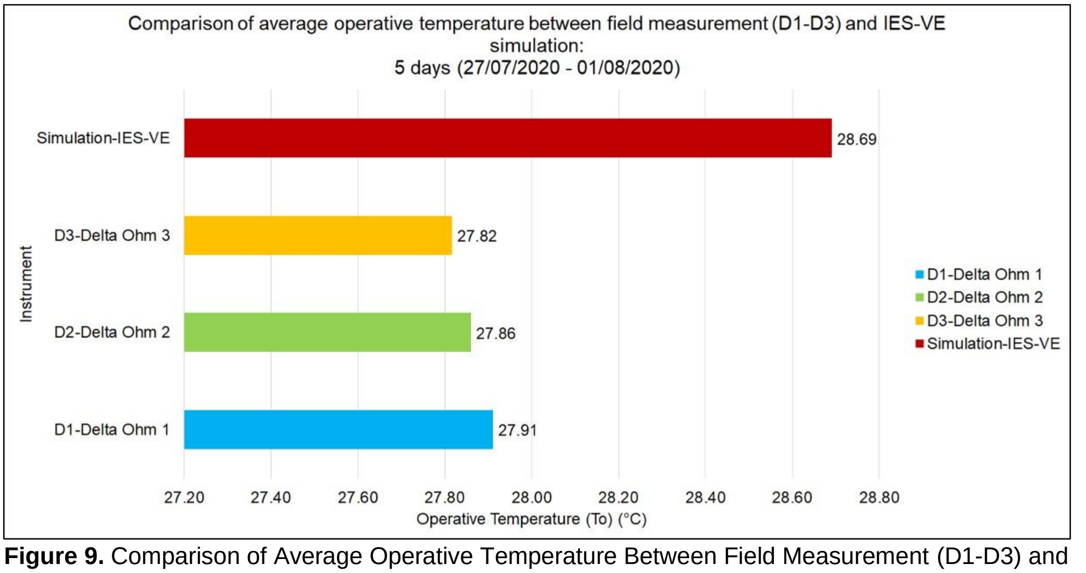

Figure 9. Comparison of Average Operative Temperature Between Field Measurement (D1-D3) and IES-VE Simulation

Table 5. Comparison of Average Percentage Differences of Operative Temperature Between Field Measurement and IES-VE Simulation for Five Days

	Instrument Delta Ohm (F0ield Measurement) (°C)			Simulation IES-VE (°C)	Percentage Differences (%)		
	D1	D2	D3		D1	D2	D3
Average	27.91	27.86	27.82	28.69	2.79%	2.98%	3.13%
Maximum	28.20	28.24	28.13	30.57	8.40%	8.25%	8.67%
Minimum	27.56	27.51	27.40	27.00	-2.03%	-1.85%	-1.46%

D = Delta Ohm HD32.3 WBGT-PMV

Based on the results, the range of percentage differences between the field measurement and IES-VE simulation is from -11.39% to 8.67%. This is within the previous data accuracy, which is below 20%. In other words, the IES-VE is reliable, accurate and is valid to be used as the physical measurement replacement for building performance simulation. Moreover, the result is supported by previous studies, i.e., Leng et al. (2012), Maamari et al. (2006) and Qays Oleiwi et al. (2019).

CONCLUSION

The accuracy investigation that has been carried out on the IES-VE simulation program in accordance with the building performance, namely, for the thermal comfort performance is very important in ensuring that the program can be used in future studies. The accuracy investigation has been conducted on three thermal comfort factors which are air temperature (Ta), relative humidity (RH) and mean radiant temperature (Tr), where a thermal comfort index of operative temperature (To) is one of the alternative steps in the IES-VE program validation process for future research. The results show that:

- The difference of field measurement and IES-VE simulation is small (-11.39% to 8.67%) and is within the acceptable range which is below 20%.
- IES-VE simulation is acceptable and is able to perform effectively for simulating building performance (thermal comfort) of air temperature, relative humidity, mean radiant temperature and operative temperature based on the above statement.

ACKNOWLEDGEMENT

The author would like to acknowledge and thank Universiti Kebangsaan Malaysia (TAP-K015205 and GP-2020-K015205), for its financial support for this research. A sincere appreciation also goes to the Architecture Branch of the Public Works Department (PWD/JKR) Malaysia and the Royal Malaysia Police (RPM).

REFERENCES

Abd. Razak, B., Mohamed, M. F., Yusoff, W. F. M., & Sulaiman, M. K. A. M. (2020). Research on the Design Typology of the Royal Malaysian Police (RMP) Lockups. *International Journal of Advanced Science and Technology*, *29*(9s), 1866–1884.

Ahadi, A. alah, Saghafi, M. R., & Tahbaz, M. (2018). The optimization of light-wells with integrating daylight and stack natural ventilation systems in deep-plan residential buildings: A case study of Tehran. *Journal of Building Engineering*, *18*, 220–244. https://doi.org/10.1016/j.jobe.2018.03.016

Ahmad, Q. T., & Szokolay, S. V. (1994). Validation of thermal design tools. *RERIC International Energy Journal*, 351–357.

Almhafdy, A., Ibrahim, N., Ahmad, S. S., & Yahya, J. (2015). Thermal Performance Analysis of Courtyards in a Hot Humid Climate Using Computational Fluid Dynamics CFD Method. *Procedia - Social and Behavioral Sciences*, *170*, 474–483. https://doi.org/10.1016/j.sbspro.2015.01.012

Anand, P., Deb, C., & Alur, R. (2017). A simplified tool for building layout design based on thermal comfort simulations. *Frontiers of Architectural Research*, *6*(2), 218–230. https://doi.org/10.1016/j.foar.2017.03.001

ASHRAE 55. (2017). *ASHRAE 55-2017 - Thermal Environmental Conditions for Human Occupancy*. www.ashrae.org

Attia, S., Beltrán, L., De Herde, A., & Hensen, J. (2009). "Architect friendly": A comparison of ten different building performance simulation tools. *Eleventh International IBPSA Conference - International Building Performance Simulation Association 2009*, 204–211.

Attia, S., Gratia, E., De Herde, A., & Hensen, J. L. M. (2012). Simulation-based decision support tool for early stages of zero-energy building design. *Energy and Buildings*, *49*, 2–15. https://doi.org/10.1016/j.enbuild.2012.01.028

Cho, C.-S., Chen, D., & Woo, S. (2012). Building Information Modelling (BIM)-Based Design Of Energy Efficient Buildings. *Journal of KIBIM*, *2*(1), 1–6.

Crawley, D. B., Hand, J. W., Kummert, M., & Griffith, B. T. (2008). Contrasting the capabilities of building energy performance simulation programs. *Building and Environment*, *43*, 661–673. https://doi.org/10.1016/j.buildenv.2006.10.027

Ibiyeye, A. I., Mohd, F. Z. J., & Zalina, S. (2015). Natural ventilation provisions in terraced-house designs in hot-humid climates: Case of Putrajaya, Malaysia. *Pertanika Journal of Social Sciences and Humanities*, *23*(4), 885–904. https://www.researchgate.net/publication/283762636

IES-VE. (2020). *Integrated Environmental Solutions-Virtual Environment (IES-VE)*. https://www.iesve.com

Jabatan Meteorologi Malaysia. (2020). *Malaysia Climate*. Jabatan Meteorologi Malaysia. http://www.met.gov.my/pendidikan/iklim/iklimmalaysia

Ji, Y., Lomas, K. J., & Cook, M. J. (2009). Hybrid ventilation for low energy building design in south China. *Building and Environment*, *44*, 2245–2255. https://doi.org/10.1016/j.buildenv.2009.02.015

Lau, A. K. K., Salleh, E., Lim, C. H., & Sulaiman, M. Y. (2016). Potential of shading devices and glazing configurations on cooling energy savings for high-rise office buildings in hot-humid climates: The case of Malaysia. *International Journal of Sustainable Built Environment*, *5*, 387–399. https://doi.org/10.1016/j.ijsbe.2016.04.004

Uniform Building By Law 1986 (Ammendment 2012), Pub. L. No. 133, 1 (2012).

Leng, P. C., Ahmad, M. H. bin, Ossen, D. R., & Hamid, M. (2012). Investigation of Integrated Environmental Solutions-Virtual Environment Software Accuracy for Air Temperature and Relative Humidity of the Test Room Simulations. *UMT 11th International Annual Symposium on Sustainability Science and Management*, 1298–1305.

Maamari, F., Andersen, M., de Boer, J., Carroll, W. L., Dumortier, D., & Greenup, P. (2006). Experimental validation of simulation methods for bi-directional transmission properties at the daylighting performance level. *Energy and Buildings*, *38*(7), 878–889. https://doi.org/10.1016/j.enbuild.2006.03.008

Maarof, S. (2014). *Roof Designs and Affecting Thermal Comfort Factors in a Typical Naturally Ventilated Malaysian Mosque*. Cardiff University.

Mohammadi, A. R., Tahir, M. M., Usman, I. M. S., Abdullah, N. A. G., Che-Ani, A. I., & Utaberta, N. (2010). The effect of balcony to enhance the natural ventilation of terrace houses in the tropical climate of Malaysia. *International Conference on Electric Power Systems, High Voltages, Electric Machines, International Conference on Remote Sensing - Proceedings*, 278–284.

MS 1525:2014. (2014). MS 1525: 2014 Energy efficiency and Use of Renewable Energy for Non-Residential Buildings - Code of Practice. *Department of Standard Malaysia*.

Nguyen, A. T., Reiter, S., & Rigo, P. (2014). A review on simulation-based optimization methods applied to building performance analysis. *Applied Energy*, *113*, 1043–1058. https://doi.org/10.1016/j.apenergy.2013.08.061

Nur 'aini, R. D. (2017). Thermal Performance Simulation of Residential Building in Tropical Climate Case Study: Housing in Bandar Universiti, Malaysia. *International Journal of Built Environment and Scientific Research*, *1*(1), 47–52.

Qays Oleiwi, M., Farid Mohamed, M., Khairul Azhar Mat Sulaiman, M., Irfan Che-Ani, A., & Raman, S. N. (2019). Thermal Environment Accuracy Investigation of Integrated Environmental Solutions-Virtual Environment (IES-VE) Software for Double-Story House Simulation in Malaysia. *Journal of Engineering and Applied Sciences*, *14*(11), 3659–3665. https://doi.org/10.36478/jeasci.2019.3659.3665

SUHAKAM. (2016). *Deaths in Police Custody a Thematic Study on Lock-Up Conditions and Factors Contributing to the Death*. Human Rights Commission of Malaysia. www.suhakam.org.my

World Meteorological Organisation. (2020). *World Weather*. World Meteorological Organisation. https://worldweather.wmo.int/en/home.html

Zaki, W. R. M., Nawawi, A. H., & Sh.Ahmad, S. (2012). Environmental Prospective of Passive Architecture Design Strategies in Terrace Houses. *Procedia - Social and Behavioral Sciences*, *42*, 300–310. https://doi.org/10.1016/j.sbspro.2012.04.194

This page intentionally left blank

GUIDE TO AUTHORS

Aims and Scope:

The Malaysian Construction Research Journal (MCRJ) is the journal dedicated to the documentation of R&D achievements and technological development relevant to the construction industry within Malaysia and elsewhere in the world. It is a collation of research papers and other academic publications produced by researchers, practitioners, industrialists, academicians, and all those involved in the construction industry. The papers cover a wide spectrum encompassing building technology, materials science, information technology, environment, quality, economics and many relevant disciplines that can contribute to the enhancement of knowledge in the construction field. The MCRJ aspire to become the premier communication media amongst knowledge professionals in the construction industry and shall hopefully, breach the knowledge gap currently prevalent between and amongst the knowledge producers and the construction practitioners.

Articles submitted will be reviewed and accepted on the understanding that they have not been published elsewhere. The authors have to fill the **Declaration of the Authors** form and return the form via fax/email to the secretariat. The length of articles should be **between 3,500 and 8,000 words** or **approximately 8 – 15 printed pages (final version)**. **The similarity index must be lower than 20% and the Similarity Report must be submitted together with the manuscript.**

Authors can submit the manuscript:

- By e-mail in Microsoft-Word format to MCRJ Secretariat (mcrj@cream.my; hafizi@cream.my; maria@cream.my)

Malaysian Construction Research Journal (MCRJ)
Construction Research Institute of Malaysia (CREAM)
Level 29, Sunway Putra Tower,
No. 100, Jalan Putra,
50350 Kuala Lumpur,
MALAYSIA.

Tel. : (6)03 – 2779 1479
: (6)03 – 2779 1474
Website : www.cream.my

Language: Follow the spelling of the Oxford English Dictionary.

Size/Page Setup: Executive (18.42 cm x 26.67 cm)

Margin: Top - 3cm, Bottom, Left and Right – 2.01cm

Paper title: Arial, 16.

CODIFICATION AND APPLICATION OF SEMI-LOOF ELEMENTS FOR COMPLEX STRUCTURES

(FULL NAME) Ahmad Abd Rahman[1], Maria Diyana Musa[2] and Sumiana Yusoff[2]
[1]Department of Quantity Surveying, Faculty of Architecture, Planning and Surveying, Universiti Teknologi MARA, Sarawak, Malaysia
[2]Institute of Ocean and Earth Sciences (IOES), University of Malaya, Malaysia

Abstract (Arial Bold, 9pt)
Damage assessment …………..…. (Arial, 9pt. Left and right indent 0.64 cm, it should be single paragraph of about 100 – 250 words)

Keywords: (Arial Bold, 9pt) *Finite Element Analysis; Modal Analysis; Mode Shape; Natural Frequency; Plate Structure (Time New Roman, 9pt)*

HEADING 1 (Arial Bold + Upper Case, 11pt)

Heading 2 (Arial Bold + Lower Case, 11pt)

Heading 3 (Arial Italic + Lower Case, 11pt)

Body Text: Times New Roman, 11 pt. All paragraphs must be differentiated by 0.64 cm tab.

Figures: Figures should be in box with line width 0.5pt. All illustrations and photographs must be numbered consecutively as it appears in the text and accompanied with appropriate captions below them.

Figures caption: Arial Bold + Arial, 9pt. + Capitalize Each Word, should be written below the figures.

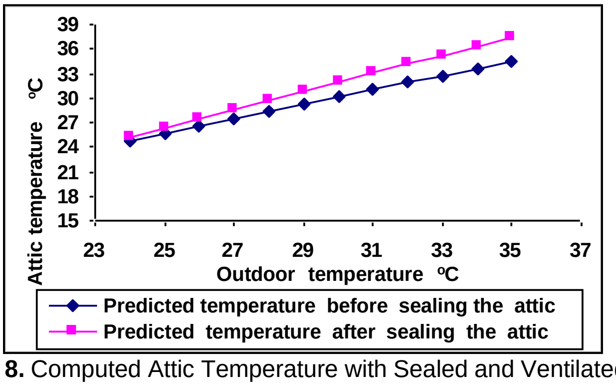

Figure 8. Computed Attic Temperature with Sealed and Ventilated Attic

Tables: Arial, 8pt. Table should be incorporated in the text.

Table caption: Arial Bold + Arial, 9pt. + Capitalize Each Word. Captions should be written above the table.

Table Line: 0.5pt.

Table 1. Recommended/Acceptable Physical Water Quality Criteria

Parameter	Raw Water Quality	Drinking Water Quality
Total coliform (MPN/100ml)	500	0
Turbidity (NTU)	1000	5
Color (Hazen)	300	15
pH	5.5-9.0	6.5-9.0

(Source: Twort et al., 1985; MWA,1994)

Units: All units and abbreviations of dimensions should conform to **SI standards.**

Citation:

Passage Type	First reference in text	Next reference in text	Bracket format, first reference in text	Bracket format, next reference marker in text
One author	Walker (2007)	(Walker, 2007)	(Walker, 2007)	(Walker, 2007)
Two authors	Walker and Allen (2004)	Walker and Allen (2004)	(Walker & Allen, 2004)	(Walker & Allen, 2004)
Three authors	Bradley, Ramirez, and Soo (1999)	Bradley et al. (1999)	(Bradley, Ramirez, & Soo, 1999)	(Bradley et al., 1999)
Four authors	Bradley, Ramirez, Soo, and Walsh (2006)	Bradley et al. (2006)	(Bradley, Ramirez, Soo, & Walsh, 2006)	(Bradley et al., 2006)
Five authors	Walker, Allen, Bradley, Ramirez, and Soo (2008)	Walker et al. (2008)	(Walker, Allen, Bradley, Ramirez, & Soo, 2008)	(Walker et al., 2008)
Six or more authors	Wasserstein et al (2005)	Wasserstein et al. (2005)	(Wasserstein et al., 2005)	(Wasserstein et al., 2005)
Organisation (easily identified by the initials) as the author	Sultan Idris Education University (UPSI, 2013)	UPSI (2013)	(Sultan Idris Education University [UPSI], 2013)	(UPSI, 2013)
Organisation (No abbreviation) as the author	Pittsburgh University (2005)	Pittsburgh University (2005)	(Pittsburgh University, 2005)	(Pittsburgh University, 2005)

(Source: UPSI, 2019)

Reference: Times New Roman, 11pt. Left indent 0.64 cm, first line left indent – 0.64 cm.

References should be listed in **alphabetical order**, on separate sheets from the text. In the list of references, the titles of periodicals should be given in full, while for books should state the title, place of publication, name of publisher, and indication of edition.

Johan, R. (1999) Fire Management Plan for The Peat Swamp Forest Reserve of North Selangor and Pahang. In Chin T.Y. and Havmoller, P. (eds) Sustainable Management of Peat Swamp Forests in Peninsular Malaysia Vol II: Impacts. Kuala Lumpur: Forestry Department Malaysia, 81-147.

Siti Hawa, H., Yong, C. B. and Wan Hamidon W. B. (2004) Butt Joint in Dry Board as Crack Arrester. Proceeding of 22nd Conference of ASEAN Federation of Engineering Organisation (CAFEO 22). Myanmar, 55-64.

Skumatz, L. A. (1993) Variable Rate for Municipal Solid Waste: Implementation, Experience, Economics and Legislation. Los Angeles: Reason Foundation, 157 pp.

Sze, K. Y. (1994) Simple Semi-Loof Element for Analysing Folded-Plate Structures. Journal of Engineering Mechanics, 120(1):120-134.

Wong, A. H. H. (1993) Susceptibility to Soft Rot Decay in Copper-Chrome-Arsenic Treated and Untreated Malaysian Hardwoods. Ph.D. Thesis, University of Oxford. 341 pp.

Publication	References Formatting
Journal	Sze, K. Y. (1994) Simple Semi-Loof Element for Analysing Folded-Plate Structures. Journal of Engineering Mechanics, 120(1):120-134.
Books	Skumatz, L. A. (1993) Variable Rate for Municipal Solid Waste: Implementation, Experience, Economics and Legislation. Los Angeles: Reason Foundation, 157 pp.
Thesis	Wong, A. H. H. (1993) Susceptibility to Soft Rot Decay in Copper-Chrome-Arsenic Treated and Untreated Malaysian Hardwoods. Ph.D. Thesis, University of Oxford. 341 pp.
Chapter in book	Johan, R. (1999) Fire Management Plan for The Peat Swamp Forest Reserve of North Selangor and Pahang. In Chin T.Y. and Havmoller, P. (eds) Sustainable Management of Peat Swamp Forests in Peninsular Malaysia Vol II: Impacts. Kuala Lumpur: Forestry Department Malaysia, 81-147.
Proceedings	Siti Hawa, H., Yong, C. B. and Wan Hamidon W. B. (2004) Butt Joint in Dry Board as Crack Arrester. Proceeding of 22nd Conference of ASEAN Federation of Engineering Organisation (CAFEO 22). Myanmar, 55-64.

MCRJ Volume 40 | No.2 | 2023

Contents

ISSN 1985-3807
9 771985 380005

eISSN 2590-4140
9 772590 414000